ANALYSIS OF WEAKLY IONIZED HYPERSONIC FLOW

A THESIS SUBMITTED TO
THE GRADUATE SCHOOL OF NATURAL AND APPLIED SCIENCES
OF
MIDDLE EAST TECHNICAL UNIVERSITY

BY

TUĞBA PİŞKİN

IN PARTIAL FULFILLMENT OF THE REQUIREMENTS
FOR
THE DEGREE OF MASTER OF SCIENCE
IN
AEROSPACE ENGINEERING

JULY 2015

Approval of the thesis:

ANALYSIS OF WEAKLY IONIZED HYPERSONIC FLOW

submitted by **TUĞBA PİŞKİN** in partial fulfillment of the requirements for the degree of **Master of Science in Aerospace Engineering Department, Middle East Technical University** by,

Prof. Dr. Gülbin Dural Ünver _____
Dean, Graduate School of **Natural and Applied Sciences**

Prof. Dr. Ozan Tekinalp _____
Head of Department, **Aerospace Engineering Dept., METU**

Assoc. Prof. Dr. Sinan Eyi _____
Supervisor, **Aerospace Engineering Dept., METU**

Examining Committee Members:

Prof. Dr. Cevdet Çelenligil _____
Aerospace Engineering Dept., METU

Assoc. Prof. Dr. Sinan Eyi _____
Aerospace Engineering Dept., METU

Assoc. Prof. Dr. Oğuz Uzol _____
Aerospace Engineering Dept., METU

Assoc. Prof. Dr. Serhat Çakır _____
Physics Dept., METU

Asst. Prof. Dr. Sıtkı Uslu _____
Mechanical Engineering Dept., TOBB Uni. of Econ. and Tech.

Date: 06.07.2015

I hereby declare that all information in this document has been obtained and presented in accordance with academic rules and ethical conduct. I also declare that, as required by these rules and conduct, I have fully cited and referenced all material and results that are not original to this work.

Name, Last name: Tuğba Pişkin

Signature:

ABSTRACT

ANALYSIS OF WEAKLY IONIZED HYPERSONIC FLOW

Pişkin, Tuğba

M.S., Department of Aerospace Engineering

Supervisor: Assoc. Prof. Dr. Sinan Eyi

July 2015, 105 pages

The knowledge of physical phenomena and numerical computation skills are required to simulate flow field around the re-entry capsule due to extreme conditions resulted by high speed and high energy of capsule. The re-entries of spacecraft occur generally at high hypersonic speed where reactions take place actively, and where plasma field around geometry as well as radiation from the surface affect characteristics of the flow field. In these conditions, ideal gas assumption fails; thus, real gas assumption is used to define species state characteristics. The main consideration of this study is to compute the components of the flow field by considering thermal, chemical and vibrational nonequilibrium. There are various methods developed to model flow field with the examination of real gas effects and nonequilibrium in each modes. Mainly, these methods differ according to chosen temperature model; the simplest one is one temperature model, where all energy modes are defined with the same temperature. Because the assumptions for one temperature are not sufficient to characterize hypersonic flow field region, the most accepted and the most applied method is two temperature

model by defining translational – rotational and vibrational- electronic temperature. In this model, dissociation reactions and vibrational energy levels of species are associated with Park's approach. Different forward reaction rate constants and two different calculation of equilibrium constant are examined and compared. Moreover, the influences of number of species and reactions are also studied in the modelling chemical nonequilibrium. Three dimensional Apollo Command Module is chosen as geometry. Newton- GMRES method is used to solve flow field, whereas Newton method is used to compute vibrational and translational temperature.

In the numerical modelling part, different CFD considerations are examined such as mesh refinement, order of spatial discretization and different splitting of flux vectors. For the mesh refinement study, flow field is simulated by using three different meshes; coarse, medium and fine. In addition to first order discretization, MUSCL schemes are used to achieve higher order spatial discretization; therefore, different flux limiters are examined to prevent oscillations. Moreover, Van Leer and Steger Warming flux splitting schemes are developed with the consideration of real and ideal gas assumptions. Briefly, the aim of this study is to enhance knowledge about high temperature gas flow and to apply various models with comparisons of each other and that of experimental data.

Keywords: Atmospheric Re-entries, Hypersonic Flow, Real Gas Effects, Chemical Nonequilibrium, Vibrational Nonequilibrium, Two Temperature Model

ÖZ

AZ İYONLAŞMIŞ HİPERSONİK AKIŞLARIN ANALİZİ

Pişkin, Tugba
Yüksek Lisans, Havacılık ve Uzay Mühendisliği Bölümü
Tez Yöneticisi: Doç. Dr Sinan Eyi

Temmuz 2015, 105 sayfa

Yerçekimi ile ivmelenen atmosferik girişler yüksek hız ve enerjilerde gerçekleştiğinden sıcaklık çok büyük değerlere ulaşır. Atmosferik akış gibi yüksek hızlı hipersonik akışların doğru modellenmesi, tüm fiziksel olguların ve çözüm yöntemlerinin uygulanmasıyla mümkündür. Bu gibi yüksek sıcaklıklarda, türlerin akış alanındaki davranışları gerçek gaz varsayımı ile yapılmalıdır. Bu çalışmanın amacı kimyasal, termodinamiksel ve titreşimsel dengesizliklerin gerçek gaz varsayımıyla çözülmesidir. Sıcaklık varsayımlarına göre birçok farklı model bulunmaktadır. En basit olan, tek sıcaklık modeli bütün enerji modlarının tek bir sıcaklık değerleriyle belirlenmesine dayanır. Ancak bu model yüksek sıcaklarda akış alanı çözümünü elde etmede yetersiz kalmaktadır. En çok uygulanan ve kabul edilmiş metot iki sıcaklık modelidir ve bu model döngüsel ile çizgisel enerji modlarını ve titreşimsel ile elektronik enerji modlarını dengede kabul eder. Yüksek sıcaklıklarda, kimyasal reaksiyonlar ve titreşimsel sıcaklık değerleri birbirlerini etkiler. İki olgu arasındaki etkileşim, çizgisel ve titreşimsel sıcaklıkların ortalama değerleriyle bulunur. Bu çalışmada, bu yaklaşımlar incelenmiştir.

Geometri olarak üç boyutlu Apollo Komuta Modülü seçilmiştir, çünkü deney ve uçuş verileri bu geometri etrafında mevcuttur. Hesaplamalar Newton ve Newton Gmres metodları göz önüne alınarak yapılmıştır. Farklı tür sayısı ve farklı varsayımlar bu çalışmada incelenmiş bulunmaktadır.

Bu çalışmanın esas amacı yüksek sıcaklıklarda olan akış hakkındaki bilgiyi genişletip çeşitli modellerin karşılaştırılarak incelenmesidir. Ayrıca fiziksel modellerin karşılaştırılmasının yanı sıra hesaplama yöntemlerinin etkinliği de hesaplanıp karşılaştırılmıştır.

Anahtar Kelimeler: Atmosferik Giriş, Hipersonik Akış, Gerçek Gaz Etkileri, Kimyasal Dengesizlik, Titreşimsel Dengesizlik, İki sıcaklık Modeli

To my family,

ACKNOWLEDGEMENTS

First and foremost acknowledgements go to my supervisor Assoc. Prof. Dr. Sinan Eyi for his support and guidance throughout my studies. Without his support and suggestions, this work would not be possible.

I am indebted to the people of room 31-5; Bade Tonyalı, Hilal Işık and Selen Caner. They make my life more joyful with their existence, support and love. I am so lucky to have such great friends.

I would like to express my thanks to my colleague, Münire Gülay Şenol for her help to complete my thesis. She is always there for me and she has been the greatest source of motivation through my university life.

I would also like to thank TÜBİTAK for providing financial support during this study. Also, I would like to thank all my friends who work on the same TÜBİTAK project (112M129) especially Muharrem Özgün, Hilmi Berk Gür and Oğuz Kaan Onay. I would like to express my gratitude to my roommate and colleague Ali Yıldırım for spending his time to review my results and for helping me when I need throughout this study.

I specially thank to Sebahat and Erdinç Bastepe for their valuable support and encouragement. Also, I am so grateful to Gülsüm and Ali Baş for their helps and efforts to motivate me. I appreciate my friends Deniz Seçilmiş and my roommates (101) for their helps, and never ending support.

I owe my deepest and warmhearted thanks to my family who give me strength and help me throughout the entire period of the study. I am so thankful for my parents, Seher and Durali Pişkin everlasting support, guidance and love. Special thanks go to my siblings Bilge, Kübra and Faruk Pişkin for their unfailing support and their encouragement to keep me walking.

TABLE OF CONTENTS

LIST OF TABLES

TABLES

LIST OF FIGURES

FIGURES

LIST OF SYMBOLS

SYMBOLS

Kn	Knudsen number
λ	Mean free path
Da	Damköhler number
ρ	Density
E	Total energy
E_v	Vibrational Energy
$\dot{w}$	Source terms for species mass and vibrational energy equations
X	Mole fractions of species
Y	Mass fractions of species
α', α''	Stoichiometric coefficients
A_i	Preexponential factor
β_i	Temperature exponent
$k_{f,i}$	Forward reaction rate constant
$k_{b,i}$	Backward reaction rate constant
k_{eq}	Equilibrium constant
T_c	Controlling temperature
T_{tr}	Translational temperature
T_v	Vibrational temperature
θ_v	Characteristic vibrational temperature
$\dot{w}_{v-c}$	Source term for vibrational energy –chemical reactions exchanges
$\dot{w}_{v-t}$	Source term for vibrational energy –translational energy exchanges
$\dot{w}_{v-v}$	Source term for vibrational energy –vibrational energy exchanges
τ_s	Species vibrational relaxation time
F, G, H	Flux vectors
S	Source vectors

Φ	Flux limiter
Δ,∇	Forward and backward operators
ε	Small number to perturb
μ	Forcing term
V	Orthonormal bases
H	Hessenberg matrix

SUBSCRIPTS

s	for each species
i	for each reaction
v	Vibrational energy
j	for each direction

CHAPTER 1

INTRODUCTION

1.1 Motivation

The advancements in the computer technology lead to the development and the extend usage of computational tools for the most of the engineering studies. In the most of aerospace engineering studies, Computational Fluid Dynamics (CFD) is one of the important tools used. The advancement of the spacecraft design strictly depends on the accurate prediction of flow field during the reentry. Because of the experimental difficulties in hypersonic flow, CFD is extensively used to analyze the flow field and to improve design parameters of spacecrafts [1]

Atmospheric re-entries to the Earth's and other planets with considerable gravitational force are characterized by high speed and high enthalpy flow. Because of the high Mach number and high temperature, hypersonic flow fields occurred during re-entries contain dissociation, exchange, charge exchange, dissociative recombination, electron impact ionization and dissociation reactions. Moreover, radiation and the exchange between energy modes which are vibrational, translational, rotational and electric-electronic, occur. Modelling these extreme conditions require sufficient understanding of real gas behaviours and nonequilibrium conditions.

Due to transition of high kinetic energy to thermal energy, the ionization of species takes place frequently; hence, the flow field contains many positive and negative charged species. These charged species cause plasma layer around the body. The number density of charged particles affects frequency of plasma. When the frequency of the plasma layer is higher than the communication band frequency, there will be communication blackout. The accurate prediction of flow field and the

modification of re-entry vehicle have importance on prevention of moral and financial damage and even death. Therefore, accurate modelling of re-entries are important to have successful and safe flights.

1.2 Objective

The understanding of chemical nonequilibrium and vibrational relaxation and then developing a flow solver with consideration of real gas effects are main objectives of this study.

The influence of different thermochemical approaches have been investigated in terms of accuracy, convergence behaviour and computational cost. In addition to ideal gas assumption, code has been extended to investigate real gas effects. To model chemical nonequilibrium, different models and assumptions are examined and compared with available experimental and theoretical data. The coupling chemical reactions and vibrational nonequilibrium with different controlling temperature models are taken into account. After the investigation of high temperature effects with different assumptions, choosing a proper model for future studies with our developed codes is basic consideration of physical modelling.

The computational efforts to simulate physical processes during atmospheric re-entries are studied. Various splitting methods and discretization orders are reviewed. In this study, Newton and Newton GMRES methods is used to simulate hypersonic re-entries with different temperature models. Moreover, Apollo Command Module is chosen as a geometry to evaluate and to verify the developed code.

1.3 Flow Characteristics

During atmospheric re-entries, the change of kinetic energy into internal energy produce enormously high aerodynamic heating; therefore, to simulate effects of this extreme heating during atmospheric re-entries, flow characteristics must be defined. First of all, re-entries are characterized by very high speed and high temperatures. The maximum velocity during the re-entry to Earth's atmosphere was achieved in 2006 by the Stardust Capsule, 12.8 km /s, and the maximum temperature was around 25,000 K [2]. Around this temperature, many reactions start such as dissociation, exchange and ionization.

The flow field during atmospheric re-entries strictly depends on the composition of the atmosphere. Different chemical properties of species in atmosphere yield different flow field characteristics because each species has different mass, energy levels and different chemical bonding structures. In this study, re-entries to the Earth's atmosphere cases are studied. Therefore, initial composition of atmospheric air is considered as 21% of O_2 and 79% of N_2. The species composition is important because of the different reaction characteristics and different energy exchange mechanism between species. The high temperature and nonequilibrium effects make ideal gas assumption invalid; thus, real gas assumption is more suitable. Ideal gas assumption states that gas is in thermally and calorically perfect state. Therefore, following assumptions yield for ideal gases that collisions in between gases occur elastically, there are not any forces between species, and motions of gases are random where distance in-between species are greater than the molecule size [4]. In the hypersonic flow, most of these assumptions are invalid and real gas effects should be considered. Real gas assumptions can affect the shock standoff distance, thermal heating at surface and energy exchange between modes [1]. The physical phenomena, assumptions and available equations through spacecraft motion in atmosphere are summarized in Figure 1.1 which is derived from NASA report [3] and Tirsky's study [7].

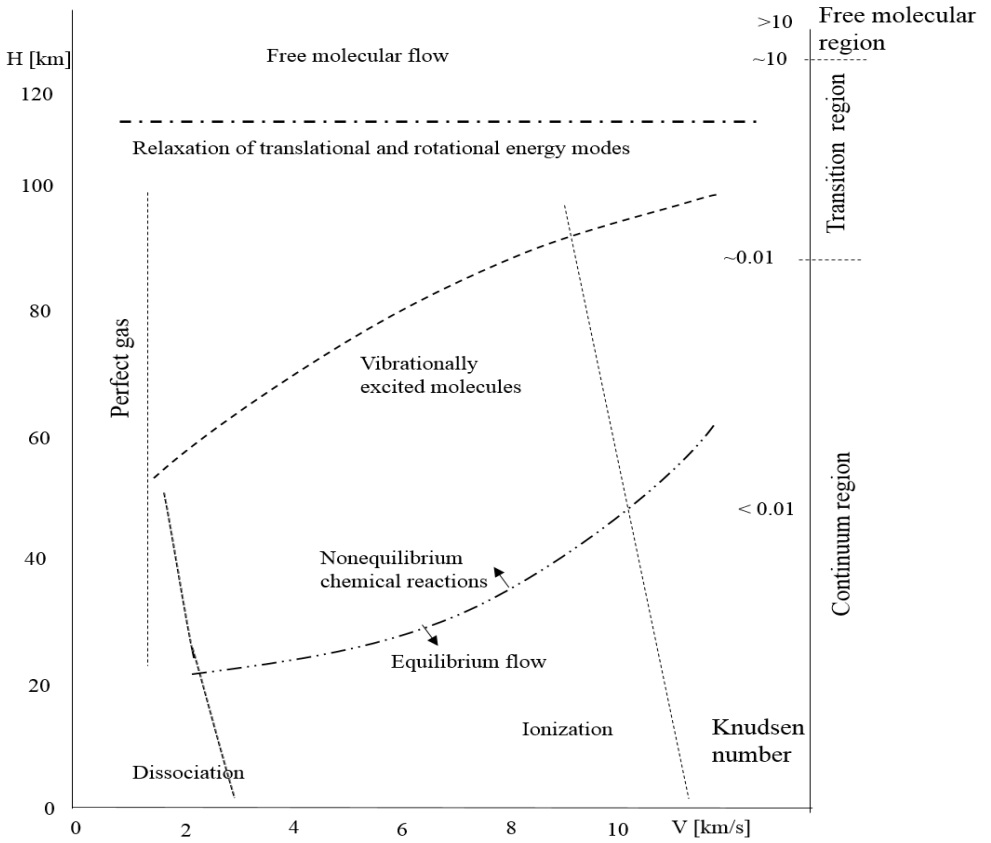

Figure 1.1 Variations of physical phenomena with trajectory of a space shuttle on Earth's atmosphere.

One of the important parameters to observe the flow field characteristics is Knudsen number. Knudsen number is obtained by dividing the mean free path of molecule to the length of spacecraft. The mean free path is the average distance between collisions of two flow components.

The validity of the Navier Stokes equations are restricted with Knudsen number. The applicability of Navier Stokes and Euler equations require enough number of collisions of the flow components; therefore, the exchange between momentum and energy modes are satisfied. Clearly, to solve Navier Stokes and Euler equations, the flow field should be dense enough. In regions where Knudsen number less than 0.01, the flow field can be considered as continuum and the transport equations can be used [5].

The region with Knudsen number in between 0.01 and 10 is named as rarified or translational regime [5]. In these regions, the interactions between particles are low; hence, transport equations are not applicable. However, Boltzmann equations are valid in these regions. Therefore, to obtain solution for these regions, discrete particle models which are based on kinetic theory are used.

For higher values of Knudsen number, Kn > 10, the flow field is defined free-molecular region where number of collisions between particles are poor because of very small number of particles as in Figure 1.1. In these regions, due to lack of the interactions in between components of flow field, shock layer cannot be observed [6]. In these regions, the solution method is based on the statistical mechanics equations: Boltzmann and collisionless Boltzmann equations. In the atmospheric re-entries, Knudsen number varies with the altitude of the re-entry vehicle, and the variation of Knudsen number with the altitude can be observed through Figure 1.1.

Even though global Knudsen number satisfies continuum regime condition, there are locally transition regions. The distinction between local and global Knudsen number must be stated clearly. Instead of considering global Knudsen number, calculation of local Knudsen number will result in more accurate simulations if the flow field has different regions: continuum and transition. Flow solver should be adapted according to these regions. Global and local Knudsen number which are based on the gradient of the flow variable can be written as:

$$Kn = \frac{\lambda}{L} \qquad Kn_{local} = \frac{\lambda}{\psi}\left\|\frac{d\psi}{dx}\right\| \tag{1.1}$$

where ψ is the global flow field variable such as density, pressure and so on, λ is the mean free path and the L is the length of the vehicle.

Determination of whether flow is in thermal and chemical equilibrium or non-equilibrium is done with Damköhler number which is the ratio of the flow residence time to the chemical reaction time. This non-dimensional number can be written as:

$$Da = \frac{\tau_f}{\tau_c} \tag{1.2}$$

where τ_c is the required time for the chemical reactions to reach chemical equilibrium and τ_f is the characteristic flow residence time. When the chemical reaction time scale approaches zero due to very fast reactions, Damköhler number approaches infinity. Therefore, these fast reactions yield equilibrium state. If the chemical reaction time scale is very large compared to the fluid time scale, then the flow field is considered as frozen. That means there is an inadequate change in the flow field composition because of the lack of the chemical reactions. In between equilibrium and frozen state, flow field can be considered as in nonequilibrium.

The high temperature during the re-entry results in ionization reactions; thus, the number of ionized particle increases. The existence of electrons and ions can provide a medium which has plasma dynamic characteristics. The ionization fraction can be obtained through Equation 1.3.

$$x_i = \frac{n_i}{n_n + n_i} \tag{1.3}$$

where n_i, n_n represents number of ionized particles and neutral particles respectively. When x_i approaches to 1, plasma is considered as the fully ionized plasma. For the case of smaller fraction value, plasma is considered as weakly ionized plasma. Most of the studies assume that flow field is weakly ionized because fully ionized flow field is difficult to model and to compute.

1.4 Literature Survey

There are various models which have been developed to simulate hypersonic flow field by considering thermal, chemical and vibrational nonequilibrium. Models vary with respect to their assumptions for the flow field and the physical characteristics of flow field. The most of the studies focused on the continuum assumption in order to use Navier- Stokes and Euler equations. Moreover, there are various studies with real or ideal gas assumptions. Ideal gas assumptions are useful in terms of computational effort and time; however, results with ideal gas assumptions have different characteristics from the real flow field data especially in terms of temperature values [8].

The other important model mainly developed for the transition region is Direct Simulation of Monte Carlo (DSMC). The Monte Carlo methods are numerical techniques based on presenting solutions to physical processes or problems which are obtained from randomness of solution point in a statistical approach. DSMC uses kinetic theory of gases that is also a statistical way to describe distribution functions of flow variable. DSMC was introduced by Bird [9] and many applications with different assumptions were obtained [10]. Unlike the transport equations, DSMC methods are capable of working in both continuum and transition region. However, in continuum regime, DSMC methods require high computational time because of the high number density of species. Therefore, multi scale flow assumptions have been studied by various authors [11] & [12]. Multi scale flow consideration helps to deal with continuum and rarefied flow field regions by reducing computational cost.

The most of the studies differs from each other with temperature usage. For the initial studies, only one temperature is used to define translational and rotational temperatures. To consider vibrational energy, vibrational temperature was introduced by Park [13]. In the two temperature model, exchange between vibrational and electronic energy mode was assumed to be very fast; thus, electronic energy modes of species can be defined with vibrational temperature. Also, there is the assumption to take into account concerning effects of vibrational and

translational temperatures; this assumption is known as Park's two temperature model. Currently, many researchers are using three temperature model for translational- rotational mode, vibrational mode and electronic mode [14] & [15]. The energy exchange mechanism between these three modes must also be considered for the accuracy of physical modelling. In the Boyd study [14], one of the approaches to the correlation of these modes via temperatures is presented. Recently, to simulate rotational energy mode effects, four temperature model has been introduced, [16] although the exchange between translational and rotational energy mode is so fast, and it is expected that the temperature values for translational and rotational modes are close to each other due to fast exchange.

The variety in flow solvers provides opportunity to choose a solver according to the flow field characteristics. There are various flow solvers: explicit, implicit and fully implicit to solve flow field equations. Explicit methods are generally not applicable for the hypersonic flow field computation because governing equations should be solved in coupled equations due to convergence characteristics. Commonly, implicit methods are used to implement governing equations. Splitting and source term of the governing equation can be done in a fully coupled manner to prevent stiffness problem [17].

There are various studies to model chemical nonequilibrium by using finite rate chemistry. The calculations of forward reaction rate in finite rate chemistry is obtained by a curve fitting to experimental data. There are many coefficients sets developed for air reactions by Gupta [18], Dunn Kang [19], Park [20], and Gardiner [21].The reactions are important factors on chemical composition and characteristics of flow. Moreover, to calculate backward reaction rate, two models are commonly used in modelling of hypersonic re-entries. The first one is Gibb's free energy minimization and the second one is Park's polynomials with curve fitted coefficients [20]. It is mentioned in following chapter that vibrationally excited molecules are most likely to dissociate. There are many approaches to couple vibrational temperature and chemical reactions, the most well-known and the simplest method of which is using Park's average temperature on dissociation reactions. The modification on Park's temperature is suggested by Sharma [22].

The dissociation probabilities are introduced to couple two modes by Treanor [23]. Knab extended Treanor study with the assumption stating that chemical reactions would not affect vibrational mode of molecules [24]. Lastly, Macheret's model based on dissociation reactions of upper levels is related with vibrational temperature whereas translational temperature is used for low energy levels [25].

1.5 Scope of Thesis

The physical modelling of flow field are given in Chapter 2 in addition to assumptions done for modelling chemical and vibrational nonequilibrium, and governing equations are given in general form. In the thermodynamic nonequilibrium part, ideal and real gas assumptions and the characteristics of flow field with an increasing temperature are explained. In the chemical nonequilibrium part, reactions for different species number are listed. Finite rate chemistry and coupling between reactions and vibrational temperature are given in detail. Moreover, different curve fit coefficients and models to simulate chemical nonequilibrium are mentioned. Lastly, vibrational energy and source terms are explained. The computation steps of vibrational and translational temperature are also clarified in this chapter.

Chapter 3 introduces the numerical method to solve equations which are defined in the previous chapter. Transformations of the Euler equations from physical spaces to computational space are given where transformations are shown in flow variables and flux vectors. First order and higher order spatial discretizations are given. The limiters which are used to provide oscillations in the higher order reconstruction are also stated. Van Leer and Steger Warming flux splitting schemes are modified for real gas assumptions. As a solver, Newton GMRES method, inexact, is explained with the comparison of an exact solver. Lastly, boundary conditions of flow domain are given.

In Chapter 5, obtained results are given and discussed. The geometry, Apollo Command Module sketch and results of the verification of the code are presented. Also, mesh refinement was examined in terms of CPU time and residual history. Ideal gas and real gas assumptions are compared, and the influence of species number and number of reactions are also studied. One temperature and two temperature models effects are also clarified. There are various models discussed in Chemical Nonequilibrium part of Chapter 2 where the comparisons of these models are also stated. Also, different splitting methods and different orders of discretization with different flow conditions are investigated.

At the end, conclusions and comments about this study are drawn and recommendations for future works are summarized in Chapter 6.

CHAPTER 2

PHYSICAL MODELLING

The simulation of the hypersonic flow field requires well defined characteristics of flow by considering all phenomena changing properties of the flow regime. The extreme kinetic energy results in nonequilibrium between each energy mode, ionization and excitation reactions. Nonequilibrium yields source term to governing equations. Before writing governing equations, basic assumptions for this study to compute weakly ionized hypersonic flow field can be listed as follows;

i. The medium is considered as continuum region, and the modelled re-entry altitude is approximately 40 km. Therefore, Navier Stokes and Euler equations can be used. The calculation at rarefied and free molecular regions are neglected.

ii. Viscous effects are neglected, and Euler equations are used to define governing equations. Also, flow is accepted as steady flow where there is no time dependence.

iii. Heat transfer is neglected.

iv. The flow is defined as nonequilibrium flow where energy changes between modes of species occur actively; hence, Damköhler number is in the range of nonequilibrium flow.

v. The number density of ionized particle is assumed as lower than the required number density to define flow field as plasma. Therefore, the region is weakly ionized and plasma dynamic effects are neglected.

The other assumptions for the modelling of nonequilibrium of modes are given in each nonequilibrium section. According to these basic assumptions, governing

equations for reacting gas flow which is in nonequilibrium can be modelled as follows by using two temperature assumptions. In the following formulation, equations are given in unsteady form to show flow variable vector clearly;

Species mass conservation:

$$\frac{\partial}{\partial t}\rho_s + \frac{\partial}{\partial x^j}\rho_s u^j = \dot{w}_s \qquad (2.1)$$

Total mass conservation:

$$\frac{\partial}{\partial t}\rho + \frac{\partial}{\partial x^j}\rho u^j = 0 \qquad (2.2)$$

Conservation of momentum in each direction:

$$\frac{\partial}{\partial t}\rho u^k + \frac{\partial}{\partial x^j}(\rho u^k u^j + P^j) = 0 \qquad k=1,2,3 \qquad (2.3)$$

Conservation of total energy:

$$\frac{\partial}{\partial t}\rho E + \frac{\partial}{\partial x^j}(\rho E + P)u^j = 0 \qquad (2.4)$$

Conservation of vibrational energy:

$$\frac{\partial}{\partial t}\rho E_v + \frac{\partial}{\partial x^j}\rho E_v u^j = \dot{w}_v \qquad (2.5)$$

In these governing equations, source term vector has non zero values for conservation of species mass and that of vibrational energy equation. The methods to solve these coupled equations are mentioned in the following chapter. The source term of species mass conservation is the production rate of species due to reactions and rates for each species are obtained from finite rate chemistry. The other source term includes interactions of translational- vibrational energy exchanges, chemical reactions- vibrational energy interactions and energy transfer between electrons and heavy particles which are ions and neutrals. For the one temperature model, species mass, total mass, momentum and total energy conservation equations are solved;

thus, vibrational energy conservation is not considered. All energy modes which are translational, rotational, vibrational and electronic are modelled with single temperature. In the two temperature models, five equations (2.1, 2, 3, 4 and 5) are solved, and total energy includes vibrational energy mode. Also, second temperature is used to obtain vibrational source term and vibrational energy of species. Moreover, ideal and real gas assumptions are explained in following section in detail.

2.1 Mixture Properties

The atmospheres are generally a mixture of different atoms, molecules, ions and electrons. The modelling of the re-entries requires the consideration of mixture properties such as partial pressure, mole and mass fractions and concentrations. The primitive flow variables are generally obtained by using mixture properties. The mass fractions of species, Y_s, are obtained as the mass of species, i, per the unit total mass and the summation of mass fractions of each species equals to one, as in Equation 2.6

$$Y_s = \frac{\rho_s}{\rho} \quad \text{and} \quad \sum_{s=1}^{N_s} Y_s = 1 \tag{2.6}$$

The molar mass of the mixture, M from Dalton's law can be written as:

$$\frac{1}{M} = \sum_{s=1}^{N_s} \frac{Y_s}{M_s} \tag{2.7}$$

where M_i is the species molar mass. The mole fractions, X_i are important to simulate chemical nonequilibrium.

$$X_i = \frac{N_i}{N} = \frac{N_i}{\sum_{i=1}^{N_s} N_i} \tag{2.8}$$

Also, the summation of the mole fraction of each species are equal to unity. The physical characteristics of flow field can be obtained after considering of the mixture properties. Pressure, gas constants, specific heat constants and the like are obtained from each component of the mixture.

2.2 Thermodynamic Nonequilibrium

The thermophysical modelling of the flow field is based on two different assumptions: ideal and real gas. For the low temperature (<1000 K), ideal gas assumptions work properly; however, ideal gas assumption starts failing with increasing temperature. High temperature and density require real gas consideration to obtain more correct simulation of the flow field in the hypersonic re-entries.

2.2.1 Ideal Gas Assumption

In terms of the simplicity and the range of applicability of ideal gas assumption, many studies have used equations derived with this assumption. However, hypersonic flows are mostly not in the range of applicability of real gas assumptions. The definition of ideal gas in terms of statistical kinetic theory is based on assumptions: the attractive and repulsive interaction of species are ignored, elastic collisions occur between gas species which are elastic, size of the species with respect to average distance between species are close to each other, and motion of species are freely random [4]. In terms of degree of freedom, each species has three degree of freedom. From the view pointed by classical approach, equipartition theory specifies that each degree of freedom has the same energy in thermal equilibrium [20]. Species distribution functions are obtained by using Maxwell Boltzmann distribution function. All equations derived and used in this section are obtained by using the above assumptions and physical phenomena.

Generally, ideal gases are known as gases which are also calorically and thermally perfect. The equation of state can be written as follows;

$$P = \sum_{s=1}^{N_s} \rho_s R_s T \tag{2.9}$$

If the behavior of gases can be modeled by using thermal equation of state, these gases are considered as thermally perfect. Furthermore, if gases have constant specific heat, they are accepted as calorically perfect. For the thermally perfect gas, enthalpy and internal energy for species can be written as function of temperature.

$$C_v = \left(\frac{\partial e}{\partial T}\right)_v \text{ and } C_p = \left(\frac{\partial h}{\partial T}\right)_p \tag{2.10}$$

The implementation of Equation 2.10 by considering reference value as formation enthalpy of species can be written as Equation 2.11, where the formation enthalpy values are obtained at absolute temperature.

$$e = \int_0^T C_v dT + h_f^o \quad \text{and} \quad \mathrm{h} = \int_0^T C_p dT + h_f^o \tag{2.11}$$

With ideal gas assumption, specific heat ratio of air is assumed as $\gamma = C_p/C_v \cong 1.4$ then total energy can be obtained from following equation. The value of specific heat ratio is constant for ideal gas.

$$\mathrm{E} = \frac{P}{\gamma - 1} + \frac{1}{2}\rho(u^2 + v^2 + w^2) \tag{2.12}$$

The ideal gas assumption was examined both with reaction and without reaction. In the simulation of flow field with reactions, total terms (enthalpy, specific heat constants and entropy) are obtained by summing over each species; moreover, in order to close the system of coupled equations, Dalton's Law, Equation 2.9 is used. Also, temperature calculation is directly obtained from the equation of state.

One of the excepted behaviors of flow calculation is having good approximation with ideal gas at low Mach values[26]. The importance of real gas assumption arises with high temperature and high Mach values. The effects of ideal gas assumptions for various conditions are shown in the Results section.

2.2.2 Real Gas Assumption

The real gas can be defined as thermally imperfect gas which require consideration of the intermolecular forces in the thermal description of the gas flow. There are various studies to see the effects of real gas and ideal gas assumptions on flow field simulation. In blunt bodies, shock standoff distance is reduced due to real gas effects; also, there are differences in surface heating rates, shock characteristics and flow compositions [27]. Therefore, the consideration of real gas effects provides reduced risk factor on simulation and design of re-entries.

There are different energy modes for atoms and molecules. For atoms, there are electronic energy modes and translational energy modes. On the other hand, nuclear motion of the molecules are modelled with translational, rotational and vibrational energy modes. Also, energies of electrons in the molecules are modelled with electronic energy. As a result of Schrödinger equations, there are only allowed quantized energy levels. The required energy to excite energy levels are given in decreasing order as electronic, vibrational, rotational and translational. The correlation between these energy modes can be seen in Figure 2.1.

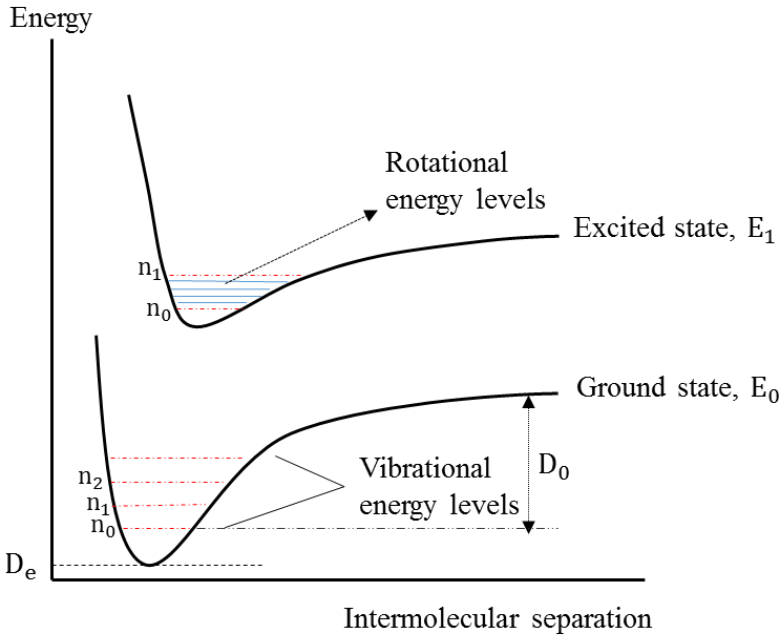

Figure 2.1. Different energy modes for diatomic species

As it can be seen in the graph, D_e is the ground state of the electronic energy, and the dissociation energy is represented with D_0 in the above figure. It can be noticed that if vibration occurs at higher levels, dissociation of diatomic species are more likely to happen. The simulation which considers all energy modes with different temperatures gives more accurate results however computational efforts increases with the number of temperatures. Moreover, because of the fast exchange between energy modes, there exist equilibrium between energy modes [28].

In this study, real gas effects are examined with one temperature and two temperature models. In the following sections, two different temperature models are explained and formulations are given in detail.

2.2.2.1 One Temperature Model

The one temperature model is based on the assumption that all energy modes are in equilibrium. One temperature model provides simplicity to solve governing

equations; however, it overestimates the equilibrium rates [20]. The total energy with one temperature can be written as:

$$\mathrm{E} = \sum_{s=1}^{N_s} \rho_s C_{v,s} T + \frac{1}{2}\rho(u^2 + v^2 + w^2) + \sum_{s=1}^{N_s} \rho_s h_s^0 \tag{2.13}$$

The calculation of specific heat constants are obtained from curve fit equations which are fourth order polynomials.

$$\frac{\mathrm{C_{p,s}}}{\mathrm{R}} = \mathrm{a_{1,s}}\frac{1}{\mathrm{T^2}} + \mathrm{a_{2,s}}\frac{1}{\mathrm{T}} + \mathrm{a_{3,s}} + \mathrm{a_{4,s}T} + \mathrm{a_{5,s}T^2} + \mathrm{a_{6,s}T^3} + \mathrm{a_{7,s}T^4} \tag{2.14}$$

As in the Equation 2.14, specific heat at constant pressure is function of temperature and specific heat constant is evaluated at each cell in each iteration. Also, species enthalpies are obtained from curve fit, Equation 2.15.

$$\frac{\mathrm{h_s}}{\mathrm{R}} = -\mathrm{a_{1,s}}\frac{1}{\mathrm{T}} - \mathrm{a_{2,s}}\ln(\mathrm{T}) + \mathrm{a_{3,s}T} + \mathrm{a_{4,s}}\frac{\mathrm{T^2}}{2} + \mathrm{a_{5,s}}\frac{\mathrm{T^3}}{3} + \mathrm{a_{6,s}}\frac{\mathrm{T^4}}{4} + \mathrm{a_{7,s}}\frac{\mathrm{T^5}}{5} + \mathrm{a_{8,s}} \tag{2.15}$$

Species entropies are obtained from the same curve fit coefficients as:

$$\frac{S_s}{R} = -a_{1,s}\frac{1}{2T^2} - a_{2,s}\frac{1}{T} + a_{3,s}\ln(T) + a_{4,s}T + a_{5,s}\frac{T^2}{2} + a_{6,s}\frac{T^3}{3} + a_{7,s}\frac{T^4}{4} + a_{9,s} \tag{2.16}$$

These nine coefficients are obtained from the report of NASA Glenn Research Center, NASA Glenn Coefficients for Calculating Thermodynamic Properties of Individual Species [29]. Coefficients are given for each species at three temperature range. The temperature values are in the range of 200 K and 20000K. Coefficients are given in Appendix A. For higher temperature values, there are curve fits values up to 30000K for air [18].

The temperature values from flow variables are obtained by using Newton's method. The Newton method to obtain solutions of a system of equations is obtained as:

$$T^{n+1} = T^n - \frac{f(T^n)}{f'(T^n)} \tag{2.17}$$

The previous formulation requires initial guess and functions depends on flow variables. The function to calculate temperature can be written as :

$$f(T) = \rho E - \left[\rho h - P + \frac{1}{2}(u^2 + v^2 + w^2)\right] \cong 0 \tag{2.18}$$

The first term comes from CFD calculations and the second one is obtained from flow properties at each cell by using curve fitted equations. Basically, the aim of Newton's method is to reduce the second term in Equation 2.17. With one temperature model, thermochemical nonequilibrium is modelled; however, vibrational nonequilibrium equations are not solved.

2.2.2.2 Two Temperature Model

In two temperature model, one temperature is used for translational and rotational energy modes and one temperature is used for vibrational and electronic energy modes. As in the one temperature model, vibrational temperature can be equilibrated with translational temperature; however, equilibration processes take time [4]. Also, it is assumed that each diatomic species is equilibrated with the same vibrational temperature because it is shown that there are small differences between vibrational temperature of oxygen and nitrogen gases in atmospheric re-entries to the Earth's atmosphere [30].

The relation between vibrational temperature and chemical reactions plays important role on the correct simulation of flow field. Especially, there may be some overestimated reaction rates behind the shock with one temperature model [7]. The coupling between vibrational temperature and chemical reactions are given in the following section.

The total energy including vibrational mode can be written as in Equation 2.19. The calculation of total vibrational energy is given in the Vibrational Nonequilibrium section.

$$\mathrm{E} = \sum_{s=1}^{N_s} \rho_s C_{v,s} T_{tr} + E_v(T_v) + \frac{1}{2}\rho(u^2 + v^2 + w^2) + \sum_{s=1}^{N_s} \rho_s h_s^0 \qquad (2.19)$$

The addition of vibrational energy to the system of equations increases the length of flow variable and flux vector. Governing equations are still coupled with each other. Also, enthalpy and entropy calculations are obtained from Equation 2.14-16.

2.3 Chemical Nonequilibrium

In this study, re-entries to Earth's atmosphere are studied with various species numbers. The main components of the Earth's atmosphere are oxygen (21%) and nitrogen (%79). Oxygen dissociations start at approximately around 2000 K and complete around 4000 K; also, nitrogen dissociation reactions occur nearly in between 4000 K and 9000 K [16]. Basically, dissociation and exchange reactions are modelled with five species: O_2,N_2, NO, N and O.

Table 2.1. Reactions for 5 species

Dissociation reactions (M : O_2,N_2, NO, N and O)	$O_2 + M \rightleftarrows 2O + M$ $N_2 + M \rightleftarrows 2N + M$ $NO + M \rightleftarrows N + O + M$
Exchange (Zel' dovich) reactions	$N_2 + O \rightleftarrows NO + N$ $NO + O \rightleftarrows O_2 + N$

The number of reactions for 5 species chemistry model is 17 including dissociation and exchange reactions. Ionization reactions start to generate electron with an increasing temperature. Therefore, at very high temperature, ions and electrons should be considered in addition to neutral species, and reactions are charge exchange, dissociative recombination, electron impact ionization and electron impact ionization in addition to dissociation and Zel' dovich reactions. For the second case, there are 11 species which are O_2,N_2, NO, N, O, O_2^+, N_2^+, NO^+, N^+, $O^+$and e. The modelled reaction number is 49 for the 11 species which are listed in Table II. In Table II, dissociation and exchange reactions are not listed and there are 30 different dissociation reactions obtained through different combinations with M; O_2,N_2, NO, N, O, O_2^+, N_2^+, NO^+, N^+, $O^+$and e.

Table 2.2. Reactions for 11 species

Dissociative recombination reactions:	$N + O \rightleftarrows NO^+ + e$ $O + O \rightleftarrows O_2^+ + e$ $N + N \rightleftarrows N_2^+ + e$
Charge exchange reactions:	$NO^+ + O_2 \rightleftarrows {O_2}^+ + NO$ $NO^+ + N \rightleftarrows {N_2}^+ + O$ $NO^+ + O \rightleftarrows {O_2}^+ + N$ $NO^+ + O \rightleftarrows O_2 + N_2^+$ $NO^+ + N \rightleftarrows N_2 + O^+$ $O^+ + N_2 \rightleftarrows {N_2}^+ + O$ $O^+ + NO \rightleftarrows N^+ + O_2$ ${O_2}^+ + N_2 \rightleftarrows {N_2}^+ + O_2$ ${O_2}^+ + N \rightleftarrows N^+ + O_2$
Electron impact dissociation:	$N_2 + e \rightleftarrows 2N + e$
Electron impact ionization:	$N + e \rightleftarrows N^+ + 2e$ $O + e \rightleftarrows O^+ + 2e$

The general formulation for each reaction is as follows:

$$\sum_{l=1}^{n_s} \alpha'_{l,i} X_l \underset{k_{b,i}}{\overset{k_{f,i}}{\rightleftarrows}} \sum_{l=1}^{n_s} \alpha''_{l,i} X_l \qquad i = 1,2, \ldots n_r \qquad (2.20)$$

where n_r is the number of reactions, X is the species chemical symbol and α', α'' are the stoichiometric coefficients.

Initially, it is assumed that flow is in chemical nonequilibrium. The comparison between time scale of flow and that of reaction allows to choose appropriate models to solve chemical compound. Generally, atmospheric re-entries are characterized by chemical nonequilibrium to provide adequate description to thermochemical characteristic of flow. For the nonequilibrium flow, finite rate chemistry model is used to obtain rate of forward and backward reaction rates. The nonequilibrium chemistry differs from equilibrium and frozen chemistry in the rates of chemical reactions. There are no rate processes calculation in the frozen flow and forward and backward reaction rates are equal in equilibrium flow. The tendency of reversible and irreversible reactions is required for modelling chemical nonequilibrium. The forward reaction rate constants are obtained from the Arrhenius Law, Equation 2.21.

$$k_{f,i}(T_r) = A_i {T_f}^{\beta_i} e^{-\frac{E_i}{R_u T_r}} \tag{2.21}$$

where A_i is the preexponential factor, β is the temperature exponent and E is the activation energy for each reaction. Also, the definition of temperature in the forward reaction rate equation is one of the important factors to couple vibrational and chemical modes. The various definitions on this controlling temperature will be mentioned throughout this chapter.

The coefficients of Arrhenius rate equation for each reaction are given in Appendix A. It should be noted that nonequilibrium flow simulation is very responsive to forward and backward reaction rate. There are various coefficients developed by Gardiner, Dunn & Kang, Gupta, curve fit, Park 85, 87, 90 and 93 models. The response of the flow solver to different reaction rate constants is examined in this study.

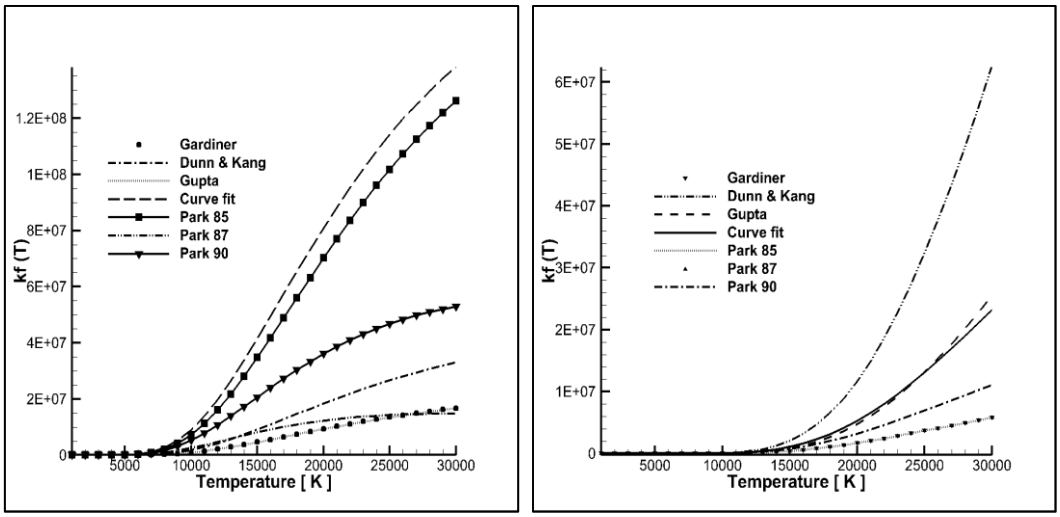

Figure 2.2. Forward reaction rates for two different dissociation reactions (left: $O_2 + N_2 \rightleftarrows 2O + N_2$ and right: $2N_2 \rightleftarrows 2N + N_2$) with different reaction rate models

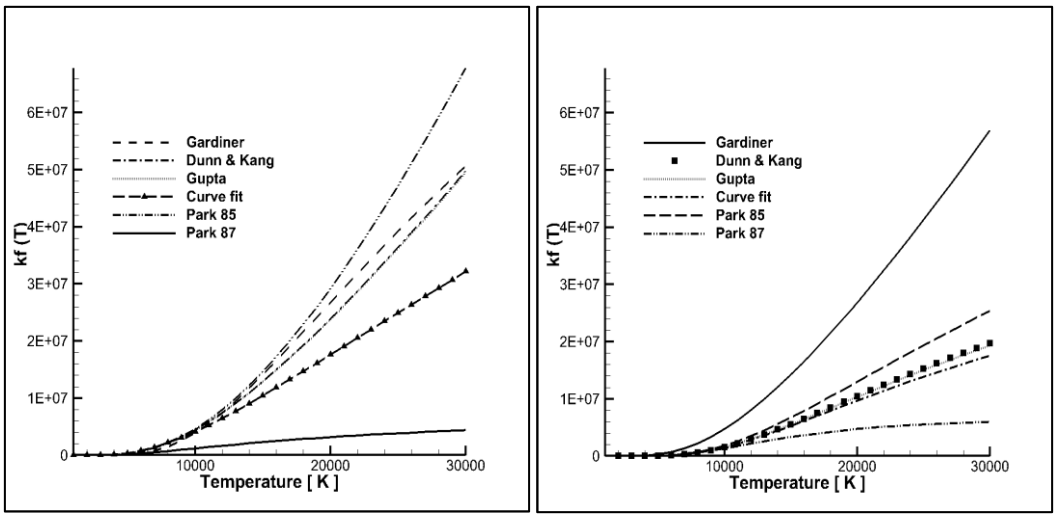

Figure 2.3. Forward reaction rates for exchange reactions (left: $N_2 + O \rightleftarrows NO + N$ and right: $NO + O \rightleftarrows O_2 + N$) with different reaction rate models

The various forward reaction rates with different reaction rate models for dissociation reactions: $O_2 + N_2 \rightleftarrows 2O + N_2$ and $2N_2 \rightleftarrows 2N + N_2$ are represented in Figure 2.2. In Figure 2.3, effects of forward reaction rate constants for Zel' Dovich reactions on rate can be seen. There are various overlapped models which have same rate constants. With an increasing temperature, differences between

reaction rate models become significant. The determination of reaction rates is an important source of uncertainties of the flow fields analysis and also important factor on the stiffness of the flow solver [26]. The effects of reaction rate constants are examined in the Results and Discussion chapter.

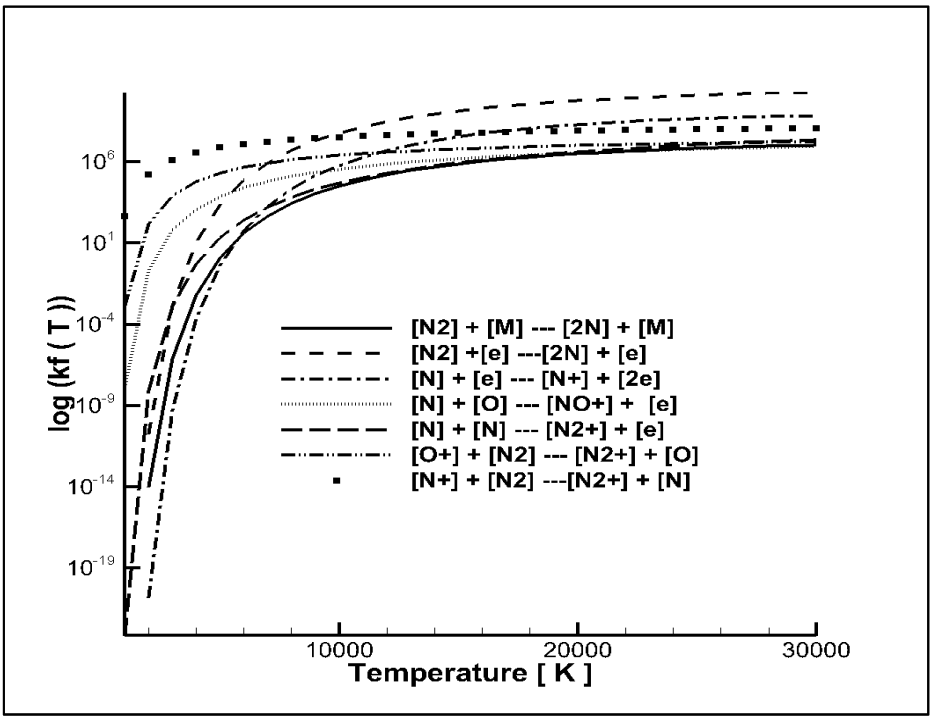

Figure 2.4. Forward reaction rates for different reactions with Park's coefficients

In the Figure 2.4, the responses of different reactions to temperature are examined and logarithmic scale is used because of enormous differences in reaction rates. It can be seen that electron impact ionization and charge exchange reactions require higher temperatures than electron impact dissociation and dissociative recombination reactions. It can be observed that ions and electrons are important factors on the chemical nonequilibrium at high temperature values.

The backward reaction rate should also be computed for the sake of finite rate chemistry. To calculate backward reaction rate constant, equilibrium constants for each reactions should be calculated as in Equation 2.22.

$$k_{b,i} = \frac{k_{f,i}}{k_{eq,i}} \tag{2.22}$$

There are two ways to compute equilibrium constant: Gibb's free energy minimization and curve fits methods. Equilibrium constant calculation by using Gibb's free energy and pressure correction is:

$$k_{eq,i} = k_p(T_b)\left(\frac{R_u T_b}{P_{atm}}\right)^{\alpha} \tag{2.23}$$

where $\alpha = \sum_{l}^{n_s}(\alpha_l' - \alpha_l'')$ is the difference of stoichiometric coefficients. The equilibrium constant at one atmospheric pressure is k_p which is evaluated as:

$$k_p(T_b) = e^{-\Delta g/RT_b}$$

$$\Delta g = \sum_{l}^{n_s}(\alpha_l'' - \alpha_l')g = \sum_{l}^{n_s}(\alpha_l'' - \alpha_l')(h_i - S_i T_b) \tag{2.24}$$

The normalized enthalpy and entropy values used in Equation 2.24 are obtained from Equation 2.15.

The other method used in this study to obtain equilibrium constant is the curve fit introduced by Park [13]. Park's fourth order exponential function can be written as:

$$k_{eq,i} = e^{(c_1 z^{-1} + c_2 + c_3 \ln z + c_4 z + c_5 z^2)} \tag{2.25}$$

where $z = 10000/T$ and coefficients for each reactions are obtained for maximum temperature of 10000K. For the higher temperature Gupta [18] developed curve fit values up to 30000 K to have more suitable results, Equation 2.26.

$$k_{eq,i} = e^{(c_1 z^5 + c_2 z^4 + c_3 z^3 + c_4 z^2 + c_5 z^1 + c_6)} \tag{2.26}$$

The coefficients used in this study to obtain equilibrium constants are given in Table A.VIII. After calculation of forward and backward reaction rates, source term calculations can be done. The change in any arbitrary species concentration because of chemical reactions is obtained by using the law of mass action:

$$\dot{w}_s = M_s \sum_{i=1}^{n_r} (\alpha''_{si} - \alpha'_{si}) \left[k_{f,i} \prod_{s=1}^{n_s} [X_k]^{\alpha'_{si}} - k_{b,i} \prod_{s=1}^{n_s} [X_k]^{\alpha''_{si}} \right] \quad (2.27)$$

where [X] is the molar concentration of species, n_r is the number of reactions and n_s is the number of species. The nondimensional form of chemical source terms are used in this study.

In this study, one and two temperature models are used. For one temperature flow, T_f, temperature value to obtain forward reaction rate in Equation 2.21, and T_b, temperature value to obtain backward reaction rate in Equation 2.23 are chosen as a translational temperature. However, modelling dissociation reactions only with a translational temperature will overestimate the total dissociation because of the time difference between translational and vibrational modes to reach maximum values [35]. Therefore, there are many studies to couple vibrational relaxation and dissociation reactions to consider the effects of the vibrational modes on dissociation reactions. First of all, Park introduced the controlling temperature which is the geometrical average of vibrational and translational temperatures [20]. The controlling temperature can be written in general form as Equation 2.28.

$$T_c = T_{tr}^p T_v^q \quad (2.28)$$

where the summation of p and q is 1. For the Park's controlling temperature, p and q equals to 0.5. Also, controlling temperature is used only in the computation of the forward reaction rates of species. Backward reaction rate computation is done by using translational temperature because vibrational relaxation is an important parameter for diatomic species. However, for dissociative recombination,

vibrational temperature is used for calculating backward reaction rate of electron impact ionization and electron impact dissociation reactions which generate electrons as a products [31].

The other coupling method implemented in this study was introduced by Sharma at al. [22]. This method was derived from SSH (Schwartz, Slawsky, and Herzfeld) theory and it states that higher order vibrational states have fast exchange with dissociation reactions. The dependence of controlling temperature to vibrational temperature is reduced in this method, where p is 0.7 and q is 0.3. The sensitivity of the chosen coupling, Z, can be measured with Equation 2.29.

$$Z(T, T_v) = \frac{k_f(T, T_v)}{k_f(T)} \tag{2.29}$$

The comparisons between coupling methods can be obtained by using Equation 2.29. Although, the Park's controlling temperature is based on experimental data from a shock tube, there is no certain ways to verify coupling methods on a physical basis [8]. Also, coupling methods are other important source of uncertainties. The various coupling factors are examined in this study with different p and q values.

2.4 Vibrational Nonequilibrium

The total change in vibrational states of diatomic molecules are obtained by summing over all diatomic species vibrational energy, Equation 2.30.

$$E_v = \sum_s E_{v,s}\rho_s \tag{2.30}$$

Species vibrational energy is obtained by using Equation 2.31. It is based on the assumption which each diatomic species is equilibrated with one common vibrational temperature.

$$E_{v,s} = \frac{R_s \theta_{v,s}}{\left(e^{\frac{\theta_{v,s}}{T_v}} - 1\right)} \tag{2.31}$$

where θ is the characteristic vibrational temperature and $\theta_{v,s} = {h\nu}/{k}$. h is the Planck constant, k is the Boltzmann constant. The characteristic vibrational temperature of species are given in Table A.1. The characteristic vibrational temperature of atoms are zero because the existence of vibrational states requires relative motion of atoms with respect to each other by chemical bonds. The energy equation is obtained by integrating specific heat constant at constant volume for vibrational states, $C_{v,v,s}$, Equation 2.32, up to temperature T.

$$C_{v,v,s} = \begin{cases} \dfrac{R_s \left(\dfrac{\theta_{v,s}}{T_v}\right)^2 e^{\frac{\theta_{v,s}}{T_v}}}{\left(e^{\frac{\theta_{v,s}}{T_v}} - 1\right)^2} & \text{for molecules} \\ 0 & \text{for atoms and electrons} \end{cases} \tag{2.32}$$

When the ratio of the characteristic vibrational temperature to vibrational temperature approaches zero, C_v values approach R, thus; equipartition theory holds and vibrational energy states are fully excited [22]. Although, electronic energy states require more energy than vibrational energy state to excite, vibrational and electronic energy modes are assumed as equilibrated with one temperature, T_v.

The vibrational source term basically includes three terms which are the exchange of vibrational –translational modes, exchange of vibrational modes –chemical reactions and exchange of vibrational energy of different species, Equation 2.33.

$$\dot{w}_v = \dot{w}_{v-c} + \dot{w}_{v-t} + \dot{w}_{v-v} \tag{2.33}$$

The $\dot{w}_{v-c}$ term is used to model increase and decrease in vibrational energy due to chemical reactions. Generally, the dissociation reactions decrease the vibrational energy, and recombination reactions add more vibrational states. There are two

basic models to effects of reactions on the vibrational energy levels. These methods are known as preferential and nonpreferential models. As in Figure 2.1., higher vibrational states are closer to dissociate than lower vibrational states. Therefore, the preferential models consider the degree of vibrational states in the calculation of effects of chemical reactions on vibrational energy levels. However, it is assumed that all vibrational states have the same effects on dissociation reaction according to nonpreferential models. The removed vibrational energy in preferential model is more than that in the nonpreferential model so vibrational temperature has lower values behind the shock and dissociation reactions occur slowly [32]. Also, the effects of each vibrational states are getting closer with an increasing kinetic energy of the flow. Therefore, nonpreferential methods are chosen in this study for the sake of simplicity. Then, the source term,$\dot{w}_{v-c}$, can be obtained from multiplication of species chemical source terms, $\dot{w}_s$ and vibrational energies, Equation 2.34. To approach preferential model, Equation 2.34 is multiplied by a constant to obtain larger values, [30].

$$\dot{w}_{v-c} = \sum_{s} \dot{w}_s E_{v,s} \tag{2.34}$$

The second term, $\dot{w}_{v-t}$ is used to model energy exchange between vibrational and translational energies. This source term calculation is based on assumptions that oscillations are harmonic and also relaxation occurs in between adjacent vibrational levels. The consideration of relaxation is also based on diatomic molecules in heat bath where molecules are in equilibrium at each energy mode. The vibrational relaxation can be written as Equation 2.35 by using Maxwell- Boltzmann distribution. The vibrational energy with translational temperature is used as local equilibrium state where the nonequilibrium try to reach.

$$\dot{w}_{v-t} = \frac{dE_v}{dt} = \sum_{s}^{ns} \frac{E_{v,s}(T_{tr}) - E_{v,s}(T_v)}{\tau_s} \tag{2.35}$$

where τ is the relaxation time depending on pressure and temperature of heat bath. The most known relaxation time equation was developed by Landau –Teller

experimentally. Lee [33] offered the molar averaged relaxation time for Landau-Teller model, Equation 2.36.

$$\tau_s = \frac{\sum_s X_s}{\sum_s \frac{X_s}{\tau_{si}}} \tag{2.36}$$

The relaxation time obtained experimentally by Millikan- White [34] for each species can be written as in Equation 2.37. μ is the effective molecular weight. The unit of pressure is the atmosphere.

$$\tau_{si} = \frac{1}{P} e^{\left[A_{si}\left(T^{-1/3} - 0.015\mu_{si}^{1/4}\right) - 18.42\right]}$$

$$A_{si} \approx 1.16x10^{-3}\mu_{si}^{1/2}\theta^{4/3} \tag{2.37}$$

$$\mu_{si} = \frac{M_s M_i}{M_s + M_i}$$

Previous formulations are obtained by curve fitting up to 8000K. For the higher temperatures, Millikan- White gives over predicted relaxation time because assumptions done for harmonic oscillators fail. Therefore, Equation 2.37 requires correlation term for higher temperatures. Park [20] suggested molar averaged correction term based on limiting collision cross section, Equation 2.38.

$$\tau_P = \frac{1}{c_s \sigma_s N} \tag{2.38}$$

where c is the average molecular thermal speed and σ is limiting collision cross section founded empirically, Equation 2.39.

$$c_s = \sqrt{\frac{8R_u T}{\pi M_s}} \quad \text{and} \quad \sigma_s = 10^{-21}\left(\frac{50000}{T_{tr}}\right)^2 \tag{2.39}$$

N is the number density of flow field. Park correlation was developed for nitrogen flow, however it is also used for other species.

The last term, $\dot{w}_{v-v}$ is used to model vibrational energy exchange between molecules having different vibrational energy levels. P is the exchange probabilities determined experimentally, and N_a is the Avogadro numbers.

$$\dot{w}_{v-v,i} = \sum_{s}^{n_s} \left[N_a \sigma_s \sqrt{\frac{8}{\pi} \frac{RT}{\mu_s} \left(P_{si} \frac{\rho_s}{M_s} E_{v,s} - P_{is} \frac{\rho_s}{M_s} E_{v,s} \right)} \right] \tag{2.40}$$

The influence of vibrational- vibrational energy exchange is lower than the other source terms for vibrational energy [32]. Therefore, the exchanges between vibrational states of molecules are ignored in this study.

The vibrational temperature is obtained as in Equation 2.41 from Equation 2.31. However, this calculation misses trend of vibrational temperature. Therefore, Newton's method is used to obtain solution in a few iteration steps.

$$T_v = \left[\frac{\theta_v}{ln\left(\frac{R\theta_v}{E_v}\right)} \right] \tag{2.41}$$

The computation of vibrational temperature is the same with calculation of translational temperature. The calculation of the vibrational temperature with the Newton Raphson method is obtained as follows:

To compute vibrational temperature, a function or the simply residual can be written as:

$$R(T_v) = f(T_v) = \sum_{s=1}^{N_s} \frac{Y_s \mathrm{R_s} \theta_{\mathrm{v},s}}{\left(\mathrm{e}^{\frac{\theta_{\mathrm{v},s}}{\mathrm{T_v}}} - 1 \right)} - \mathrm{E_v} \tag{2.42}$$

The derivative of residual with respect to vibrational temperature:

$$\frac{\partial R}{\partial T_v} = \frac{\partial f}{\partial T_v} = \sum_{s=1}^{N_s} \frac{\mathrm{R_s}\theta_{\mathrm{v,s}}}{\left(\mathrm{e}^{\frac{\theta_{\mathrm{v,s}}}{\mathrm{T_v}}} - 1\right)}\left[\frac{\partial Y_s}{\partial T_v} + \frac{Y_s\theta_{\mathrm{v,s}}\mathrm{e}^{\frac{\theta_{\mathrm{v,s}}}{\mathrm{T_v}}}}{T_v^2\left(\mathrm{e}^{\frac{\theta_{\mathrm{v,s}}}{\mathrm{T_v}}} - 1\right)}\right] - \frac{\partial \mathrm{E_v}}{\partial T_v} \tag{2.43}$$

The derivative terms can be indicated as:

$$\frac{\partial Y_s}{\partial T_v} = \frac{Y_s^{n+1} - Y_s^n}{T_v^{n+1} - T_v^n} \quad \text{and} \quad \frac{\partial \mathrm{E_v}}{\partial T_v} = \frac{E_v^{n+1} - E_v^n}{T_v^{n+1} - T_v^n} \tag{2.44}$$

The mass fractions are assumed as equal to each other in each cell. Therefore, the first derivative term is zero.

Substituting the function and its derivative into Equation 2.17 can be obtained as:

$$T_v^{n+1} = T_v^n - \frac{\sum_{s=1}^{N_s} \frac{Y_s \mathrm{R_s}\theta_{\mathrm{v,s}}}{\left(\mathrm{e}^{\frac{\theta_{\mathrm{v,s}}}{\mathrm{T_v}}} - 1\right)} - \mathrm{E_v}}{\sum_{s=1}^{N_s} \frac{\mathrm{R_s}\theta_{\mathrm{v,s}}}{\left(\mathrm{e}^{\frac{\theta_{\mathrm{v,s}}}{\mathrm{T_v}}} - 1\right)}\left[\frac{Y_s\theta_{\mathrm{v,s}}\mathrm{e}^{\frac{\theta_{\mathrm{v,s}}}{\mathrm{T_v}}}}{T_v^2\left(\mathrm{e}^{\frac{\theta_{\mathrm{v,s}}}{\mathrm{T_v}}} - 1\right)}\right] - \frac{E_v^{n+1} - E_v^n}{T_v^{n+1} - T_v^n}} \tag{2.45}$$

The final formulation can be written as Equation 2.46.

$$T_v^{n+1} = T_v^n + \frac{E_v^{n+1} - \sum_s \frac{R_s\theta_{v,s}Y_s}{e^{\theta_{v,s}/T_v^n} - 1}}{\sum_s \frac{R_s\theta_{v,s}^2 Y_s^{n+1} e^{\theta_{v,s}/T_v^n}}{(T_v^n)^2\left(e^{\theta_{v,s}/T_v^n} - 1\right)^2}} \tag{2.46}$$

The results for various situations are given in the following chapter. The comparisons and explanations of the results are also mentioned in next chapter.

CHAPTER III

NUMERICAL MODELLING

3.1 Introduction

To achieve high accuracy, the physical model should be chosen in detail as much as possible. However, detailed physical formulation could be complex and difficult to model and to solve. Moreover, the consideration of nonequilibrium, real gas effects and chemical source terms increase the computational cost and numerical stiffness; thus, configurations of the numerical algorithm become difficult [17]. Euler equations are the simplified version of Navier- Stokes equations by ignoring viscous and heat flux terms. The governing equations are given as in Equations 2.1-5. In this study, three dimensional steady Euler equations are used. The Euler equations in Cartesian coordinate can be written as:

$$\frac{\partial \mathrm{F(w)}}{\partial \mathrm{x}} + \frac{\partial \mathrm{G(w)}}{\partial \mathrm{y}} + \frac{\partial \mathrm{H(w)}}{\partial \mathrm{z}} - S = 0 \qquad (3.1)$$

where w is the conservative flow variable vector, F, G and H are the flux vectors and S is the source term vector. These vectors can be written as:

$$w = \begin{bmatrix} \rho \\ \rho u \\ \rho v \\ \rho w \\ \rho E \\ \rho_1 \\ \vdots \\ \rho_s \\ \rho E_v \end{bmatrix} \quad F = \begin{bmatrix} \rho U \\ \rho u U + P \\ \rho v U \\ \rho w U \\ (\rho E + P)U \\ \rho_1 U \\ \vdots \\ \rho_s U \\ \rho E_v U \end{bmatrix} \quad G = \begin{bmatrix} \rho V \\ \rho u V \\ \rho v V + P \\ \rho w V \\ (\rho E + P)V \\ \rho_1 V \\ \vdots \\ \rho_s V \\ \rho E_v V \end{bmatrix} \quad (3.2)$$

$$F = \begin{bmatrix} \rho W \\ \rho u W \\ \rho v W \\ \rho w W + p \\ (\rho E + P)W \\ \rho_1 W \\ \vdots \\ \rho_s W \\ \rho E_v W \end{bmatrix} \quad S = \begin{bmatrix} 0 \\ 0 \\ 0 \\ 0 \\ 0 \\ \dot{w}_1 \\ \vdots \\ \dot{w}_s \\ \dot{w}_v \end{bmatrix}$$

There u, v and w are the component of velocity and U, V, and W are the contravariant velocities. To close the system of equations, these coupled equations require one more equation which is the equation of state.

In order to implement boundary conditions more accurately and efficiently the generalized coordinate system has been used. This chapter continues with transformation of physical space to computational domain, spatial discretization of flow variables and vectors. After that, flux splitting and higher order reconstruction of flow variables are presented. Also, Newton- GMRES solver and boundary conditions are described.

3.2 Spatial Discretization

According to chosen topology, CFD codes are separated into two categories: structured and unstructured. Although the unstructured grid generation requires less time and effort to generate cells around complex geometries, the structured grid generation generally has advantages in CPU time and accuracy. Moreover, residual calculation requires information from neighborhood cells. Therefore, unstructured grid needs storage of the indices or indicator of each cell to get information from

neighbor cells whereas it can be easily achieved by reducing or adding one to indices in structured topology. In this study, structured mesh are used to reduce numerical modeling complexity and to save accuracy.

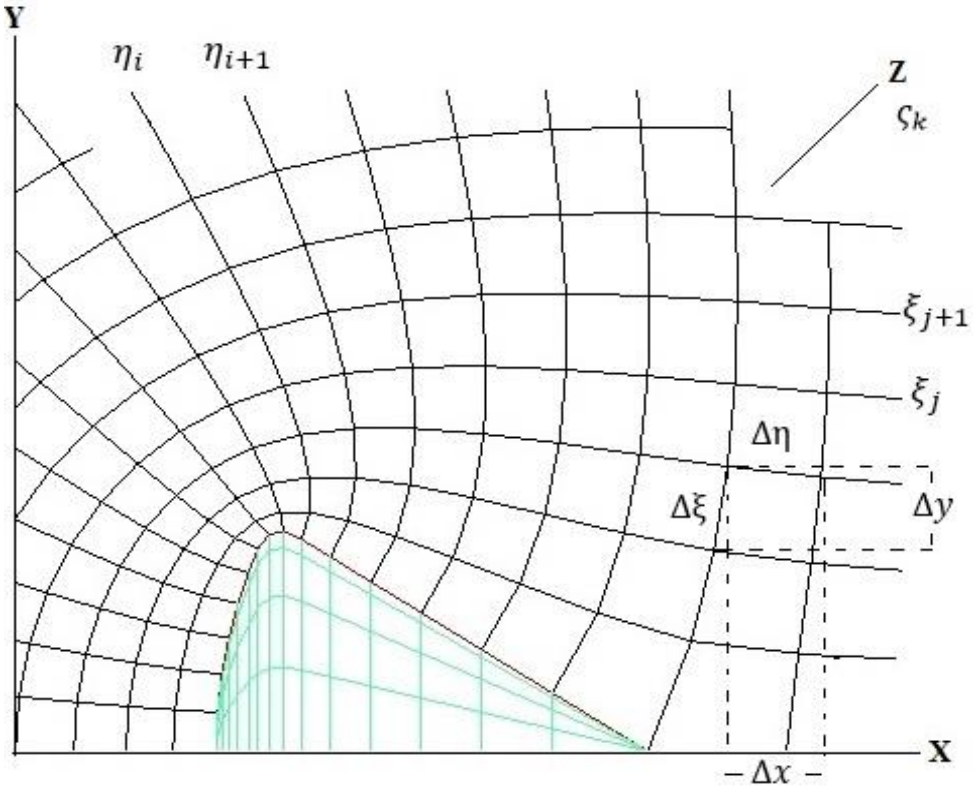

Figure 3.1. The representation of physical space around Apollo Command Module

In Figure 3.1, physical space around the sketch of Apollo Command Module is represented. The transformation from physical space (x, y, z) to computational space (η, ξ, ς) are achieved by metrics. The general transformation and inverse of it are obtained from the following equations.

$$\begin{aligned} x &= x(\eta,\xi,\varsigma) & \eta &= \eta(x,y,z) \\ y &= y(\eta,\xi,\varsigma) & \xi &= \xi(x,y,z) \\ z &= z(\eta,\xi,\varsigma) & \varsigma &= \varsigma(x,y,z) \end{aligned} \tag{3.3}$$

The application of chain rule yields the following equation, Equation 3.4. The evaluation of metrics is required to solve governing equations.

$$\frac{\partial F}{\partial \eta}\frac{\partial \eta}{\partial x}+\frac{\partial F}{\partial \xi}\frac{\partial \xi}{\partial x}+\frac{\partial F}{\partial \varsigma}\frac{\partial \varsigma}{\partial x}+\frac{\partial G}{\partial \eta}\frac{\partial \eta}{\partial y}+\frac{\partial G}{\partial \xi}\frac{\partial \xi}{\partial y}+\frac{\partial G}{\partial \varsigma}\frac{\partial \varsigma}{\partial z}+\frac{\partial H}{\partial \eta}\frac{\partial \eta}{\partial z}$$
$$+\frac{\partial H}{\partial \xi}\frac{\partial \xi}{\partial z}+\frac{\partial H}{\partial \varsigma}\frac{\partial \varsigma}{\partial z} \tag{3.4}$$
$$=\frac{\partial F}{\partial \eta}\eta_x+\frac{\partial F}{\partial \xi}\xi_x+\frac{\partial F}{\partial \varsigma}\varsigma_x+\frac{\partial G}{\partial \eta}\eta_y+\frac{\partial G}{\partial \xi}\xi_y+\frac{\partial G}{\partial \varsigma}\varsigma_y+\frac{\partial H}{\partial \eta}\eta_z$$
$$+\frac{\partial H}{\partial \xi}\xi_z+\frac{\partial H}{\partial \varsigma}\varsigma_z$$
$$=S$$

The transformation from body fitted physical space base on assumption that partial derivatives of physical space coordinates with respect to computational domain coordinates and vice versa are defined and are continuous. Thus, following linear equations can be written as:

$$\begin{bmatrix}\partial x\\ \partial y\\ \partial z\end{bmatrix}=\begin{bmatrix}x_\eta & x_\eta & x_\eta\\ y_\xi & y_\xi & y_\xi\\ z_\varsigma & z_\varsigma & z_\varsigma\end{bmatrix}\begin{bmatrix}\partial \eta\\ \partial \xi\\ \partial \varsigma\end{bmatrix}=[J]\begin{bmatrix}\partial \eta\\ \partial \xi\\ \partial \varsigma\end{bmatrix}, \tag{3.5}$$
$$\begin{bmatrix}\partial \eta\\ \partial \xi\\ \partial \varsigma\end{bmatrix}=\begin{bmatrix}\eta_x & \eta_y & \eta_z\\ \xi_x & \xi_y & \xi_z\\ \varsigma_x & \varsigma_y & \varsigma_z\end{bmatrix}\begin{bmatrix}\partial x\\ \partial y\\ \partial z\end{bmatrix}=[J^{-1}]\begin{bmatrix}\partial x\\ \partial y\\ \partial z\end{bmatrix}$$

J and J^{-1} are known as the Jacobian matrices of the transformation, and their elements are related each other as:

$$[J]=\frac{Transpose\ of\ cofactor\ J^{-1}}{|J^{-1}|}=\frac{\partial(\eta,\xi,\varsigma)}{\partial(x,y,z)}$$
$$=\frac{1}{x_\eta(z_\varsigma y_\xi-z_\xi y_\varsigma)-x_\xi(z_\varsigma y_\eta-z_\eta y_\varsigma)+x_\varsigma(z_\xi y_\eta-z_\eta y_\xi)} \tag{3.6}$$

Therefore, each metric $(\eta_x, \eta_y, \eta_z, \xi_x, \xi_y, \xi_z, \varsigma_x, \varsigma_y, \varsigma_z)$ can be written easily from Equation 3.6. Basically, Jacobian matrices are obtained from the ratio of the volumes of computational space to physical spaces [36]. Substituting metrics with Equation 3.4 yields:

$$\frac{\partial \check{F}(\mathrm{w})}{\partial \eta} + \frac{\partial \check{G}(\mathrm{w})}{\partial \xi} + \frac{\partial \check{H}(\mathrm{w})}{\partial \varsigma} - \check{S} = 0 \tag{3.7}$$

The flow variables, flux and source term vectors in computational space are written as in following equations.

$$\check{w} = \frac{1}{|J|}\begin{bmatrix} \rho \\ \rho u \\ \rho v \\ \rho w \\ \rho E \\ \rho_1 \\ \vdots \\ \rho_s \\ \rho E_v \end{bmatrix} \qquad \check{F} = \frac{1}{|J|}\begin{bmatrix} \rho U \\ \rho u U + P\eta_x \\ \rho v U + P\eta_y \\ \rho w U + P\eta_z \\ (\rho E + P)U \\ \rho_1 U \\ \vdots \\ \rho_s U \\ \rho E_v U \end{bmatrix} \qquad \check{S} = \frac{1}{|J|}\begin{bmatrix} 0 \\ 0 \\ 0 \\ 0 \\ 0 \\ \dot{w}_1 \\ \vdots \\ \dot{w}_s \\ \dot{w}_v \end{bmatrix} \tag{3.8}$$

$$\check{G} = \frac{1}{|J|}\begin{bmatrix} \rho V \\ \rho u V + P\xi_x \\ \rho v V + P\xi_y \\ \rho w V + P\xi_z \\ (\rho E + P)V \\ \rho_1 V \\ \vdots \\ \rho_s V \\ \rho E_v V \end{bmatrix} \qquad \check{F} = \frac{1}{|J|}\begin{bmatrix} \rho W \\ \rho u W + P\varsigma_x \\ \rho v W + P\varsigma_y \\ \rho w W + P\varsigma_z \\ (\rho E + P)W \\ \rho_1 W \\ \vdots \\ \rho_s W \\ \rho E_v W \end{bmatrix}$$

The transformed computational domain is discretized by using Finite Volume Method (FVM). In this method, computational spaces are divided into discrete control volumes and these control volumes do not overlap.

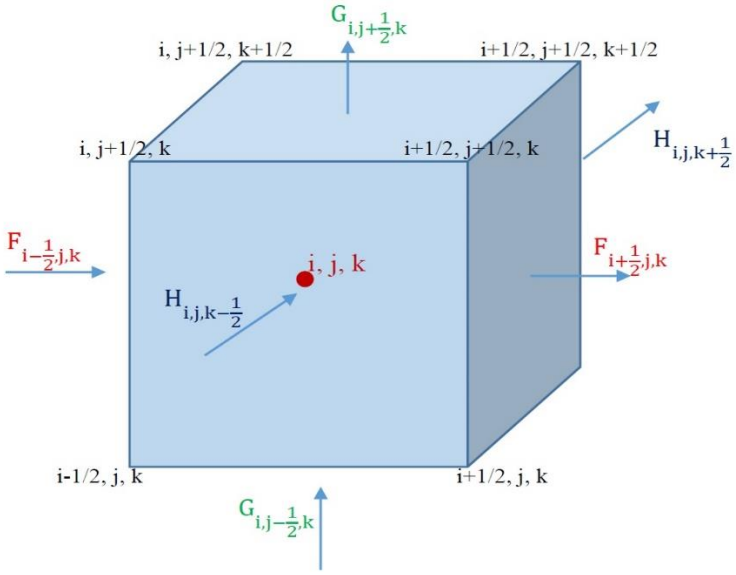

Figure 3.2. Control volume and flux vectors around control volume

The three dimensional control volume is shown in Figure 3.2. Flux vectors are evaluated at the surface of the control volume. Basically, conservation laws physically state that net flux rate leaving the control volume must be equal to the rate of flux generated in the control volume.

$$\delta_\eta \check{F} = \check{F}_{i+\frac{1}{2},j,k} - \check{F}_{i-\frac{1}{2},j,k}$$

$$\delta_\xi \check{G} = \check{G}_{i,j+\frac{1}{2},k} - \check{G}_{i,j-\frac{1}{2},k} \qquad (3.9)$$

$$\delta_\varsigma \check{H} = \check{H}_{i,j,k+\frac{1}{2}} - \check{H}_{i,j,k-\frac{1}{2}}$$

where δ is the distance between nodal points. The discretized form of the Equation 3.7 can be written as in Equation 3.10.

$$\frac{\partial_\eta \check{F}(\breve{w})}{\Delta\eta} + \frac{\partial_\xi \check{G}(\breve{w})}{\Delta\xi} + \frac{\partial_\varsigma \check{H}(\breve{w})}{\partial\varsigma} - \check{S} = 0 \qquad (3.10)$$

The substitution Equation 3.9 in Equation 3.10 yields the following equation, Equation 3.11. Also, the computational domain is equally spaced in each direction. The chemical and vibrational source terms are computed at cell centers, therefore the discretization of the source vector is not necessary.

$$\left(\check{\mathrm{F}}_{\mathrm{i}+\frac{1}{2},\mathrm{j},\mathrm{k}} - \check{\mathrm{F}}_{\mathrm{i}-\frac{1}{2},\mathrm{j},\mathrm{k}}\right) + \left(\check{\mathrm{G}}_{\mathrm{i},\mathrm{j}+\frac{1}{2},\mathrm{k}} - \check{\mathrm{G}}_{\mathrm{i},\mathrm{j}-\frac{1}{2},\mathrm{k}}\right) + \left(\check{\mathrm{H}}_{\mathrm{i},\mathrm{j},\mathrm{k}+\frac{1}{2}} - \check{\mathrm{H}}_{\mathrm{i},\mathrm{j},\mathrm{k}-\frac{1}{2}}\right) - \check{S}_{i,j,k} = 0 \tag{3.11}$$

The flux calculation requires considering the interactions of neighborhood cells at the control volume surface. There are many schemes to evaluate face values of fluxes such as: upwind, central differencing, second order upwind, power-law scheme and Quick schemes. In this study, first and higher order upwind schemes are used to make assumptions about variation of flow variables between the neighbor cell centers.

The evaluation of fluxes at cell surfaces requires flow variable interpolation from left and right cells. The fluxes in the Equation 3.11 can be expanded as:

$$\begin{aligned}\check{\mathrm{F}}_{\mathrm{i}+\frac{1}{2},\mathrm{j},\mathrm{k}} &= \check{F}^{+}\left(\breve{w}^{-}{}_{i+\frac{1}{2},j,k}\right) + \check{F}^{-}\left(\breve{w}^{+}{}_{i+\frac{1}{2},j,k}\right)\\ \check{\mathrm{F}}_{\mathrm{i}-\frac{1}{2},\mathrm{j},\mathrm{k}} &= \check{F}^{+}\left(\breve{w}^{-}{}_{i-\frac{1}{2},j,k}\right) + \check{F}^{-}\left(\breve{w}^{+}{}_{i-\frac{1}{2},j,k}\right)\end{aligned} \tag{3.12}$$

The values of flow variables at cell surfaces are obtained by interpolation of the values. The order of the interpolation is an important factor on convergence. The simplest interpolation is the first order interpolation in which values are obtained from neighbor cells, Equation 3.13.

$$\begin{aligned}\breve{w}^{-}{}_{i+\frac{1}{2},j,k} &= \breve{w}_{i,j,k}\\ \breve{w}^{+}{}_{i+\frac{1}{2},j,k} &= \breve{w}_{i+1,j,k}\end{aligned} \tag{3.13}$$

3.3 Higher Order Reconstruction

In the previous parts, finite volume method and first order spatial discretization are presented. Flow variables are assumed as constant in each computational cell, and fluxes are computed at the interface of the cells. For the first order accurate interpolation, flow variables are obtained from left and right neighbor cells. Therefore, accuracy of the first order schemes are not good as higher order schemes, because higher order interpolation of flow variables base on the fact that flow variables are not constant in the computational cell volume [37].

The Monotonic Upwind Scheme for Conservation Laws (MUSCL) was developed by van Leer [37] to obtain second order spatial accuracy. MUSCL schemes can be written as:

$$\breve{w}^{-}_{i+\frac{1}{2},j,k} = \breve{w}_{i,j,k} + \frac{1}{4}[(1-\kappa)\nabla_i + (1+\kappa)\Delta_i]$$
$$\breve{w}^{+}_{i+\frac{1}{2},j,k} = \breve{w}_{i+1,j,k} - \frac{1}{4}[(1-\kappa)\Delta_{i+1} + (1+\kappa)\nabla_i] \quad (3.14)$$

∇ and Δ are the backward and forward operators, and they are defined as Equation 3.15.

$$\nabla_i = \breve{w}_{i,j,k} - \breve{w}_{i-1,j,k} \quad , \quad \Delta_i = \breve{w}_{i+1,j,k} - \breve{w}_{i,j,k} \quad (3.15)$$

κ is an important factor on the order of accuracy and type of spatial discretization. κ has values in between -1 and 1.

Higher order spatial discretization generates oscillations at regions where gradients are high due to shock, and numerical solver cannot handle these oscillations. Flux limiters are used to prevent oscillations from sharp changes. Flux limiters are functions of the local consecutive gradient parameter which is obtained by taking ratio of upstream flow variable gradient to downstream flow variable gradient, Equation 3.16.

$$r_i = \frac{\breve{w}_{i,j,k} - \breve{w}_{i-1,j,k}}{\breve{w}_{i+1,j,k} - \breve{w}_{i,j,k}} = \frac{\nabla_i}{\Delta_i} \tag{3.16}$$

The MUSCL scheme with limiter functions, $\phi(r)$ can be written as following equation:

$$\begin{aligned} \breve{w}^{-}{}_{i+\frac{1}{2},j,k} &= \breve{w}_{i,j,k} + \frac{\phi(r_i)}{4}[(1-\kappa)\nabla_i + (1+\kappa)\Delta_i] \\ \breve{w}^{+}{}_{i+\frac{1}{2},j,k} &= \breve{w}_{i+1,j,k} - \frac{\phi(r_{i+1})}{4}[(1-\kappa)\Delta_{i+1} + (1+\kappa)\nabla_{i+1}] \end{aligned} \tag{3.17}$$

When the flow field has large gradient of the flow variable, there are also big differences between forward and backward surface of the cells. Due to this large gradient, MUSCL scheme interpolation cannot work properly. Therefore, MUSCL scheme has undershoot or overshoot interpolation so oscillations and instabilities occur [36]. There are various flux limiters which are min-mod, Superbee, Van Leer, Van Albada and, Venkatakrishnan limiters to prevent oscillations.

In this study, Van Albada [38] and the modified Van Albada limiter by Venkatakrishnan [39] are used. The Van Albada flux limiter can be defined as:

$$\Phi(r_i) = \frac{r_i^2 + \mathrm{r}_i}{r_i^2 + 1} \tag{3.18}$$

Basically, at the smooth regions, values of limiter should approach one, where flux limiters should be turned off. The flux limiter generates oscillations and instabilities at nearly smooth regions. Venkatakrishnan introduced modified Van Albada limiter; thus, MUSCL scheme do not apply limiter through almost smooth regions. Venkatakrishnan flux limiter can be described by the following equations where Equation 3.17 is rearranged as following Equation 3.19:

$$\breve{w}^{-}_{i+\frac{1}{2},j,k} = \breve{w}_{i,j,k} + \frac{1}{2}\phi(r_i)\nabla_i = \breve{w}_{i,j,k} + \Psi(r_i)$$
$$\breve{w}^{+}_{i+\frac{1}{2},j,k} = \breve{w}_{i+1,j,k} - \frac{1}{2}\phi(r_{i+1})\Delta_{i+1} = \breve{w}_{i+1,j,k} + \Psi(r_{i+1}) \quad (3.19)$$

Ψ values can be written for the left surface of the cells with two different κ values.

$$\Psi(r_i) = \frac{(\Delta_i^2 + \epsilon)\nabla_i + (\nabla_i^2 + \epsilon)\Delta_i}{\nabla_i^2 + \Delta_i^2 + 2\epsilon} \qquad for\ \kappa = 0$$
$$\Psi(r_i) = \frac{(2\Delta_i^2 + \epsilon)\nabla_i + (\nabla_i^2 + 2\epsilon)\Delta_i}{\nabla_i^2 + \Delta_i^2 - \nabla_i\Delta_i + 3\epsilon} \qquad for\ \kappa = 1/3 \quad (3.20)$$

The small term ($\epsilon = 1x10^{-12}$) is added to the nominator and denominator to prevent division by zero at smooth gradient regions. After completion of the spatial discretization, fluxes can be splitted.

3.4 Flux Splitting

The flux vectors, $\breve{F}$, $\breve{G}$ and $\breve{H}$ are homogenous functions of flow variable, $\breve{w}$ according to the Euler theorem.

$$\frac{\partial \breve{F}}{\partial \breve{w}}\frac{\partial \breve{w}}{\partial \eta} + \frac{\partial \breve{G}}{\partial \breve{w}}\frac{\partial \breve{w}}{\partial \xi} + \frac{\partial \breve{H}}{\partial \breve{w}}\frac{\partial \breve{w}}{\partial \varsigma} = \breve{A}\frac{\partial \breve{w}}{\partial \eta} + \breve{B}\frac{\partial \breve{w}}{\partial \xi} + \breve{C}\frac{\partial \breve{w}}{\partial \varsigma} = \breve{S} \quad (3.21)$$

$\breve{A}, \breve{B}$ and $\breve{C}$ are the Jacobian matrices. To solve linear system of equations eigenvalues and eigenvectors of Jacobian matrices should be obtained. At this point, matrix M having eigenvector as elements should be defined.

$$\breve{A} = M_{\breve{A}}\Lambda_{\breve{A}}M_{\breve{A}}^{-1} \text{ and } \breve{F} = M_{\breve{A}}\Lambda_{\breve{A}}M_{\breve{A}}^{-1}\breve{w} \quad (3.22)$$

The splitting eigenvalue vector, Λ according to positive and negative entries yields two new matrices composing Λ. For the Euler equations, eigenvalue splitting is

based on velocity splitting. The flux vector with splitted eigenvectors can be written as:

$$\check{F} = M_{\check{A}}\,\Lambda_{\check{A}}^{-}\,M_{\check{A}}^{-1}\breve{w} + M_{\check{A}}\,\Lambda_{\check{A}}^{+}\,M_{\check{A}}^{-1}\breve{w} = \check{A}^{-}\breve{w} + \check{A}^{+}\breve{w} = \check{F}^{-} + \check{F}^{+}$$

$$\check{G} = M_{\check{B}}\,\Lambda_{\check{B}}^{-}\,M_{\check{B}}^{-1}\breve{w} + M_{\check{B}}\,\Lambda_{\check{B}}^{+}\,M_{\check{B}}^{-1}\breve{w} = \check{B}^{-}\breve{w} + \check{B}^{+}\breve{w} = \check{G}^{-} + \check{G}^{+} \qquad (3.23)$$

$$\check{F} = M_{\check{C}}\,\Lambda_{\check{C}}^{-}\,M_{\check{C}}^{-1}\breve{w} + M_{\check{C}}\,\Lambda_{\check{C}}^{+}\,M_{\check{C}}^{-1}\breve{w} = \check{C}^{-}\breve{w} + C^{+}\breve{w} = \breve{H}^{-} + \breve{H}^{+}$$

At the cell faces, $\check{F}^{+}$ propagates information left to right and $\breve{w}^{-}$ values are obtained from the left face of the computational cells. Similarly, $\check{F}^{-}$ propagates information right to left and $\breve{w}^{+}$ values are obtained from the right face of the computational cells. In the computation of the splitted flux vector, corresponding splitted flow variables are used. Then, final formulation in (i, j, k) cell can be obtained as:

$$\begin{aligned}
&\left[\check{F}^{+}\left(\breve{w}^{-}{}_{i+\frac{1}{2},j,k}\right) + \check{F}^{-}\left(\breve{w}^{+}{}_{i+\frac{1}{2},j,k}\right)\right] \\
&\qquad - \left[\check{F}^{+}\left(\breve{w}^{-}{}_{i-\frac{1}{2},j,k}\right) + \check{F}^{-}\left(\breve{w}^{+}{}_{i-\frac{1}{2},j,k}\right)\right] \\
&+ \left[\check{G}^{+}\left(\breve{w}^{-}{}_{i,j+\frac{1}{2},k}\right) + \check{G}^{-}\left(\breve{w}^{+}{}_{i,j+\frac{1}{2},k}\right)\right] \\
&\qquad - \left[\check{G}^{+}\left(\breve{w}^{-}{}_{i,j-\frac{1}{2},k}\right) + \check{G}^{-}\left(\breve{w}^{+}{}_{i,j-\frac{1}{2},k}\right)\right] \\
&+ \left[\breve{H}^{+}\left(\breve{w}^{-}{}_{i,j,k+\frac{1}{2}}\right) + \breve{H}^{-}\left(\breve{w}^{+}{}_{i,j,k+\frac{1}{2}}\right)\right] \\
&\qquad - \left[\breve{H}^{+}\left(\breve{w}^{-}{}_{i,j,k-\frac{1}{2}}\right) + \breve{H}^{-}\left(\breve{w}^{+}{}_{i,j,k-\frac{1}{2}}\right)\right] = \check{S}_{i,j,k}
\end{aligned} \qquad (3.24)$$

The basic upwind flux splitting scheme is written as in Equation 3.24. The aim of the flux vector splitting is to obtain proper physical propagation of the flow variable throughout flow. There are various flux splitting method developed for Euler equations. In this study, Van Leer, Steger- Warming and the Advection Upstream Splitting Method (AUSM) are used.

3.4.1 Van Leer Flux Splitting

In this study, both ideal and real gas assumptions are used for flow field calculations. There are some differences in the flux vectors with ideal and real gas assumptions. Van Leer states that Steger-Warming splitting schemes are not differentiable at stagnation and sonic regions [40]. Van Leer scheme is based on Jacobian vector splitting, and derivatives are assumed as continuous.

$$M = M^{+} + M^{-}$$

$$M^{\pm} = \begin{cases} \pm\frac{1}{4}(M \pm 1)^2 & |M| \leq 1 \\ \frac{1}{2}(M \pm |M|) & otherwise \end{cases} \tag{3.25}$$

Van Leer splitting can be done according to Mach number splitting. For the supersonic flow, whole scalar value of Mach number is directed to downstream. For the subsonic regions, the Mach number splitting is done with respect to Equation 3.25.

Splitted flux vector in the supersonic regions can be obtained as:

$$\check{F}^{+} = \check{F} \text{ and } \check{F}^{-} = 0 \quad \text{for u} \geq \text{a}$$

$$\check{F}^{-} = \check{F} \text{ and } \check{F}^{+} = 0 \quad \text{for u} \leq -\text{a} \tag{3.26}$$

Splitted flux vector in the subsonic regions is given by the following equation:

$$\check{F}^{\pm} = \rho a \frac{(M \pm 1)^2}{\gamma} \begin{bmatrix} 1 \\ \left(\frac{-\breve{U} \pm 2a}{\gamma}\right)\check{k}_{x,1} + u \\ \left(\frac{-\breve{U} \pm 2a}{\gamma}\right)\check{k}_{x,2} + v \\ \left(\frac{-\breve{U} \pm 2a}{\gamma}\right)\check{k}_{x,3} + w \\ \left(\frac{-\breve{U} \pm 2a}{\gamma+1}\right)\breve{U} + \frac{2a^2}{\gamma-1} + \frac{u^2+v^2+w^2}{2} \end{bmatrix} \quad (3.27)$$

In the above equations, a is the Mach number. k is the directional cosine vectors and $\breve{U}$ is the contravariant velocity, Equation 3.28.

$$\check{k}_{x,j} = \frac{\eta_{x^j}}{\sqrt{\eta_x^2 + \eta_y^2 + \eta_z^2}} \quad , \qquad \check{k}_{y,j} = \frac{\xi_{x^j}}{\sqrt{\xi_x^2 + \xi_y^2 + \xi_z^2}} \quad ,$$

$$\check{k}_{z,j} = \frac{\varsigma_{z^j}}{\sqrt{\varsigma_x^2 + \varsigma_y^2 + \varsigma_z^2}} \quad (3.28)$$

$$\breve{U}_{x^j} = u\check{k}_{x^j,1} + v\check{k}_{x^j,2} + w\check{k}_{x^j,3}$$

The previous formulation is written for ideal gas assumptions where gas has constant specific heat ratio. For the real gas assumption, specific heat constant varies in each cell; it is function of pressure and temperature. Moreover, real gas effects are important during the chemical and vibrational nonequilibrium; thus, chemical and vibrational terms are included in the following formulation. For the real gas assumption, flux vector is assumed as:

$$\check{F} = \check{F}\left[\rho, a, M, {}^{\rho_i}/_{\rho}, E, E_v\right] \quad (3.29)$$

Speed of sound for ideal gas is simply obtained from $a^2 = \gamma RT$. For the real gas, speed of sound is obtained from:

$$a^2 = \frac{\partial P}{\partial \rho} + \frac{P}{\rho^2}\frac{\partial P}{\partial e} \tag{3.30}$$

The partial derivatives of pressure with respect to ρ and e can be obtained from pressure equation, $P = (\gamma - 1)\rho e$. The specific heat constant is also function of density and energy, therefore Equation 3.30 can be written as:

$$a^2 = \frac{\gamma P}{\rho} + e\left[(\gamma - 1)\mathrm{e}\frac{\partial \gamma}{\partial \mathrm{e}} + \rho\frac{\partial \gamma}{\partial \mathrm{P}}\right] = \Gamma(\gamma - 1)\mathrm{e} \tag{3.31}$$

Liou, Leer and Shuen [40] introduces a new auxiliary variable, Γ which is also function of density and energy. Also, specific heat constant is calculated in each cell at each iteration. Thus, Van Leer flux splitting algorithm for real gas with nonequilibrium physics are obtained as in Equation 3.32 by considering Leer [40] and Grossman and Cinnella [41] studies.

For subsonic regions, splitted flux vector can be written as:

$$\check{F}^{\pm} = \rho a(M \pm 1)^2 \begin{bmatrix} 1 \\ \left[u - \check{k}_{x,1}\left(\breve{U} \pm 2a\right)\frac{P}{\rho a^2}\right] \\ \left[v - \check{k}_{x,2}\left(\breve{U} \pm 2a\right)\frac{P}{\rho a^2}\right] \\ \left[w - \check{k}_{x,3}\left(\breve{U} \pm 2a\right)\frac{P}{\rho a^2}\right] \\ H - m\left(\breve{U} \pm a\right)^2 \\ \rho_1/\rho \\ \vdots \\ \rho_s/\rho \\ E_v \end{bmatrix} \tag{3.32}$$

where m is given as $m = \frac{h/a^2}{1+2h/a^2}$. It is suggested that choosing m values as 0 to obtain efficient and the simplest formulation [40]. In this study, *m* is chosen as zero. For supersonic regions, the same manner with ideal gas assumption is applicable.

3.4.2 Steger- Warming Flux Splitting

Steger- Warming splitting is another upwind flux splitting method based on eigenvalue splitting. It simply splits with diagonalizing of Jacobian matrices with eigenvectors as in Equation 3.23. Euler equations have three eigenvalues at each direction: $u, (u+a)$ and $(u-a)$. Splitted eigenvalues can be written as:

$$\lambda_1^{\pm} = \frac{u \pm |u|}{2} \qquad \lambda_2^{\pm} = \frac{(u+a) \pm |u+a|}{2}$$
$$\lambda_3^{\pm} = \frac{(u-a) \pm |u-a|}{2} \tag{3.33}$$

For the ideal gas assumptions, Steger and Warming introduce a new splitting method as in Equation 3.34 in 1981 [42].

$$\check{F}^{\pm} = \frac{\rho}{2\gamma}$$

$$\begin{bmatrix} \left[2(\gamma-1)\lambda_1^{\pm} + \lambda_2^{\pm} + \lambda_3^{\pm}\right] \\ \left[2(\gamma-1)\lambda_1^{\pm} + \lambda_2^{\pm} + \lambda_3^{\pm}\right]u + a\left(\lambda_2^{\pm} - \lambda_3^{\pm}\right)\check{k}_{x,1} \\ \left[2(\gamma-1)\lambda_1^{\pm} + \lambda_2^{\pm} + \lambda_3^{\pm}\right]v + a\left(\lambda_2^{\pm} - \lambda_3^{\pm}\right)\check{k}_{x,2} \\ \left[2(\gamma-1)\lambda_1^{\pm} + \lambda_2^{\pm} + \lambda_3^{\pm}\right]w + a\left(\lambda_2^{\pm} - \lambda_3^{\pm}\right)\check{k}_{x,3} \\ \left[2(\gamma-1)\lambda_1^{\pm} + \lambda_2^{\pm} + \lambda_3^{\pm}\right]\dfrac{u^2+v^2+w^2}{2} + aU\left(\lambda_2^{\pm} - \lambda_3^{\pm}\right) + a^2\dfrac{\lambda_2^{\pm} + \lambda_3^{\pm}}{\gamma-1} \end{bmatrix} \tag{3.34}$$

Steger- Warming flux splitting has discontinuities at sonic and at stagnation points in the calculation of derivations of flow vectors to flow variables. Therefore, there are oscillations at those discontinuous regions. To get rid of oscillations, a small number can be added to eigenvalue splitting as in Equation 3.35.

$$\lambda_1^{\pm} = \frac{\lambda_1 \pm \sqrt{{\lambda_1}^2 + \varepsilon^2}}{2} \tag{3.35}$$

Steger-Warming flux-vector splitting scheme with extension to nonequilibrium flows can be obtained as implementations by Liou, Leer & Shuen [43] and Grossman & Cinnella [43] in their studies, as shown in Equation 3.36.

$$\check{\mathrm{F}}^{\pm} = \frac{1}{\mathrm{a}^2} x \tag{3.36}$$

$$\begin{bmatrix} \lambda_1^{\pm}\frac{\mathrm{P}}{\rho}\frac{\partial \mathrm{P}}{\partial \mathrm{e}} + \frac{\lambda_2^{\pm}}{2}\left(\rho\mathrm{a}^2 - \frac{\mathrm{P}}{\rho}\frac{\partial \mathrm{P}}{\partial \mathrm{e}}\right) + \frac{\lambda_3^{\pm}}{2}\left(\rho\mathrm{a}^2 - \frac{\mathrm{P}}{\rho}\frac{\partial \mathrm{P}}{\partial \mathrm{e}}\right) \\ \lambda_1^{\pm}\frac{\mathrm{uP}}{\rho}\frac{\partial \mathrm{P}}{\partial \mathrm{e}} + \frac{\lambda_2^{\pm}}{2}\frac{\left(\mathrm{u} + \mathrm{a}\check{\mathrm{k}}_{\mathrm{x},1}\right)}{2}\left(\rho\mathrm{a}^2 - \frac{\mathrm{P}}{\rho}\frac{\partial \mathrm{P}}{\partial \mathrm{e}}\right) + \frac{\lambda_3^{\pm}}{2}\frac{\left(\mathrm{u} + \mathrm{a}\check{\mathrm{k}}_{\mathrm{x},1}\right)}{2}\left(\rho\mathrm{a}^2 - \frac{\mathrm{P}}{\rho}\frac{\partial \mathrm{P}}{\partial \mathrm{e}}\right) \\ \lambda_1^{\pm}\frac{\mathrm{vP}}{\rho}\frac{\partial \mathrm{P}}{\partial \mathrm{e}} + \frac{\lambda_2^{\pm}}{2}\frac{\left(\mathrm{v} + \mathrm{a}\check{\mathrm{k}}_{\mathrm{x},2}\right)}{2}\left(\rho\mathrm{a}^2 - \frac{\mathrm{P}}{\rho}\frac{\partial \mathrm{P}}{\partial \mathrm{e}}\right) + \frac{\lambda_3^{\pm}}{2}\frac{\left(\mathrm{v} + \mathrm{a}\check{\mathrm{k}}_{\mathrm{x},2}\right)}{2}\left(\rho\mathrm{a}^2 - \frac{\mathrm{P}}{\rho}\frac{\partial \mathrm{P}}{\partial \mathrm{e}}\right) \\ \lambda_1^{\pm}\frac{\mathrm{wP}}{\rho}\frac{\partial \mathrm{P}}{\partial \mathrm{e}} + \frac{\lambda_2^{\pm}}{2}\frac{\left(\mathrm{w} + \mathrm{a}\check{\mathrm{k}}_{\mathrm{x},3}\right)}{2}\left(\rho\mathrm{a}^2 - \frac{\mathrm{P}}{\rho}\frac{\partial \mathrm{P}}{\partial \mathrm{e}}\right) + \frac{\lambda_3^{\pm}}{2}\frac{\left(\mathrm{w} + \mathrm{a}\check{\mathrm{k}}_{\mathrm{x},3}\right)}{2}\left(\rho\mathrm{a}^2 - \frac{\mathrm{P}}{\rho}\frac{\partial \mathrm{P}}{\partial \mathrm{e}}\right) \\ \lambda_1^{\pm}\left(\frac{\mathrm{P}}{\rho}\frac{\partial \mathrm{P}}{\partial \mathrm{e}}H - \rho\mathrm{a}^2\right) + \lambda_2^{\pm}\frac{(\mathrm{H} + \mathrm{ua})}{2}\left(\rho\mathrm{a}^2 - \frac{\mathrm{P}}{\rho}\frac{\partial \mathrm{P}}{\partial \mathrm{e}}\right) + \lambda_3^{\pm}\frac{(\mathrm{H} - \mathrm{ua})}{2}\left(\rho\mathrm{a}^2 - \frac{\mathrm{P}}{\rho}\frac{\partial \mathrm{P}}{\partial \mathrm{e}}\right) \\ {\rho_1}/{\rho}\left[\lambda_1^{\pm}\frac{\mathrm{P}}{\rho}\frac{\partial \mathrm{P}}{\partial \mathrm{e}} + \frac{\lambda_2^{\pm}}{2}\left(\rho\mathrm{a}^2 - \frac{\mathrm{P}}{\rho}\frac{\partial \mathrm{P}}{\partial \mathrm{e}}\right) + \frac{\lambda_3^{\pm}}{2}\left(\rho\mathrm{a}^2 - \frac{\mathrm{P}}{\rho}\frac{\partial \mathrm{P}}{\partial \mathrm{e}}\right)\right] \\ \vdots \\ {\rho_s}/{\rho}\left[\lambda_1^{\pm}\frac{\mathrm{P}}{\rho}\frac{\partial \mathrm{P}}{\partial \mathrm{e}} + \frac{\lambda_2^{\pm}}{2}\left(\rho\mathrm{a}^2 - \frac{\mathrm{P}}{\rho}\frac{\partial \mathrm{P}}{\partial \mathrm{e}}\right) + \frac{\lambda_3^{\pm}}{2}\left(\rho\mathrm{a}^2 - \frac{\mathrm{P}}{\rho}\frac{\partial \mathrm{P}}{\partial \mathrm{e}}\right)\right] \end{bmatrix}$$

The splitting for ideal gas assumptions can be derived from Equation 3.36 simply by taking the derivatives with respect to ideal gas equations. There are still discontinuities at sonic and stagnation points.

3.5 Flow Solver

After the implementation of spatial discretization and flux splitting, the Newton GMRES method can be applied. The nonlinear governing equations can be written as in following Equation 3.37 where $\check{R}$ is the residual vector.

$$\check{R}(\breve{w}) = \frac{\partial \check{F}(\mathrm{w})}{\partial \eta} + \frac{\partial \check{G}(\mathrm{w})}{\partial \xi} + \frac{\partial \check{H}(\mathrm{w})}{\partial \varsigma} - \check{S} = 0 \tag{3.37}$$

The expansions of the Equation 3.37 with Taylor series and the elimination of second or higher terms yield below equation:

$$\check{R}^{n+1}(\breve{w}) = \check{R}^{n}(\breve{w}) + \left(\frac{\partial \check{R}}{\partial \breve{w}}\right)^{n} \Delta \breve{w}^{n} \tag{3.38}$$

Newton methods assume that at the next iteration level, flow variables exactly satisfy Euler equation, thus $\check{R}(n+1)$ equals zero. The general form of Newton's methods can be written as:

$$\left(\frac{\partial \check{R}}{\partial \breve{w}}\right)^{n} \Delta \breve{w}^{n} = -\check{R}^{n}(\breve{w}) \tag{3.39}$$

$\Delta \breve{w}$ is the increment between flow variable at *nth* and *(n+1)th* iteration levels. The flow variable values at next iteration level can be found by adding increment to the value itself. $\partial \check{R}/\partial \breve{w}$ is known as the Jacobian matrices which are evaluated by taking derivatives of residual vector with respect to flow vector. Newton method is based on the evaluation of Jacobian matrices to linearize the governing equation and solving the linearized equations implicitly. The complexity of the derivation and the construction of the Jacobian matrices is increased by nonequilibrium and real gas effects. Therefore, Newton GMRES method is used in this study to eliminate the efforts to derive Jacobian matrices. The matrix free solvers are more effective in solving stiff equations in terms of computational and storage requirements [44].

Newton GMRES method is an inexact implementation of which satisfies linearity of equation by using GMRES methods. GMRES is the abbreviation for generalized minimal residual method and it is also known as Krylov subspace method. Newton-GMRES method is an inexact Newton method where the value of local linear residual is reduced in each step [45]. The inexact Newton method should satisfy following condition:

$$\left\| \check{R}^n(\breve{w}) + \left(\frac{\partial \check{R}}{\partial \breve{w}}\right)^n \Delta \breve{w}^n \right\| = \mu \left\| \check{R}^n(\breve{w}) \right\| \tag{3.40}$$

μ is the forcing term and $\mu \in (0,1)$. If the forcing term is chosen as 0, the exact Newton method is obtained. Determining the forcing term has crucial importance on convergence characteristics of solver. To obtain faster convergence, μ can be chosen close to zero. However, small forcing terms resulted in small reduction of the norm; thus, solver tries to catch this small reduction hardly [46].

In the GMRES part, evaluation of the Jacobian matrix is not necessary; however, Jacobian matrix and vector multiplication is required. For the given non-linear system of equations, multiplication is obtained explicitly from the first order forward differencing as Equation 3.41.

$$\left(\frac{\partial \check{R}}{\partial \breve{w}}\right).v = \frac{\check{R}(\breve{w} + \epsilon v) - \check{R}(\breve{w})}{\epsilon} \tag{3.41}$$

The v is normalized vector updated in each iteration level to approach $\Delta \breve{w}$. ϵ is small positive number calculated generally in each iteration level by dividing square root of machine epsilon to norm of the vector v. With the manner of Equation 3.41, GMRES methods achieve matrix free calculation.

The GMRES method is basically Krylov subspace method trying to solve linear system. To simplify comprehensibility, chosen linear system can be written as in Equation 3.42. The following formulation are derived from Bai, Hu and Reichel study [47].

$$\mathrm{Ax} = \mathrm{B} \qquad (\mathrm{A} \in R^{nxn}\ , B \in R^{n}, \qquad x \in R^{n}) \tag{3.42}$$

In GMRES method, the initial approximate value, x_0 and residuals are defined as:

$$r_0 = b - Ax_0 \tag{3.43}$$

The method tries to find a *x* value at each iteration.

$$\begin{gathered} x_1 = x_0 + z_0 \in \ [x_0 + K_k(A, r_0)] \\ \|b - Ax_1\| = min\|b - A(x_0 + z)\| \\ K_k(A, r_0) = span\ \{r_0, Ar_0, A^2 r_0, \dots, A^{k-1} r_0\} \end{gathered} \tag{3.44}$$

$K_k(A, r_0)$ is the *kth* order Krylov subspace. After that, the Arnoldi process is applied with inputs k, x_0 and r_0 . The Arnoldi iteration is used to obtain the orthonormal bases for the Krylov subspace. As an output, Arnoldi iteration gives Hessenberg matrix The minimization process begins with computing orthonormal basis.

$$\begin{gathered} V_1 = \frac{r_0}{\|r_0\|} \\ V_k = [V_1, V_2, \dots, V_k] \\ V_{k+1} = [V_1, V_2, \dots, V_{k+1}] \end{gathered} \tag{3.45}$$

$V_k \in R^n$ and $V_{k+1} \in R^{n+1}$ are orthonormal vectors. Arnoldi process gives the upper Hessenberg matrix, then the following Equation 3.46 can be written as:

$$AV_k = V_{m+1} H \quad \text{where } H \in R^{(n+1)xn} \tag{3.46}$$

Substituting Equation 3.46 into Equation 3.44 yields the final formulation of the Arnoldi process.

$$min\|r_0 - Az\| = min\|\|r_0\| e_1 - Hy\| \tag{3.47}$$

where $e_1 = (1,0,0,\ldots,0)^T, e_1 \epsilon R^{n+1}$ and $z = Vy$. To get upper Hessenberg matrix, series of Givens rotations are applied to dense Hessenberg matrix at the end of iteration. The multiplication of the vector and Givens rotation matrix yields a rotation which results zero entries at j< i-3 indices. Final form of Hessenberg matrix can be written as

$$H = \begin{bmatrix} h_{11} & h_{12} & & \ldots & h_{1n} \\ h_{21} & h_{22} & & \ldots & h_{2n} \\ 0 & h_{32} & h_{33} & \ldots & h_{3n} \\ & 0 & h_{43} & \ldots & \\ & & 0 & \ddots & \vdots \\ \vdots & & & \ddots & h_{nn} \\ & & & 0 & h_{n+1,n} \end{bmatrix} \tag{3.48}$$

At the end of the Arnoldi iteration, the minimization of the norm value of residual vector becomes a least square problem. The least square method tries to find optimum *y* to minimize *z* with QR factorization. QR factorization is a decomposition of Hessenberg matrix into product of orthogonal matrix, *Q* and triangular matrix, *R*.

$$H = QR \tag{3.49}$$

QR factorization is used to solve least square methods in a computationally efficient way. The QR factorization can be applied to Equation 3.47.

$$\begin{aligned} Hy &= \|r_0\|e_1 \\ H^T Hy &= H^T \|r_0\|e_1 \\ R^T Q^T QRy &= R^T Q^T \|r_0\|e_1 \\ R^T Ry &= R^T Q^T \|r_0\|e_1 \\ Ry &= Q^T \|r_0\|e_1 \end{aligned} \tag{3.50}$$

At the end of the least square method, *y* is minimized and final *x* value is obtained.

$$x_n = x_0 + Hy \tag{3.51}$$

Preconditioners are not used in Newton GMRES implementation, in this study. Convergence of GMRES algorithm strictly depends on Jacobian characteristics of governing equations. To have computationally effective method, preconditioner can be used. The effective preconditioners have close approximation to preconditioned matrix; hence, storage and construction of preconditioner are not supposed to create big computational cost. There are various preconditioners and application methods in literature; however, preconditioner are not used in this study to prevent computational complexity.

3.6 Boundary Conditions

In this section, boundary conditions of this current study are described. To obtain proper solution for a flow field, boundary conditions must be defined according to the direction of the information propagation. Also ghost cells are used to obtain proper boundary conditions. One ghost cell layer is applied to outer part of the grid for the accurate implementation of the first order discretization. In this study, three boundary conditions are implemented: far field, wall and symmetry line boundaries.

For the far field boundary conditions, information from flow propagates to leave the computational domain. The values of ghost cells which are defined at outer boundary layer are defined as free stream values. The flow variables at outer boundary cells are obtained by flow solver.

For the wall boundary conditions, there should not be any mass and energy fluxes through the geometry; thus, flow tangency condition should be enforced. Therefore, normal velocities at the wall surface is assumed as zero and the tangential velocities are extrapolated from the interior cells. The flow variables:

species mass, total mass, total energy and vibrational energy values are extrapolated from the interior cells. At the wall, normal components are removed from the total values to obtain tangential values, as in Equation 3.52.

$$U_{normal} = U_{interior} . n$$
$$\left(\rho u^j\right)_{boundary} = \left(\rho u^j\right)_{interior} - 2\rho U_{normal} n^j \tag{3.52}$$

n is the unit normal vectors to the wall. U_{normal} is obtained by multiplying normal vector with the velocity from the interior cells. Also, due to grid topology, front and wake of the geometry requires additional considerations. There is a symmetry line passing through the stagnation point, thus from free stream to leading edge and from trailing edge to far field points, values on both sides should be equal to each other. Corresponding velocities at *z* direction should be pointing at opposite directions for cells on both sides of this line. Other flow variables have the same values at these cells which are laying on the left and right of this line.

The symmetric boundary conditions are used to have less computational requirements. The symmetric characteristic of flow field allows to calculate flow on half of the computational domain. At the each side of the symmetry plane, all flow variables are equal to each other except velocity. Tangential velocity components are also equal; however, normal component of velocities should be in reverse direction with the same magnitude.

CHAPTER 4

RESULTS AND DISCUSSIONS

Three dimensional Apollo Command Module is chosen as a test case due to sufficient number of the experiment and flight data. The sketch of module is given in Figure 4.1.

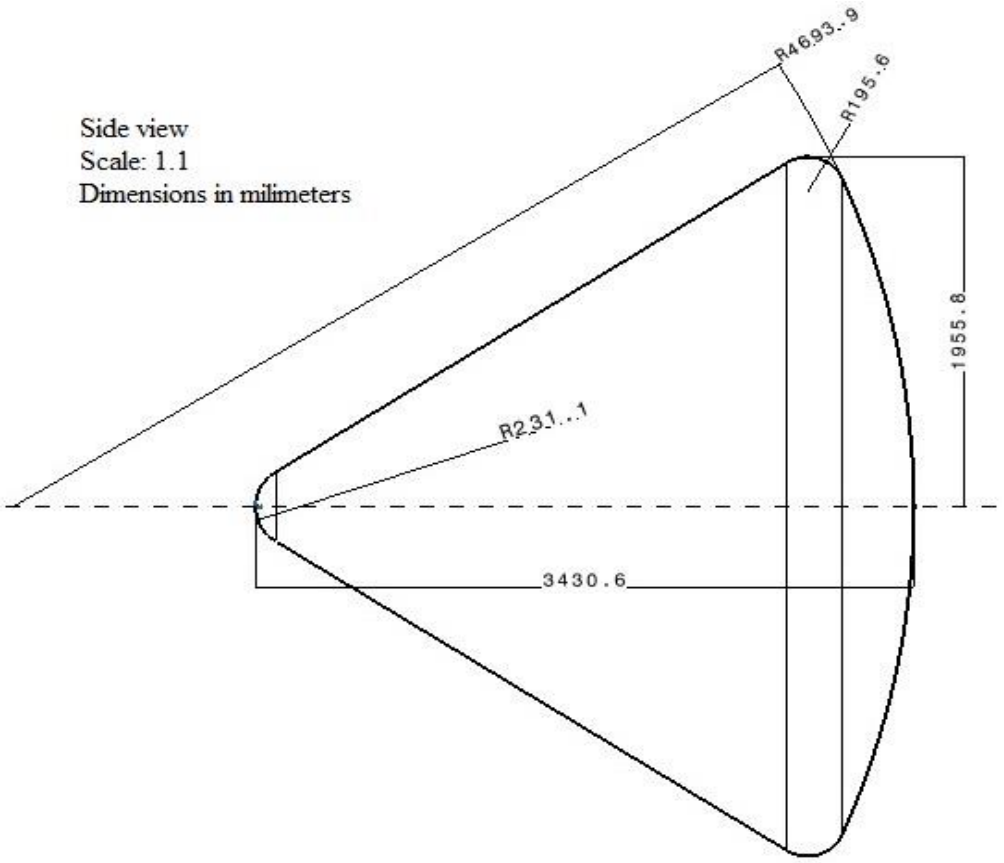

Figure 4.1. Geometrical details of Apollo Command Module

Free stream conditions are given in the following table, Table 4.1. Different free stream conditions are applied in various cases; however, free stream temperature and pressure (at approximately 40 km altitude) remain the same in all computations.

Table 4.1 Free stream values

Parameter	Value
Temperature (K)	220
Pressure (Pa)	664
Mach	15
Species (Case I)	2 (N_2, N)
Species (Case II)	5 (O_2,N_2,N,O,NO)
Species (Case III)	11(O_2,N_2,N,O,NO, O^+_2,N_2^+,N^+,O^+,NO^+,e)

Three different number of species are examined; also, the effects of number of the reactions on flow characteristics are studied. In order to see effects of temperature on the reactions characteristics, different values of free stream Mach numbers are used.

4.1 CFD Considerations

A grid independency study has been performed in this study. The number of cells in the domains can be seen in Table 4.2. Moreover, oriented views of medium computational domain is given as in Figure 4.2. Although the first figure looks like two dimensional, it is the perspective view of three dimension figure. The obtained

figure is three dimensional. The representation of whole computational domain with coarse mesh can be seen in Figure 4.3.

Table 4.2. List of meshes with different cell numbers

Mesh	i x j x k	Number of cells
Coarse	32x16x9	4608
Medium	64x32x17	34816
Fine	128x64x35	286720

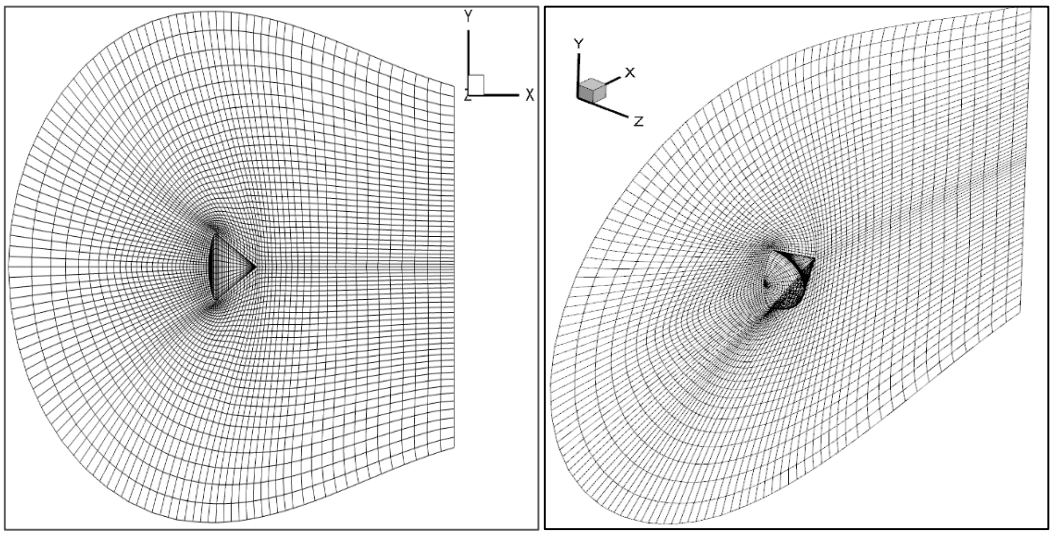

Figure 4.2 Orientation views of 3D computational domain on different planes

Table 4.3 Effects of mesh refinement study on computation time and stagnation condition

Mesh	CPU Time	Maximum Pressure	Maximum Temperature
Coarse	23 minutes	156.7 kPa	4752 K
Medium	5 days 13 hours	147.8 kPa	4740 K
Fine	3 days 2 hours (250 iterations)	X	X

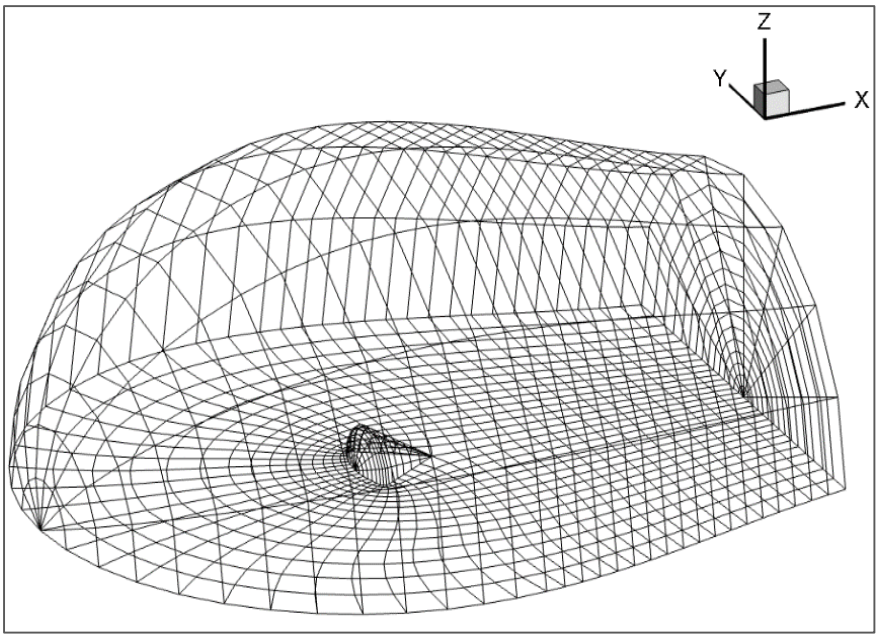

Figure 4.3. 3D representation of coarse mesh

The maximum pressure and temperature values are used to measure the effects of mesh refinement. To reach convergence criteria ($||R||/||R0|| < 10^{-12}$), coarse grid requires 23 minutes whereas medium grid requires 5 days 13 hours. The fine mesh solution completes 100 iterations in 3 days and 2 hours as given in Table 4.3. However, the fine mesh solution could not achieve high iteration number due to oscillations. Therefore, due to enormous CPU time and convergence characteristics

of the fine mesh, the fine mesh was not used in this study. Results are obtained by using the medium and coarse mesh size.

The maximum pressure and temperature values with different computational domain are given in Table 4.3. The difference in between the peak pressure values of the coarse and medium meshes is almost 9 kPa. The change is approximately % 6. Also, difference in between temperature values is 12 K. Therefore, the medium mesh is a good choice to simulate flow field in this study. The most of the results are obtained by using the medium mesh.

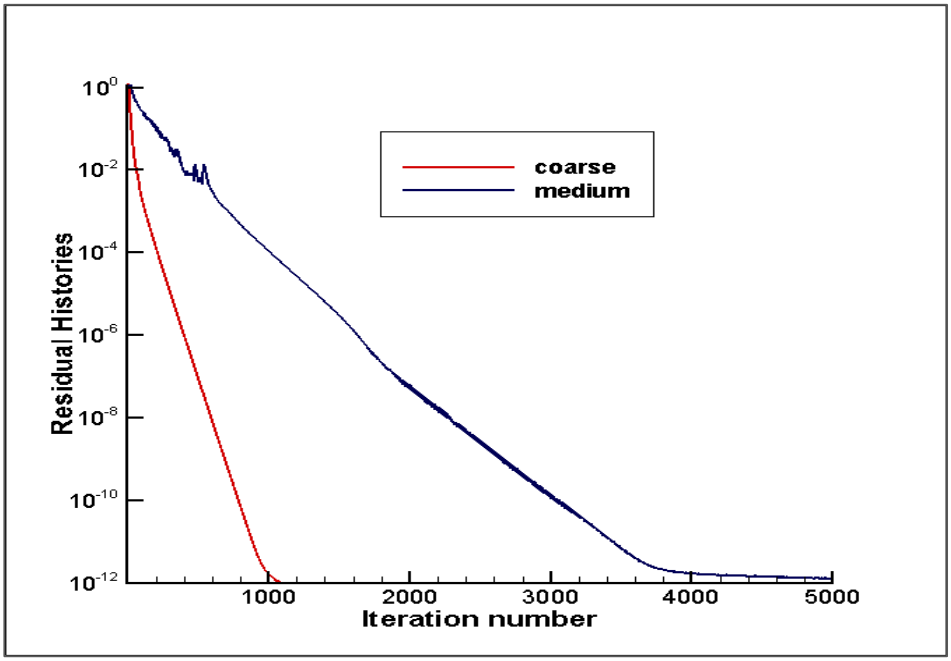

Figure 4.4. Comparisons of convergence characteristics on coarse and medium grid

The convergence characteristics of the coarse and medium computational meshes can be seen in Figure 4.4. The residual histories of the fine mesh are not included in this figure because of stability and CPU time problems. As in the Figure 4.4, the coarse grid reaches predefined convergence criteria (10^{-12}) in 1000 iterations; whereas, medium mesh requires 5 times larger iteration steps.

The first order and second order spatial discretizations are examined. In this study, the second order discretization could not work properly with the real gas assumptions and in hypersonic speed ranges. However, the second order discretization is achieved with ideal gas assumption for hypersonic speed range in our study. The residual histories with respect to iteration number of different discretization order are shown in Figure 4.5. Although different flux limiters are examined, oscillations still continue, and residual values stay high. Therefore, the first order spatial discretization are commonly used in this study to achieve stability of solver.

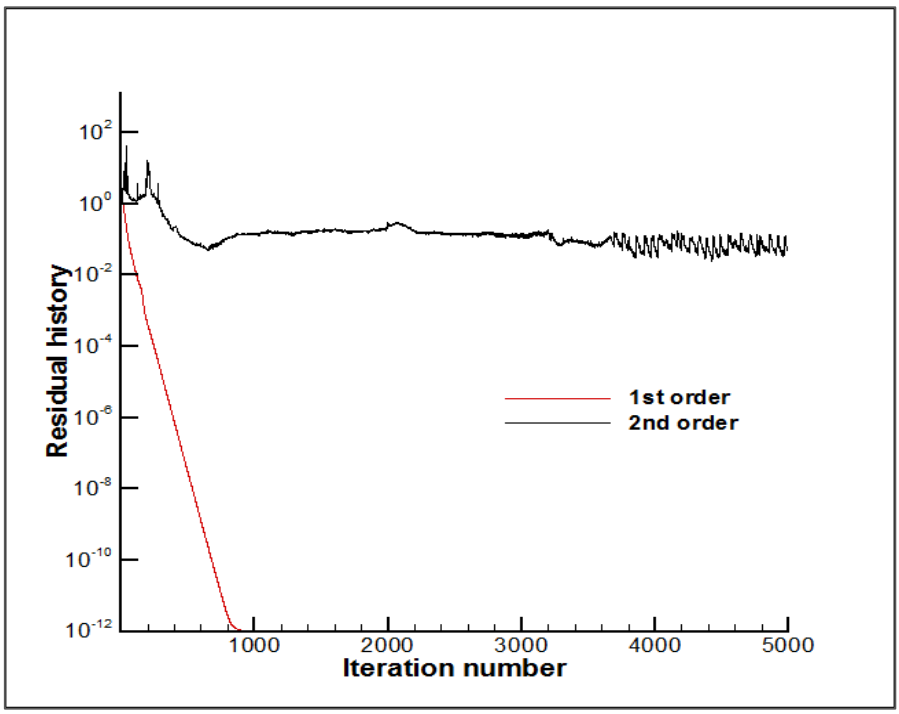

Figure 4.5. Comparisons of convergence characteristics of first and second order spatial discretizations (M=10, α=20)

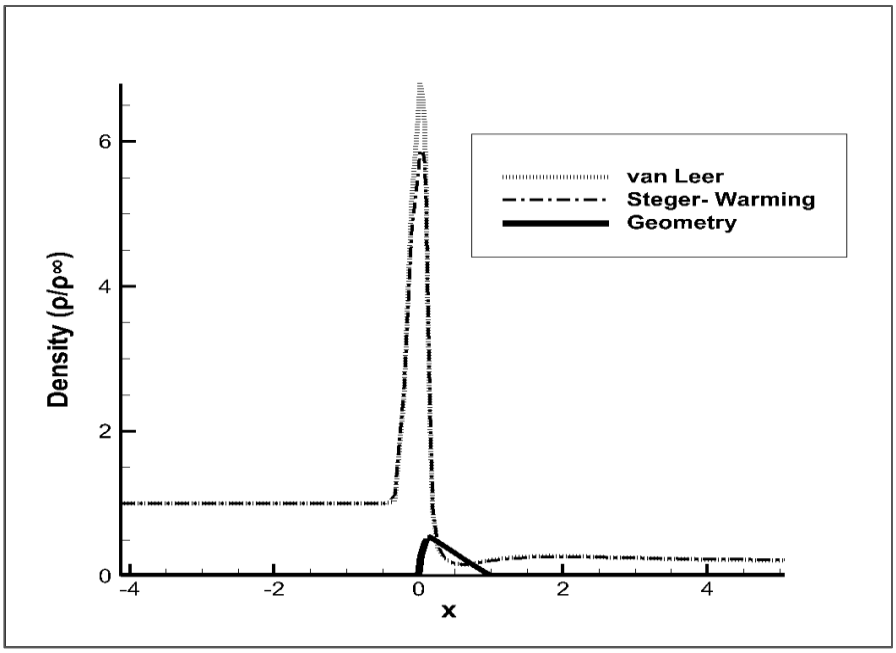

Figure 4.6 Comparisons of flux vector splitting methods with 5 species models (M=15, α=0)

Moreover, two different flux vector splitting are considered in this study: Steger-Warming and Van Leer flux splitting. For these splittings, the non-dimensional density and Mach contours are shown respectively in Figure 4.6 and 4.7. There are small differences at stagnation point and the wake region. Also, both splitting methods work properly with real gas assumption, chemical and vibrational nonequilibrium models.

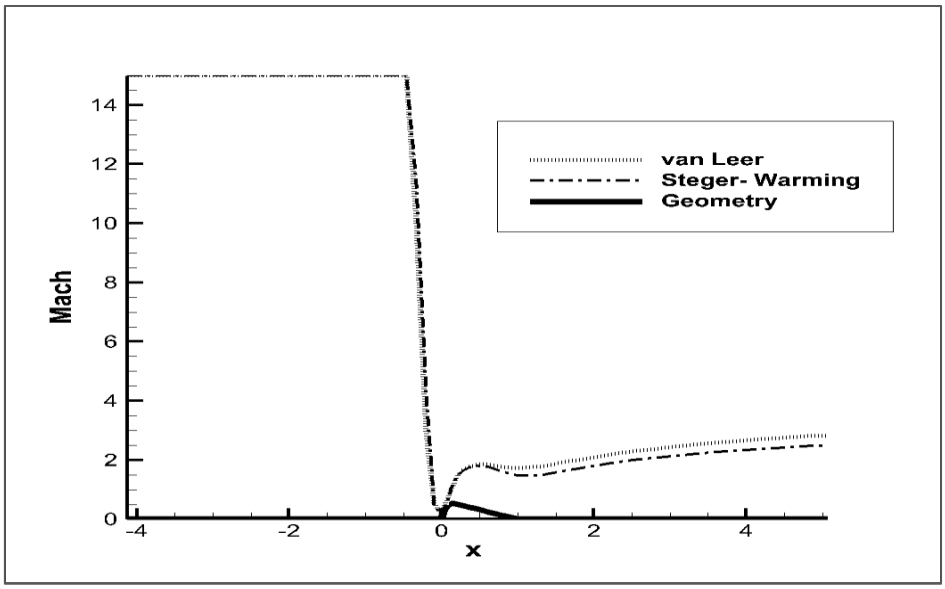

Figure 4.7 Comparisons of flux vector splitting methods with 5 species models (M=15, α=0)

Table 4.4 Number of flow variables with respect to different tests.

Chosen solver	Number of flow variables
Ideal gas	5 : ρ, ρu, ρv, ρw, ρE
Real gas, 2 species	6 : ρ, ρu, ρv, ρw, ρE, ρ1
Real gas , 5 species	9 : ρ, ρu, ρv, ρw, ρE, ρ1, ρ2, ρ3, ρ4
Real gas, 11 species	15: ρ, ρu, ρv, ρw, ρE, ρ1, ρ2, ρ3, ρ4….. ρ10
Real gas, 2 species, (two temperature)	7 : ρ, ρu, ρv, ρw, ρE, ρ1, ρEv

In this study, ideal and real gas assumptions are examined; also, real gas assumption is studied with different species number and different temperature models. The number of flow variable for each assumptions can be seen through Table 4.4.

Three dimensional representation of flow field simulation can be seen through Figure 4.8, 4.9 and 4.10. In Figure 4.8, nondimensional total density contours around the whole geometry are presented, and velocity vectors are also superimposed. At the last figure, nondimensional entropy distributions are shown at half of the computational domain. These two results are also obtained with 5 species model for Mach 15.

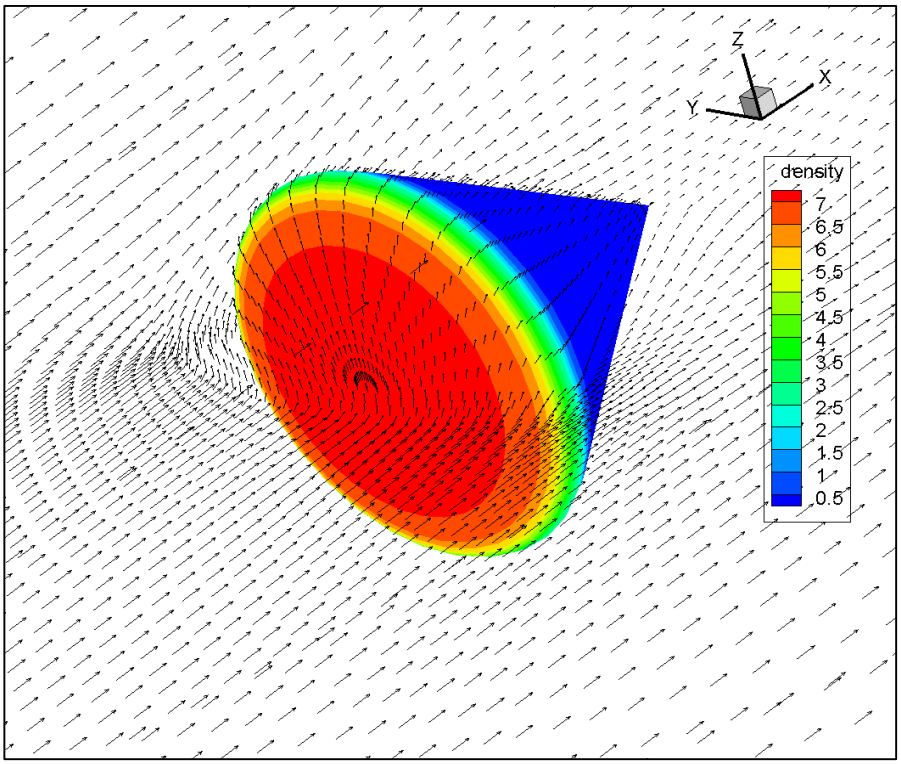

Figure 4.8. Nondimensional density contours around the whole ACM (M=15, α=0)

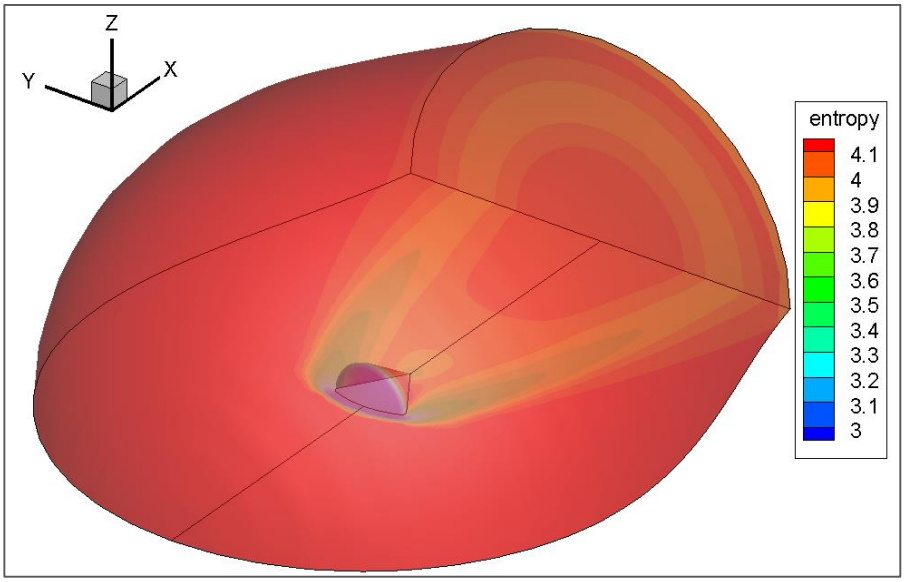

Figure 4.9 Nondimensional entropy distributions at half of the computational domain (M=15, α=0)

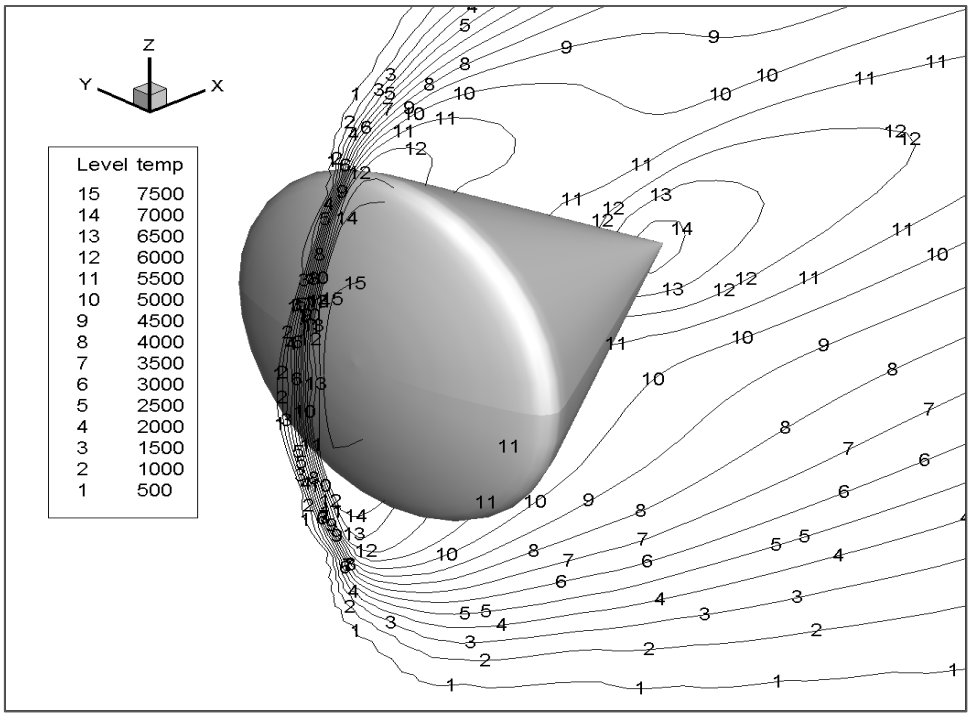

Figure 4.10 Temperature [K] contours at whole computational domain (M=15, α=0)

4.2 Validation of Code Solver

Computations are done for Apollo Command Module to validate the flow solver. Surface pressure around the module are compared with the wind tunnel tests results. The various results for the normalized pressure through stagnation line are given in Murray study [49]. These results are obtained from Bertin's [49] and Marvin's [51] wind tunnel experiments with helium gas.

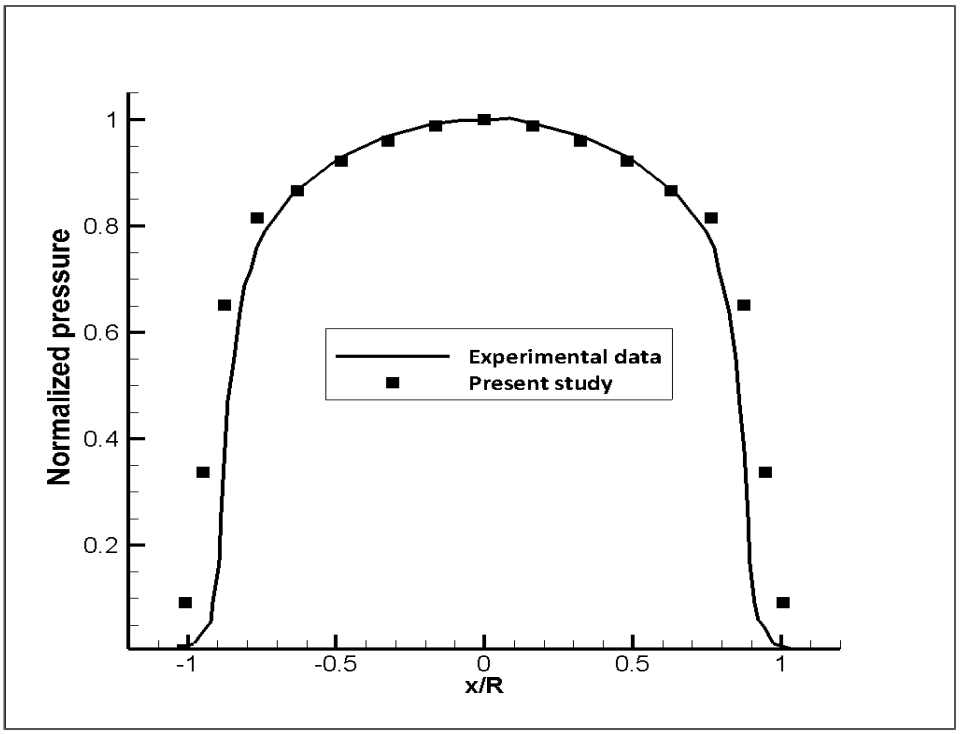

Figure 4.11 Comparisons of normalized surface pressure obtained by second order discritization with experimental data [49].

The pressure values obtained by using higher order discritization and flux limiters are compared with experimental data as in Figure 4.11. For this case, Mach number is 9, and angle of attack is zero. These results are obtained with the ideal gas assumption. The converce characteristics of the second order discretization is poor; therefore, there are big differences on the side surfaces.

In Figure 4.12, the pressure distributions for different angle of attack values in Helium gas is represented at Mach 20 [51]. For this validation, Helium gas is used with real gas assumption, and chemical reactions are ignored. Figure 4.12 shows a good the consistency of pressure distributions between the experimental data and from current solver. The normalized pressure distributions at two different angle of attacks (α=0 and α=25) are compared in Figure 4.12 Moreover, the real gas assumption work properly to simulate pressure distributions at high Mach values.

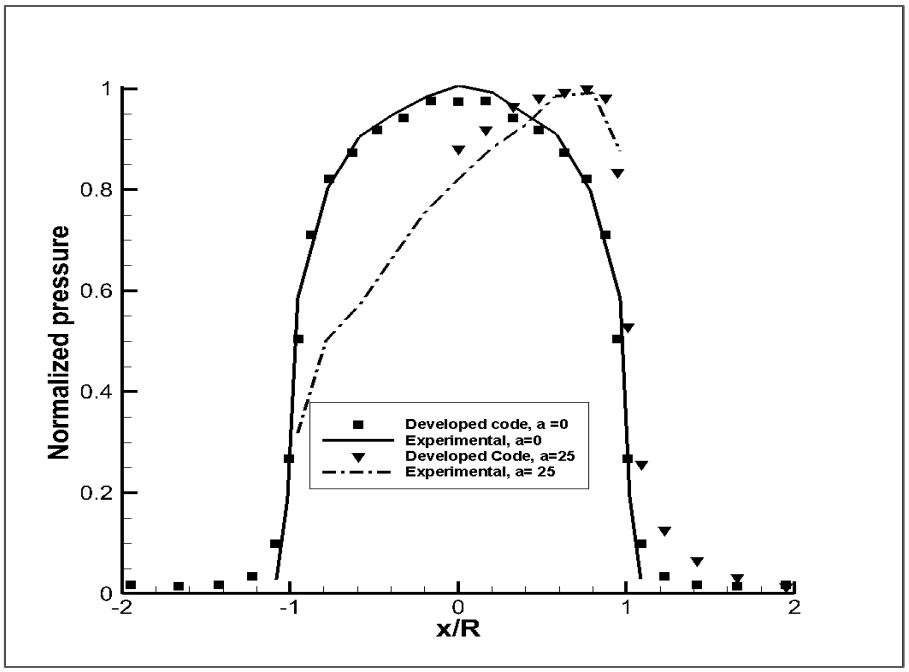

Figure 4.12 Comparisons of normalized pressure with experimental data (M=20)

In Figure 4.13, pressure distributions with different approaches are compared with the experimental data. Experiments were done at Mach 10.18 with zero angle of attack. The results are obtained by solving governing equation by considering real gas assumption with different species number. The pressure distribution with two temperature model is also compared. It should be noted that the real gas assumption is efficient in the simulation of the flow field where ideal gas assumption holds.

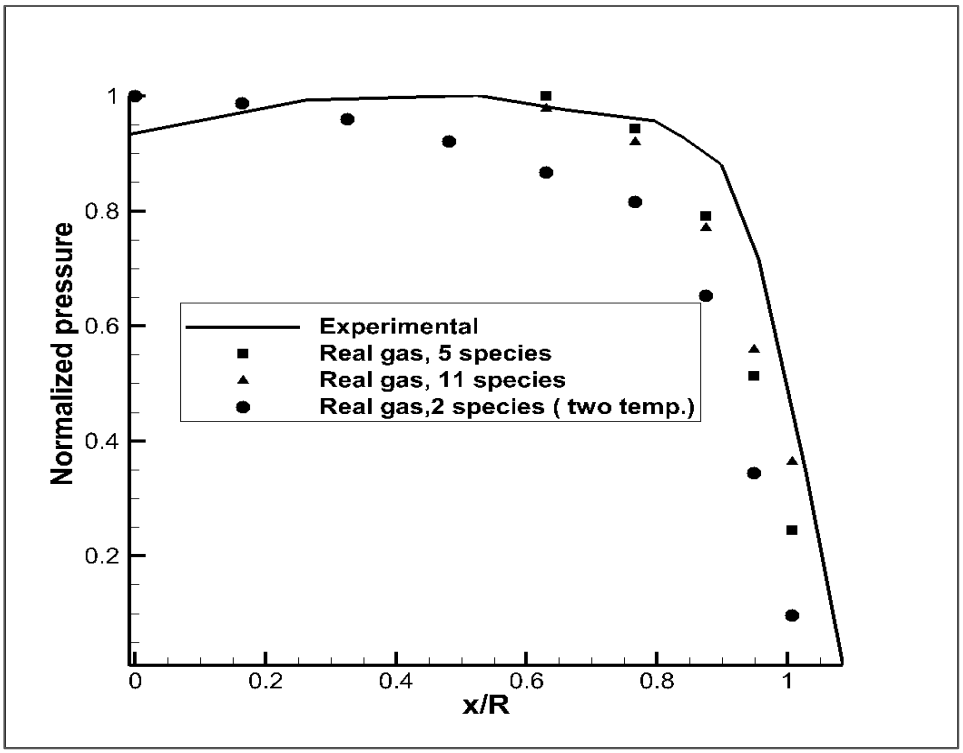

Figure 4.13 Comparisons of normalized pressure distribution by experimentally and different computational models

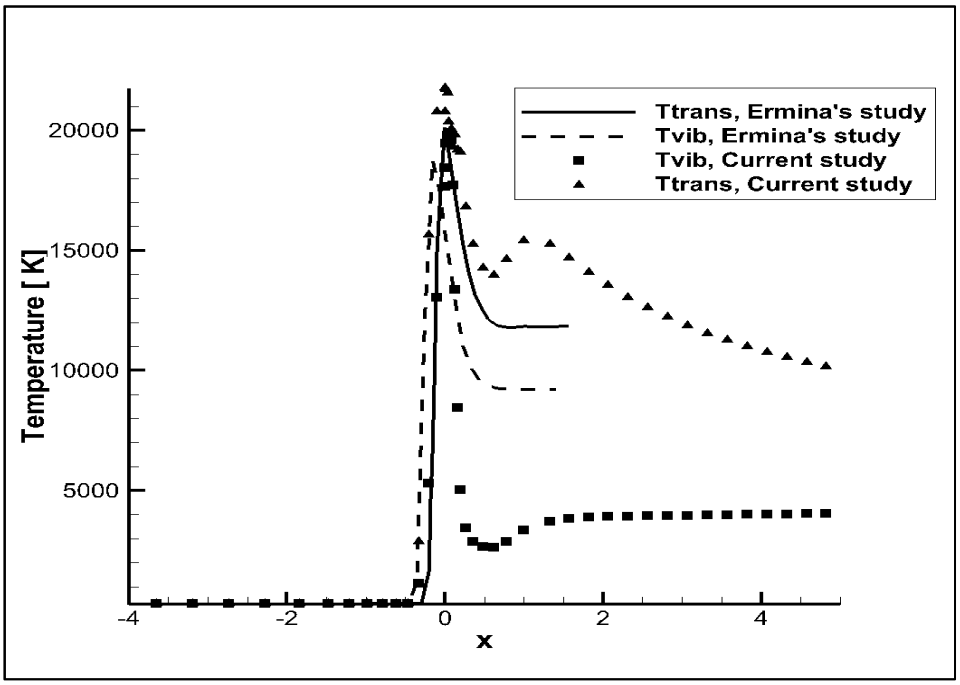

Figure 4.14 Comparisons of translational and vibrational temperature and Ermina's computational results (right) [52] at stagnation line

There are not any available experimental and flight data for translational and vibrational temperature distributions around the ACM. Therefore, these temperature values are compared with Ermina's study [52] as in Figure 4.14. It can be seen that results are similar with Ermina's results, and the peak values of both study are close to each other. These temperature distributions are obtained for Mach 32.4.

At this section, validity of the developed code solver is examined, and it can be seen obviously that the agreement between experimental and literature data is good. In the next section, flow field calculations are obtained with different models.

4.3 Ideal Gas and Real Gas Results

It was mentioned that the applicability of ideal gas assumptions is restricted with temperature. In the hypersonic speed range, the real gas assumption is more suitable compared to ideal gas assumption. There are important change in flow characteristics according to chosen models. First of all, the obtained shock stand of distance with real gas assumption is shorter than that of ideal gas assumption. In Figure 4.15, it can be seen that ideal and real gas assumptions affect the shock stand of distance. Moreover, real gas simulation gives smaller shock stand off distance than the ideal gas simulation.

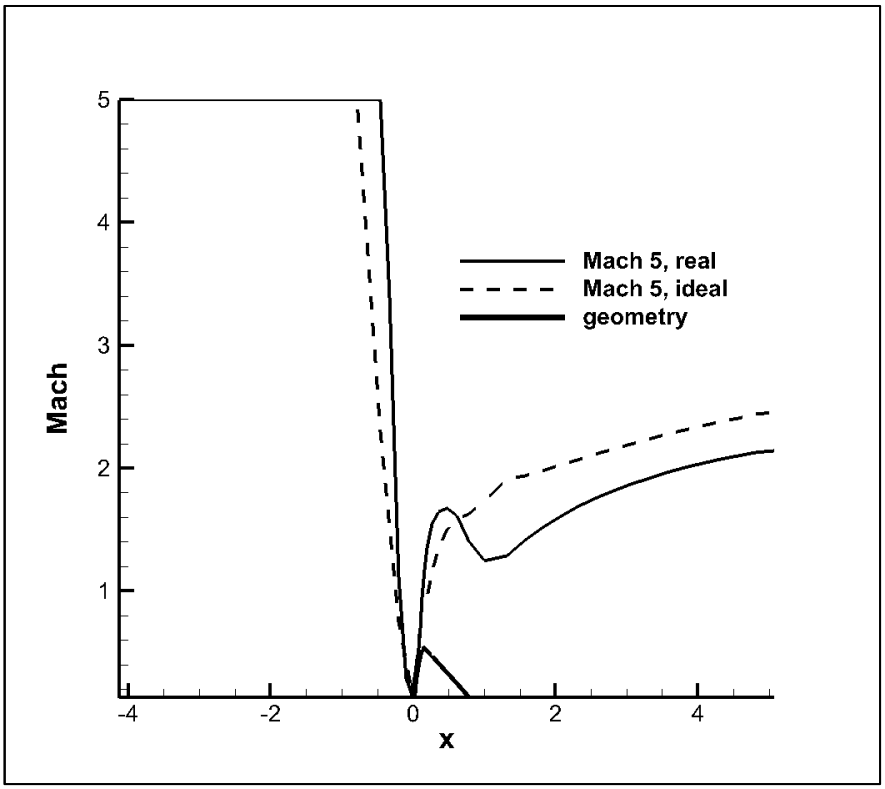

Figure 4.15 Mach distributions along the stagnation line with ideal gas and real gas assumptions (M=5, α=0)

The total density contours for various Mach numbers with ideal and real gas solver can be seen through Figure 4.16. Angle of attack is zero in this figure. There are big differences at the stagnation point for ideal and real gas assumptions. For the same Mach value (M=20), the peak total density is close to 7.5 for real gas assumption and it is approximately 4.2 for ideal gas assumption.

In Figure 4.17, non-dimensional temperature values are compared where angle of attack is zero. The importance of real gas assumption arises with increasing temperatures. For low Mach values, ideal and real gas assumptions have almost same distributions around the geometry. However, there are big differences at temperature values around geometry for high Mach values. Therefore, it can be seen that real gas assumption is required for high temperature flow to achieve high accuracy.

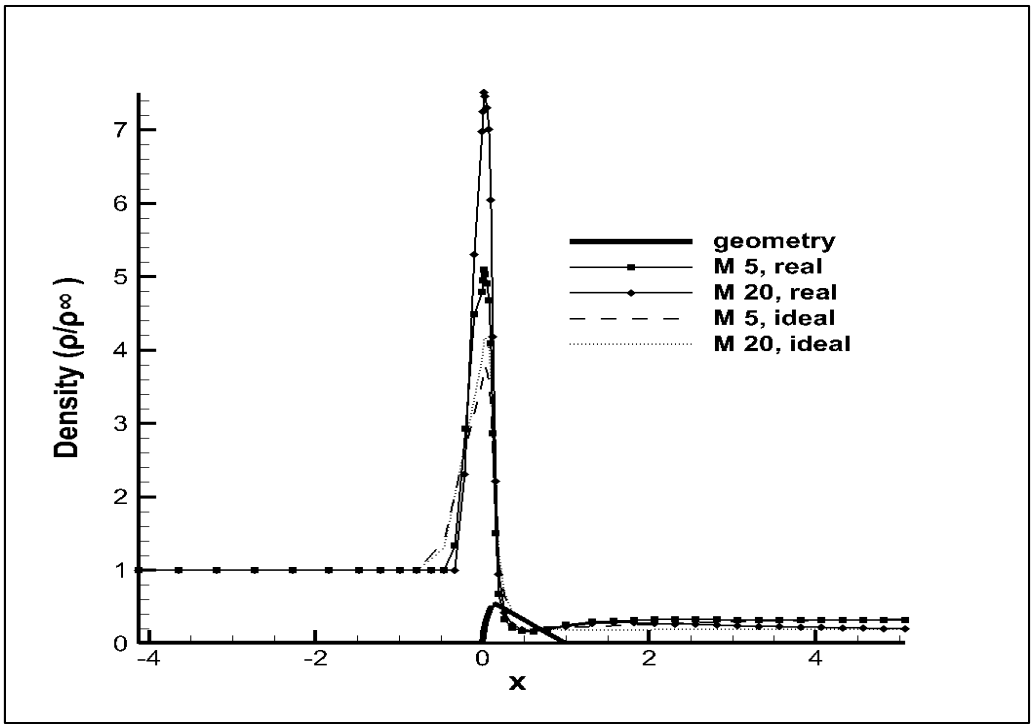

Figure 4.16 Density contours with ideal and real gas assumptions (α=0)

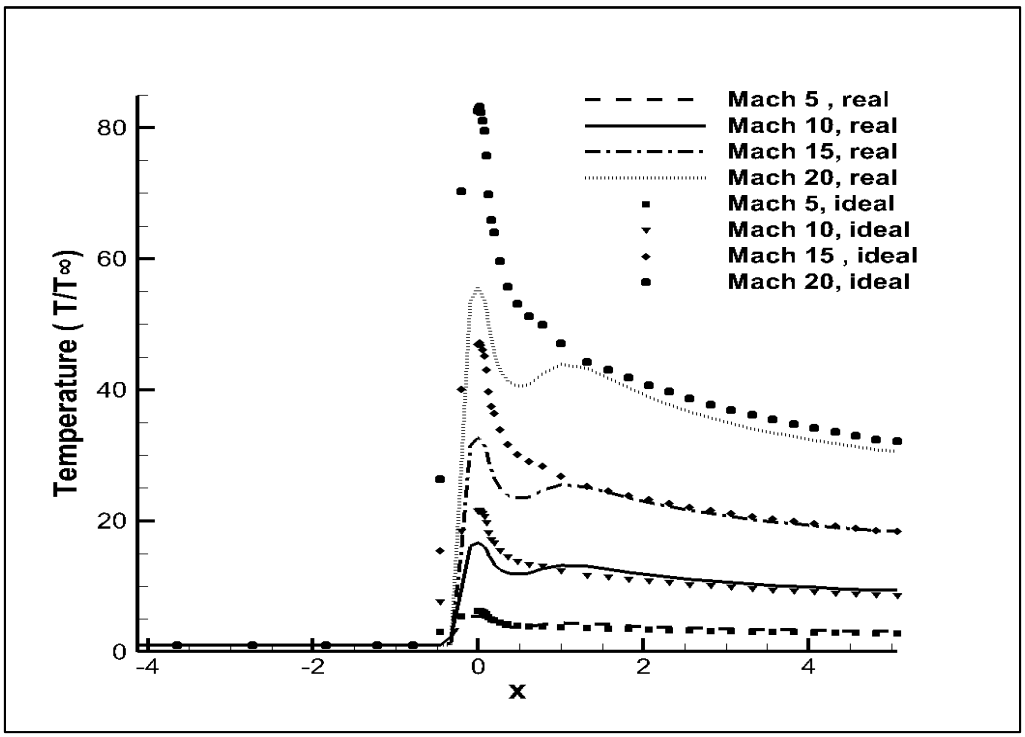

Figure 4.17 Temperature distributions with ideal and real gas assumptions (α=0)

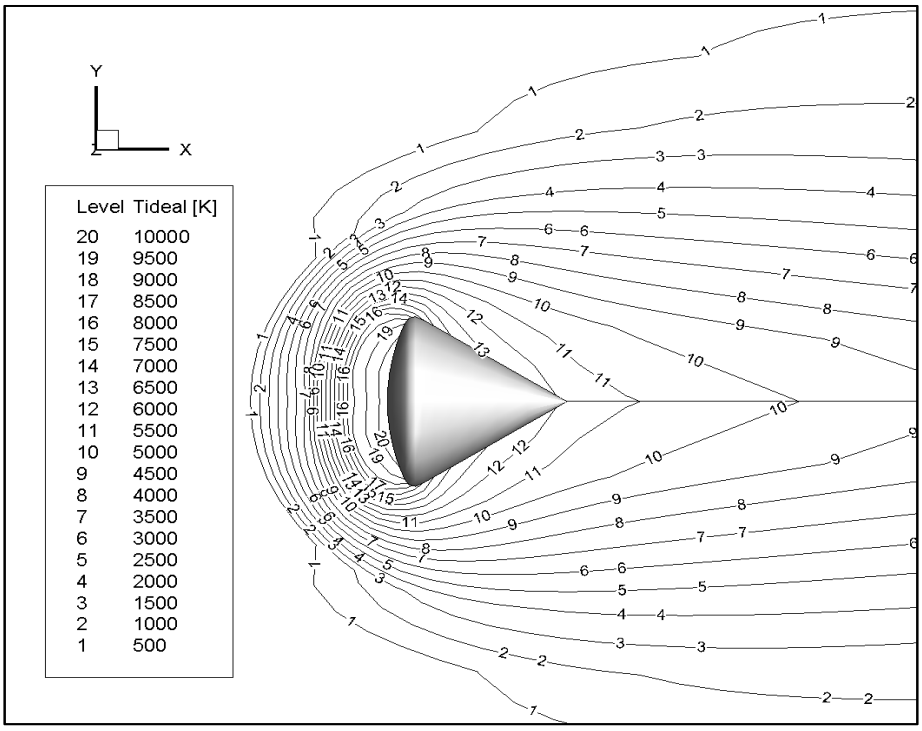

Figure 4.18 Temperature contours with ideal gas assumption (M=15, α=0)

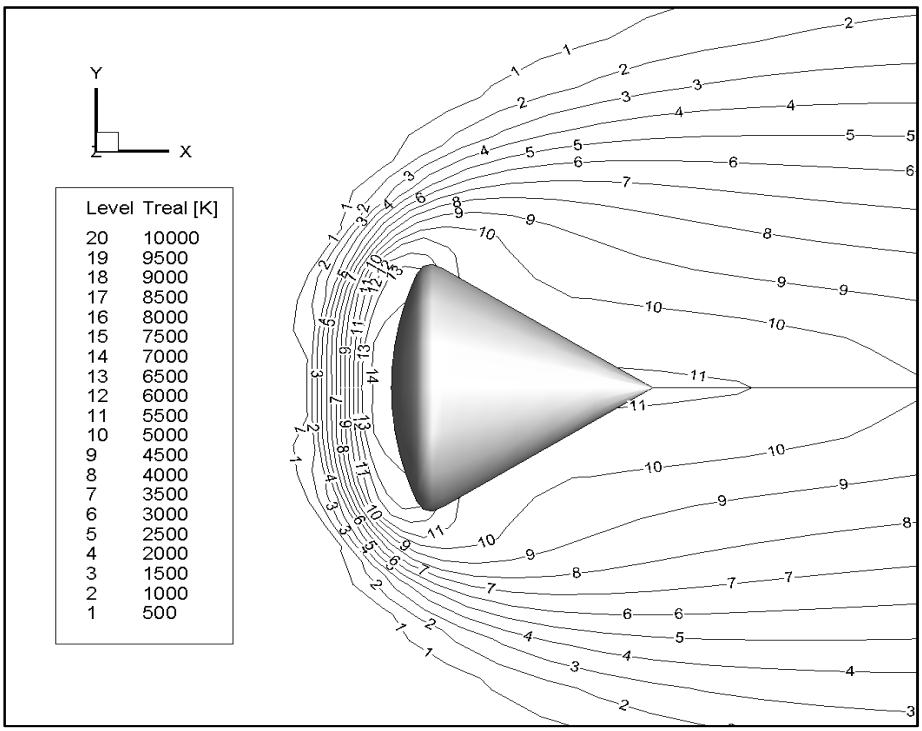

Figure 4.19 Temperature contours with real gas assumption (M=15, α=0)

Temperature contours with ideal and real gas assumptions are given in Figure 4.18 and Figure 4.19. Also, density contours are compared in Figure 4.20.

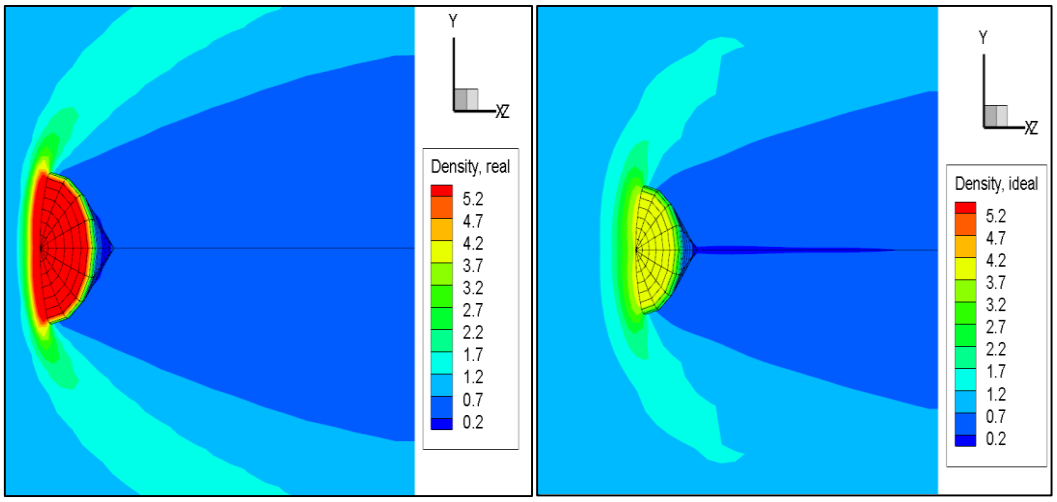

Figure 4.20 Density contours with ideal and real gas assumptions (M=15, α=0)

Lastly, assumptions change the performance of the solver. To reach the same residual value (10^{-6}), each assumptions has different CPU time requirement as given in Table 4.5. Computation time is getting larger with the detailed modelling as expected.

Table 4.5 CPU time requirement for different assumptions with different species number

Model	CPU time requirement
Ideal Gas without reactions	7 min 14 sec
Real gas with 2 species	34 min 43 sec
Real gas with 5 species	7 hours 48 min
Real gas with 11 species	1 day 3 hours

To sum up, ideal gas assumption results in bigger shock standoff distance and temperature distributions around the geometry than real gas assumption. In the modelling of hypersonic flow field, real gas assumptions are commonly preferred to obtain correct physical modelling.

4.4 Results for Chemical Nonequilibrium Models

At this part, the effects of chemical nonequilibrium models on flow field characteristics are examined. The influences of forward and backward reaction calculations are investigated separately.

4.4.1 Effects of Forward Reaction Rate Calculations

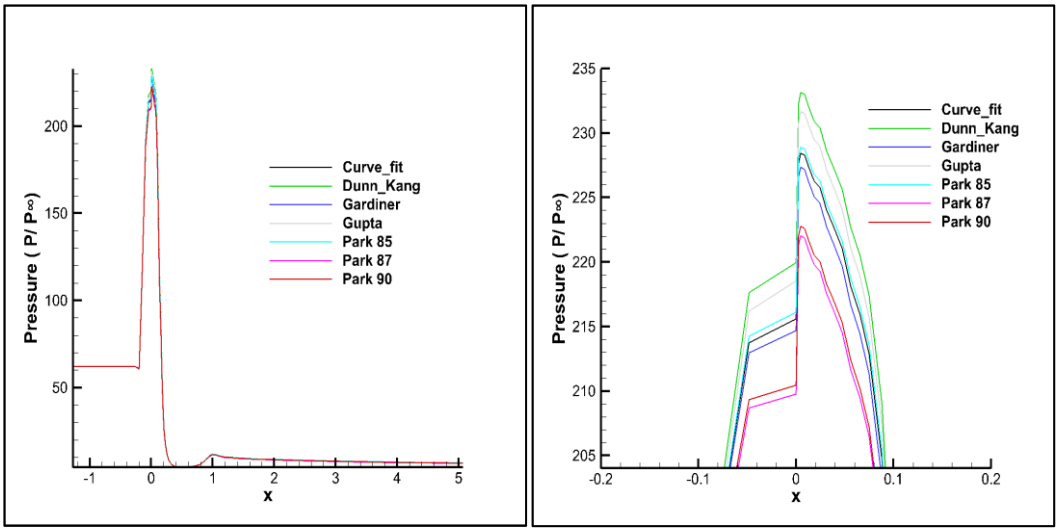

Figure 4.21. Pressure distributions around the geometry with different forward reaction rate constants (M=15, α=0)

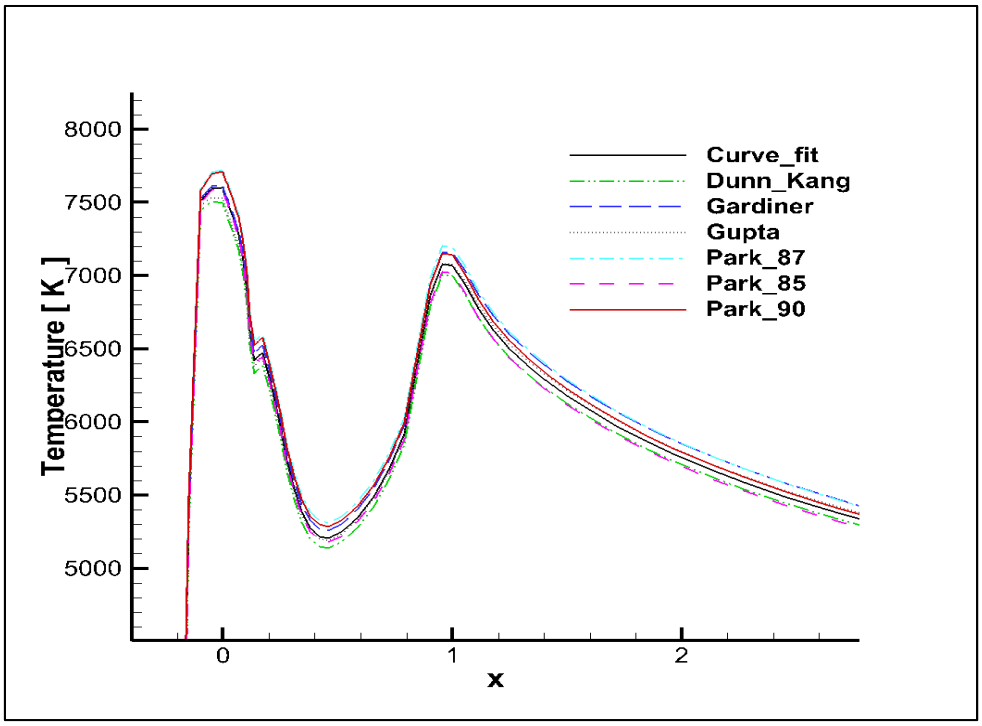

Figure 4.22 Temperature distribution with different forward reaction rate constants at stagnation line (M=15, α=0)

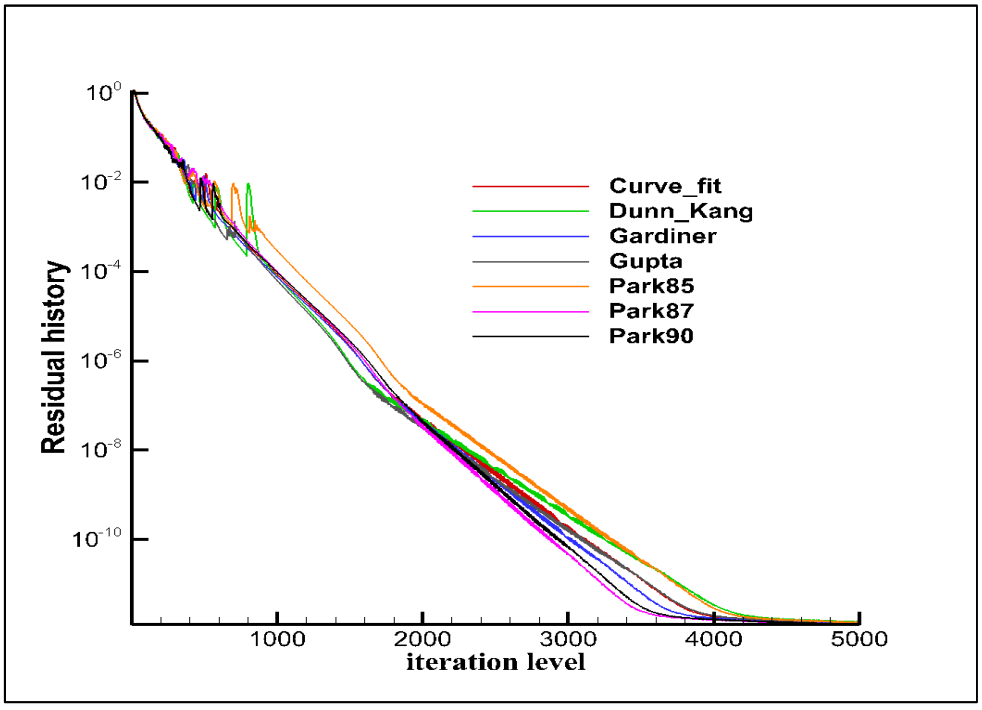

Figure 4.23 Residual histories for different forward reaction rate constants (M=15, α=0)

In the Figure 4.21, non-dimensional pressure distribution is represented with different forward reaction rates. The figure on the right is given to analyze the effects of coefficients on the stagnation point. Also, in Figure 4.22, temperature distributions along stagnation line are shown. The differences can be distinguished easily around the geometry. The influence of different coefficients on convergence characteristics can be seen in Figure 4.23. Dunn- Kang and Park 85 coefficients cause more oscillations in convergence.

In Figures 4.24 and 4.25, different coefficients to calculate forward reaction rate are compared by using species mass fractions. As in the figures, different mass fractions are obtained for different coefficients. There are big differences for species mass fractions, and there are not any certain way to choose the most accurate forward rate constants. These increase the uncertainty of modeling in chemical nonequilibrium. In this study, compatibility and stability effects of these coefficients are examined. Due to the numerical stiffness of modeling physical phenomena during atmospheric re-entries, all models cannot provide converged solutions. Therefore, Gardiner's and Park's coefficients are mainly used in this study.

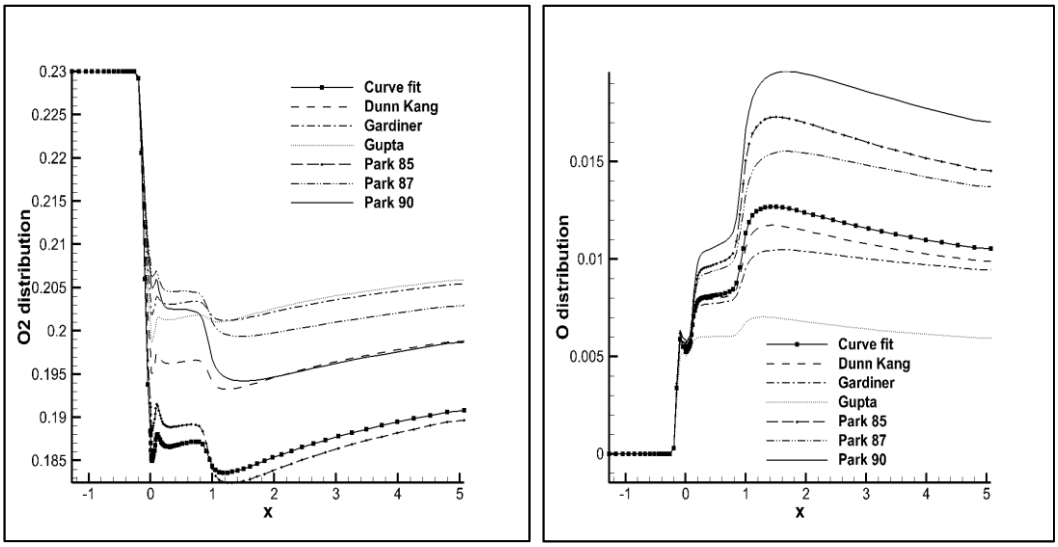

Figure 4.24. O_2 and O mass fractions along stagnation line with different forward reaction rate coefficients (M=15, α=0)

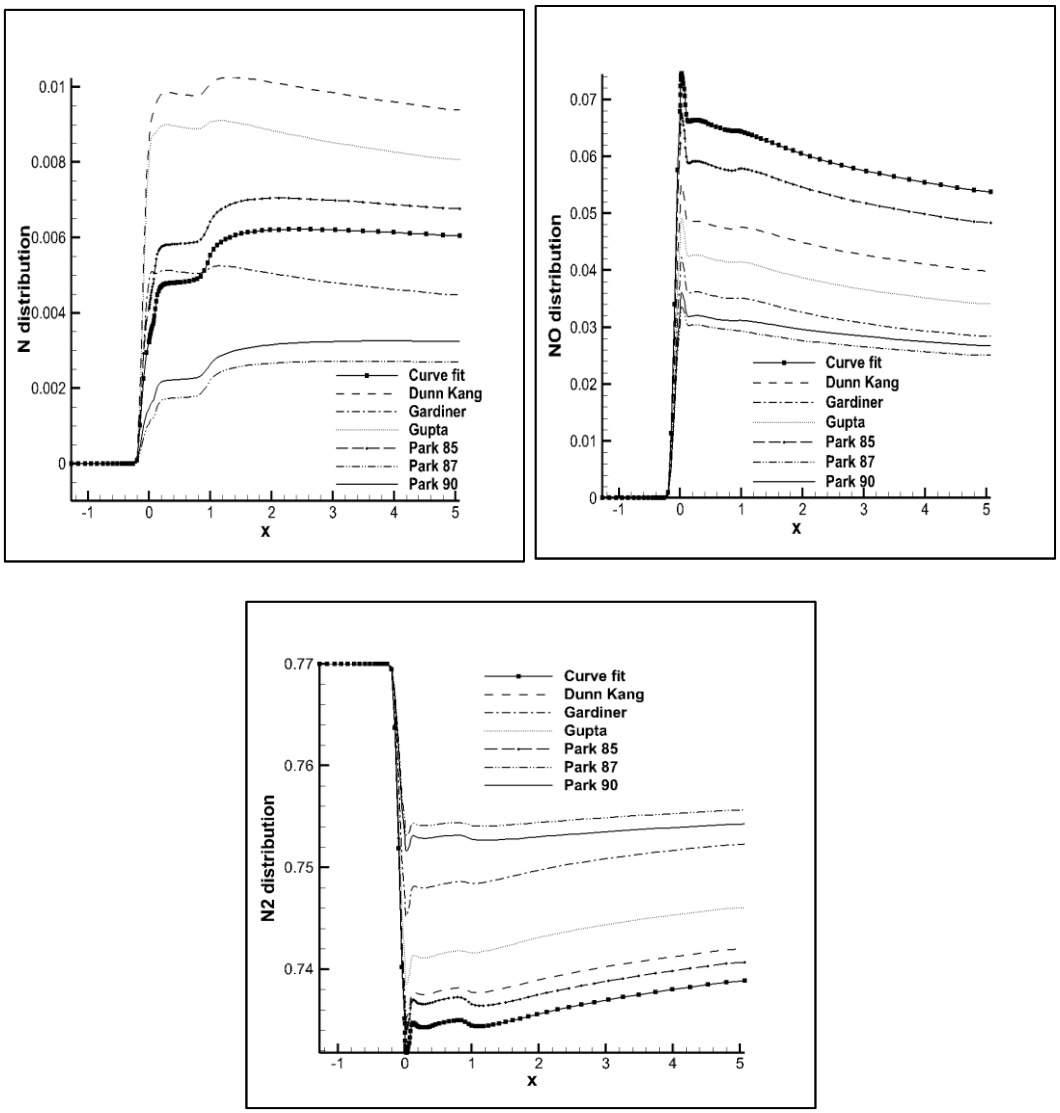

Figure 4.25 N_2, N and NO mass fractions around the geometry with different forward reaction rate coefficients (M=15, α=0)

The contours of species mass fractions around geometry with Gardiner's coefficients can be seen in the following figure, Figure 4.26. It can be seen that dissociation reactions occur actively behind the geometry because of the temperature.

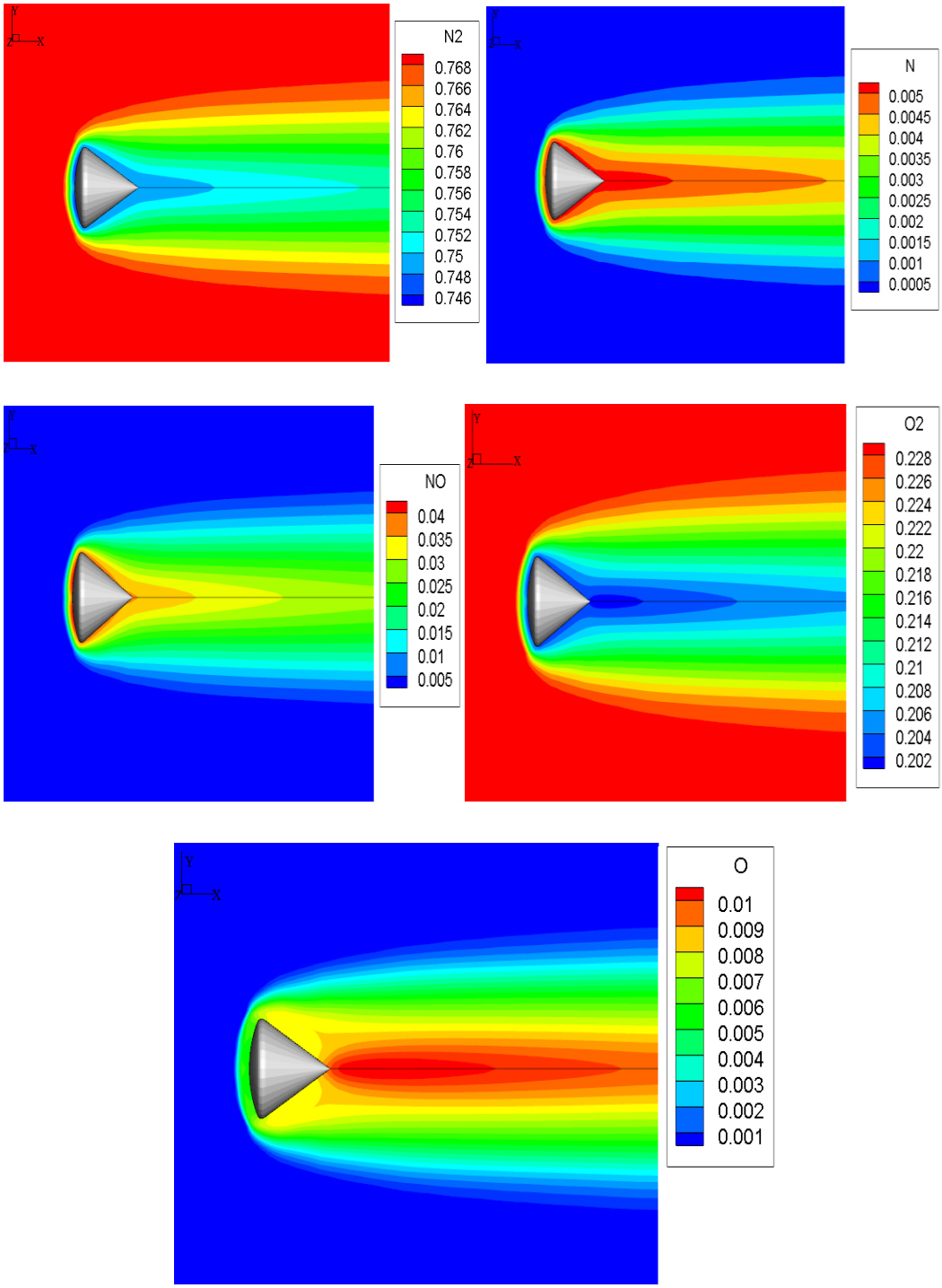

Figure 4.26 Species mass fractions around the geometry with Gardiner's forward reaction rate constants for 5 species (Mach = 15)

4.4.2 Effects of Backward Reaction Rate Calculations

There are two different backward reaction rate calculation methods based on calculation of equilibrium constants: Gibb's free energy minimization and Park's curve fitted fifth order polynomials. In Figure 4.27, it can be seen that backward reaction rate calculation has an important effect on the distributions of species. Also, there are not any available experimental or theoretical data to choose appropriate modelling. However, Gibb's free energy minimization method is preferred in this study due to stability and applicability concerns.

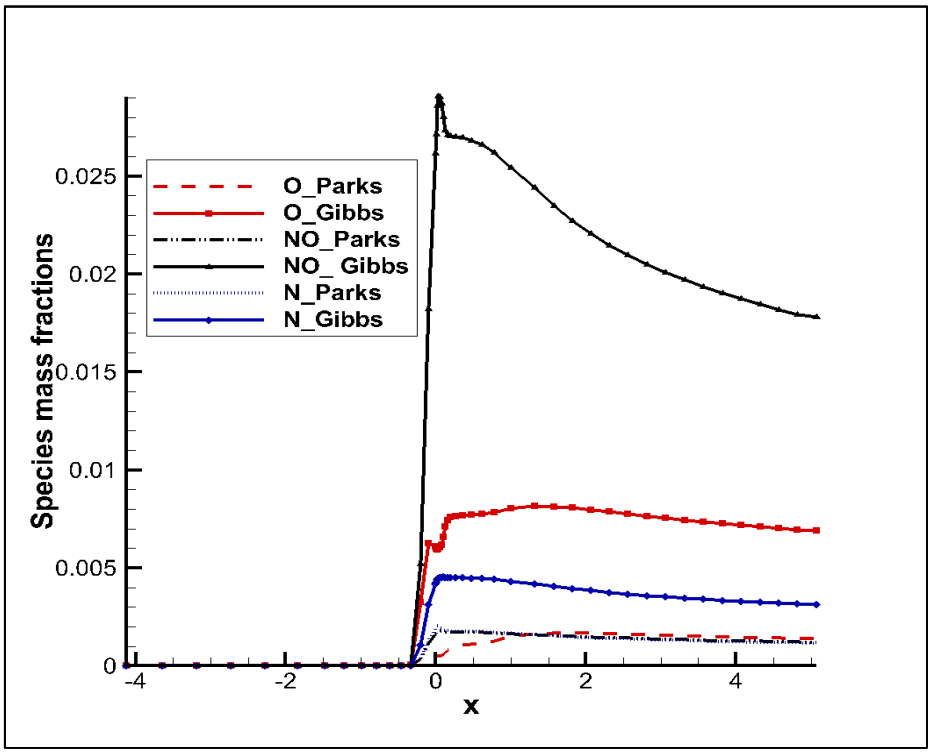

Figure 4.27 Species mass fractions around the geometry with different backward reaction rate calculation methods (M=15, α=0)

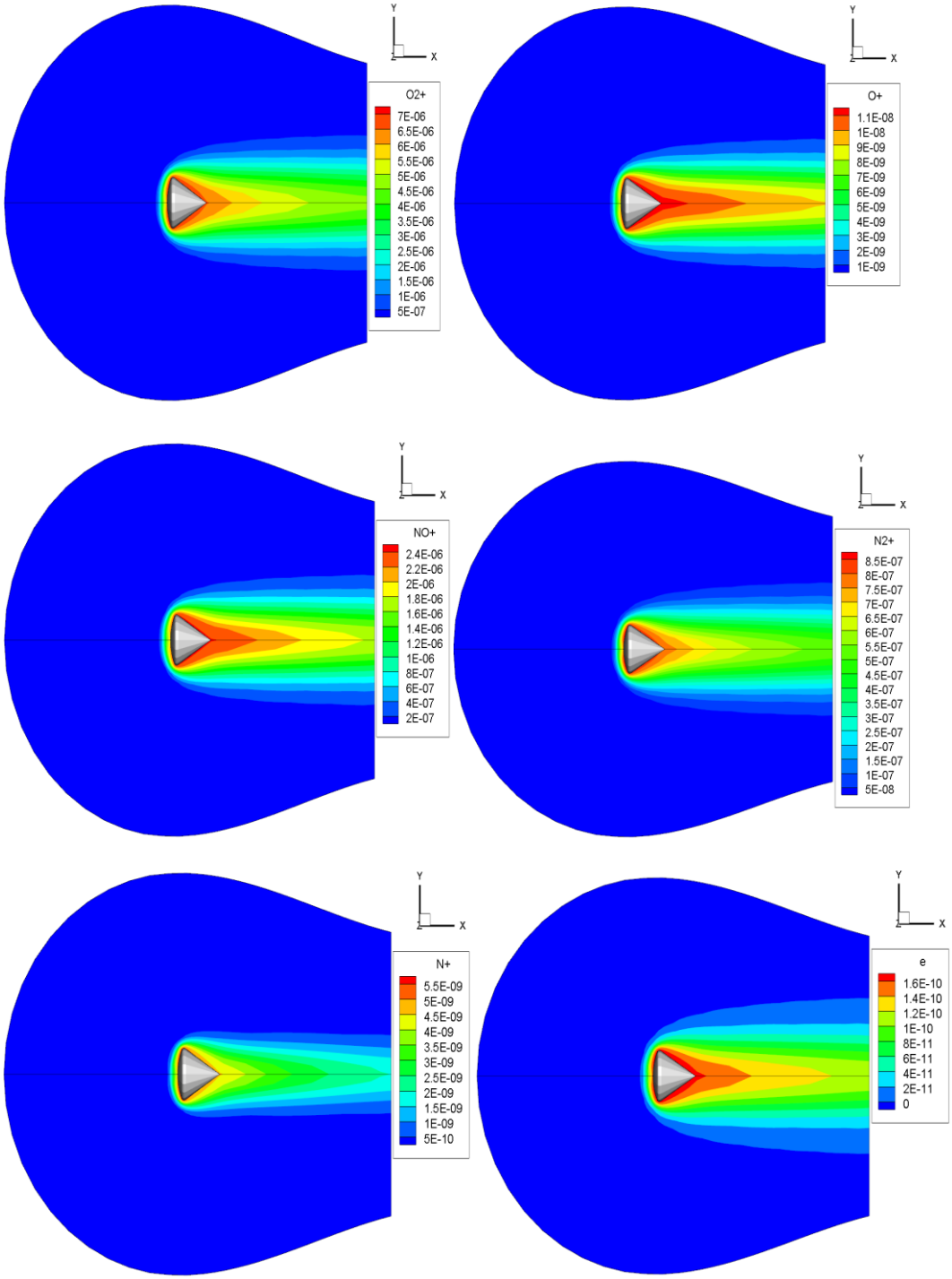

Figure 4.28. Species mass fractions around geometry with 11 species model (M=15, α=0)

In Figure 4.28, contours of species around geometry are shown. Around body temperature is so high; thus, dissociation and ionization reaction are more common in this region. Behind the geometry, flow slows down and temperature is still high; therefore, dissociation reactions occur actively.

Lastly, there are five species (O_2, N_2, NO, N and O) which are both solved in both 5 species and 11 species model. Therefore, to see effects of ionization and charge exchange reactions on these species, distributions of these species are compared in the following figure, Figure 4.29 and Figure 4.30. Hence, it is obvious that ionization and exchange reactions change the distributions of species.

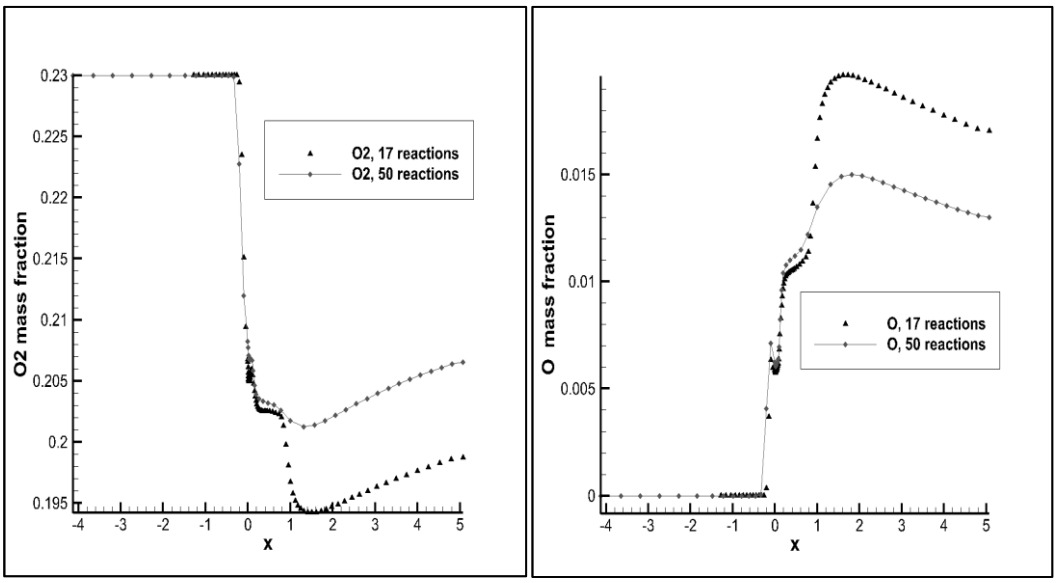

Figure 4.29 Distribution of O_2 and O along stagnation line with different reaction (M=15, α=0)

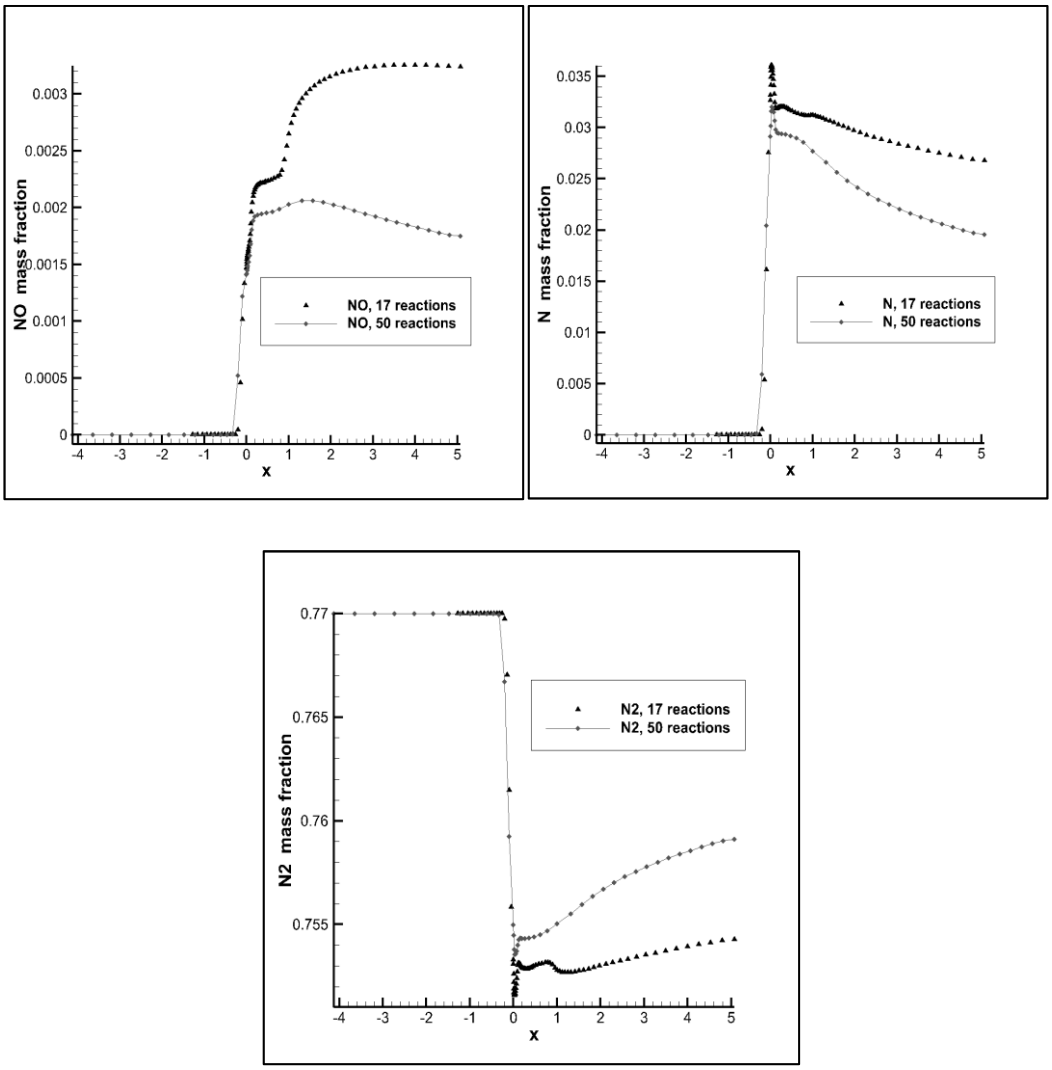

Figure 4.30 Distribution of N_2, NO and N along stagnation line with different reaction numbers (M=15, α=0)

From Figure 4.29 and 4.30, it can be seen that ionization reactions reduce mass fraction of N, NO and O. The main reason for this is that ionization energy of molecules: O_2 and N_2 are higher than that of atoms O and N respectively. Therefore, there is a reduction in the mass fraction of species whose ionization energy is low.

4.5 Results for Vibrational Nonequilibrium Models

In this section, the effects of vibrational nonequilibrium and coupling of vibrational temperature with dissociation reactions are examined. In the following figures, it is assumed that flow field contains only oxygen. The translational-rotational and vibrational-electronic temperatures are obtained as in Figure 4.31. The modelled reactions are dissociations of oxygen. To couple vibrational temperature and dissociation reactions, Park's average temperature is used.

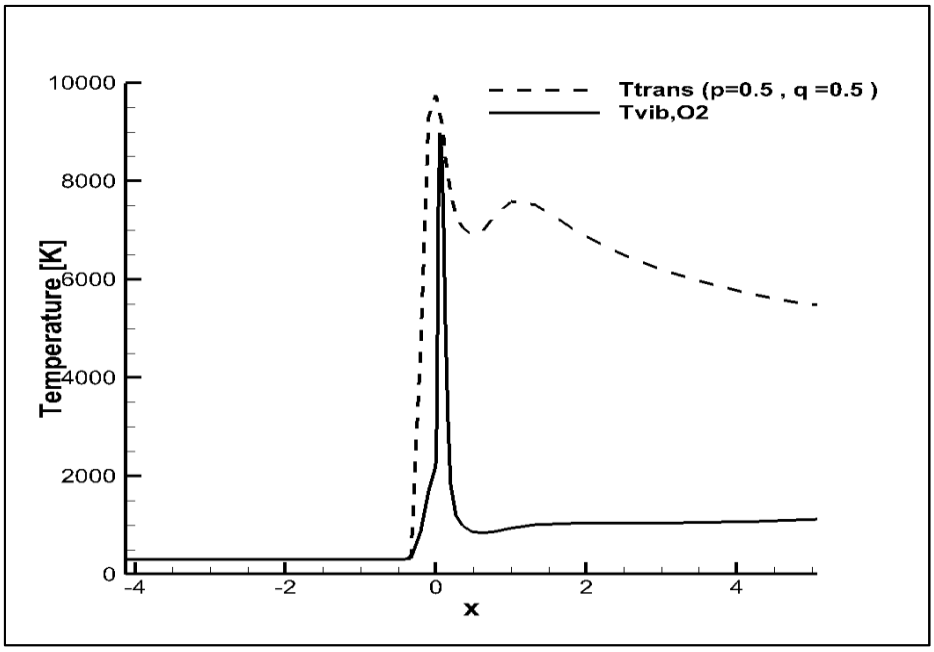

Figure 4.31 Translational and vibrational temperature variation (M=15, α=0)

Moreover, it can be noticed that vibrational temperature values are not as high as translational temperature. The energy transfer between energy modes occurs at fine rate; thus, vibrational temperature values could not reach translational temperature.

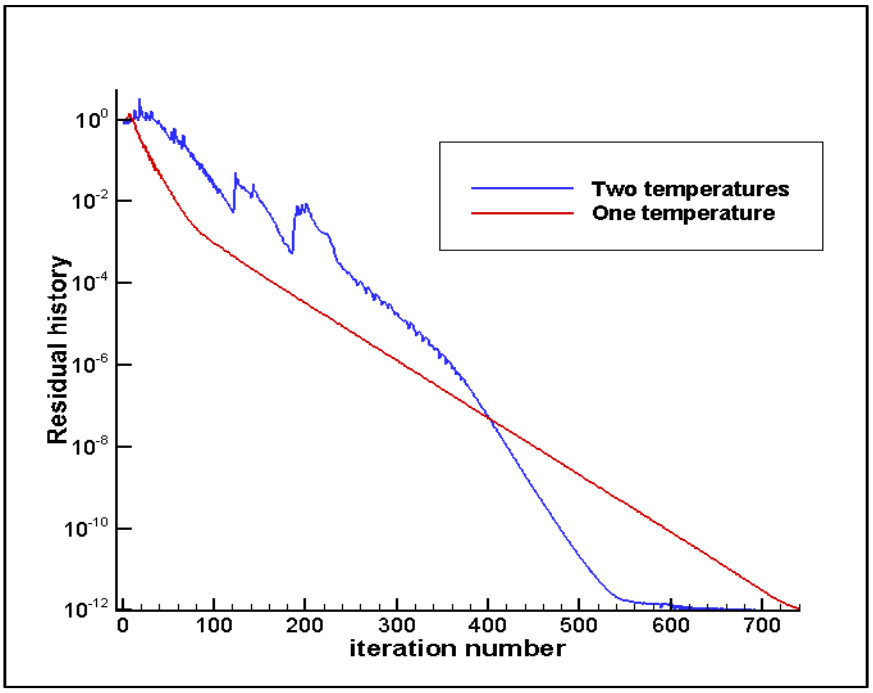

Figure 4.32 Residual histories for one and two temperature models (M=15, α=0)

The convergence characteristics of one and two temperature models have differences as shown in Figure 4.32. Two temperature models solver faces with oscillations and it requires more CPU time. The required CPU time to reach the same convergence for the one and two temperature models solver are 34 minutes and 2 hours 51 minutes, respectively.

The coupling methods for vibrational temperature and dissociation reactions are studied in Figure 4.33. There are different assumptions to consider vibrational temperature on dissociation reactions. The most known method is Park's average temperature. The different coupling methods change the distribution of oxygen slightly. Again, there is not any certain way to prove accuracy of coupling methods. However, it was mentioned that one temperature model overestimates dissociation rate. Also, p and q in the controlling temperature, $T_c = T_{tr}^p T_v^q$ can be changed. Therefore, the reduction in the p term gives reduced dissociation reactions as in Figure 4.33.

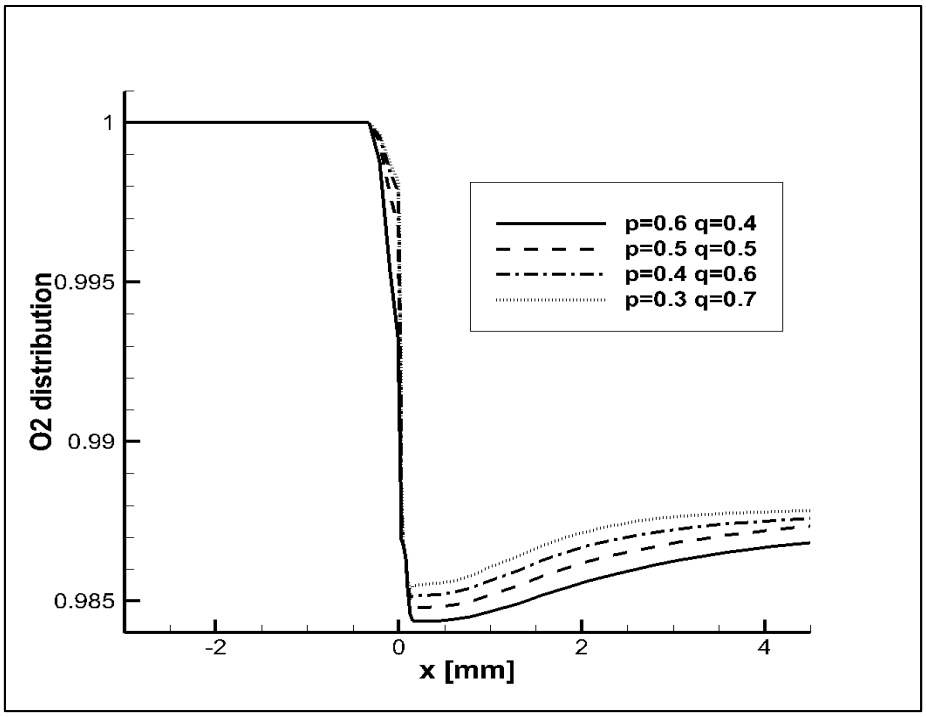

Figure 4.33 Different coupling methods for vibrational temperature and dissociation reactions (M=15, α=0)

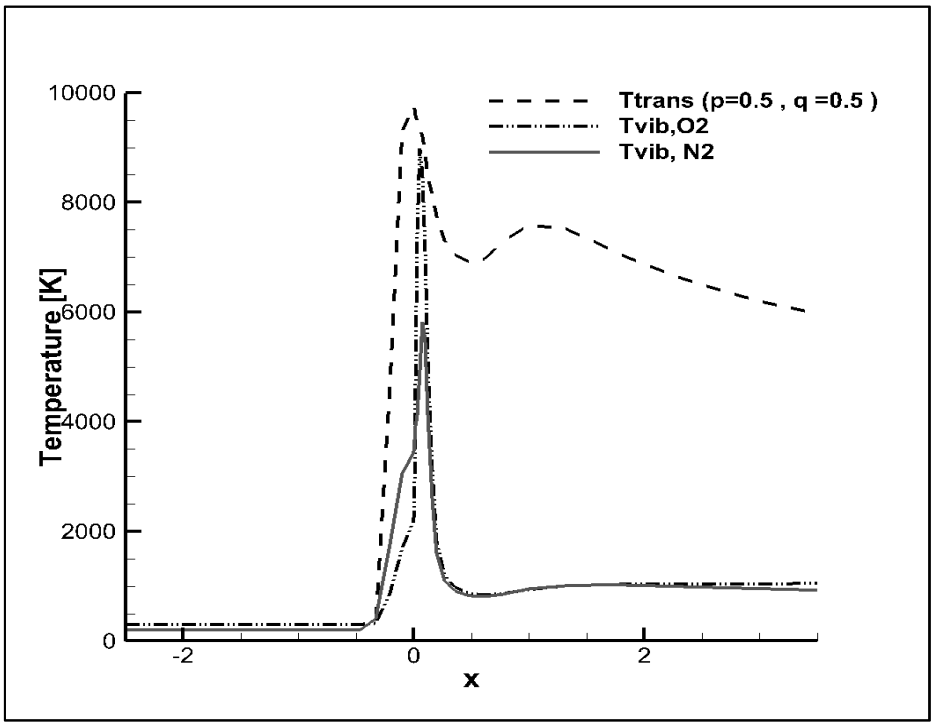

Figure 4.34 Translational and vibrational temperature variations for diatomic oxygen and nitrogen (M=15, α=0)

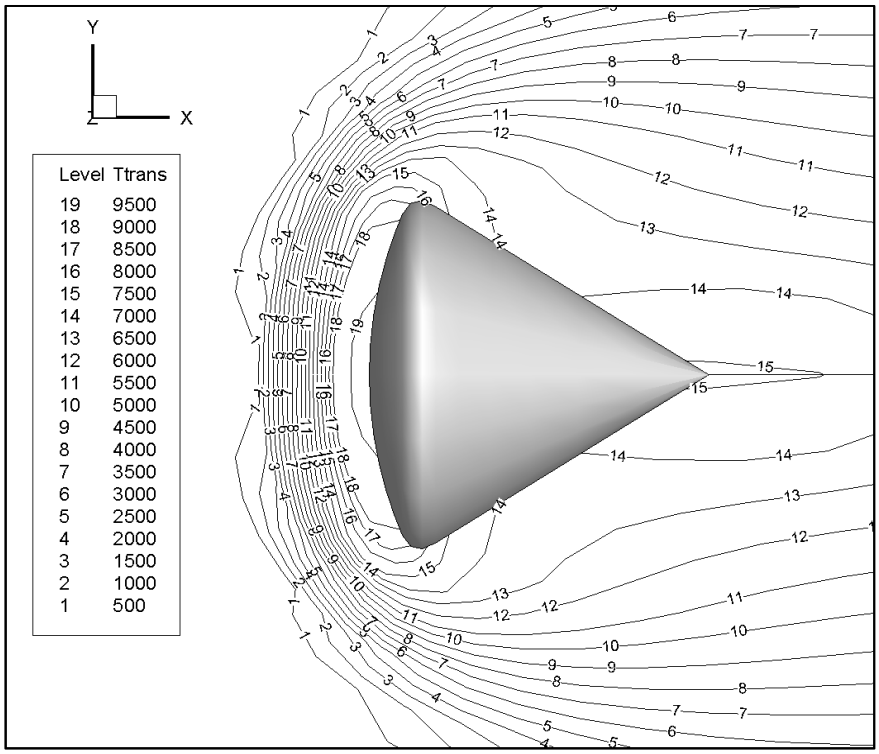

Figure 4.35 Translational temperature contours with Park's two temperature model (M=15, α=0)

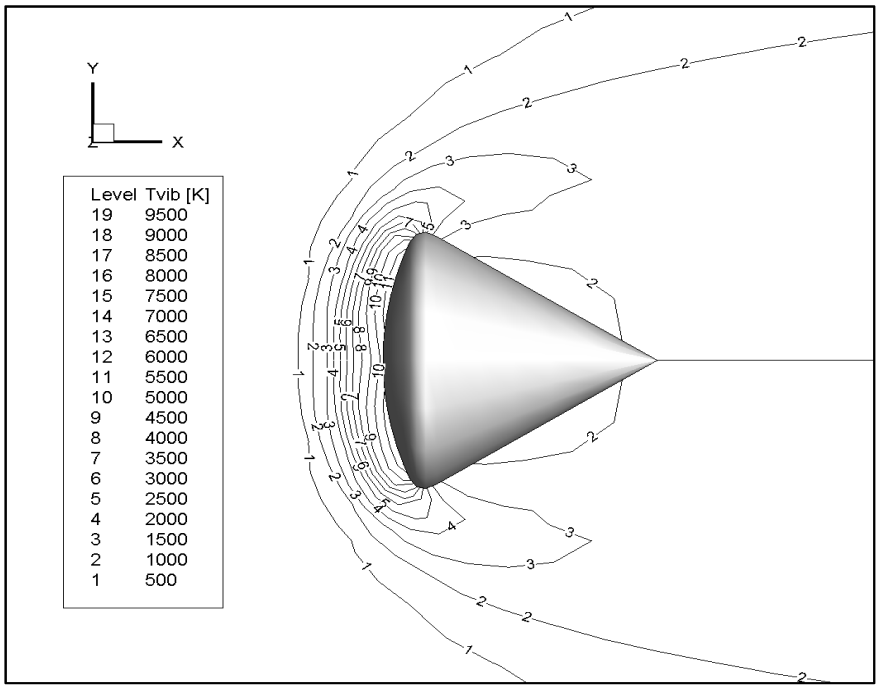

Figure 4.36 Vibrational temperature contours with Park's two temperature model (M=15, α=0)

The vibrational temperature variation for nitrogen molecules are also given in Figure 4.34. The characteristic vibrational temperature of nitrogen molecules are greater than that of oxygen molecules. Therefore, vibrational relaxation rate of nitrogen is slower; it cannot achieve high temperature values of heat bath temperature. Also, vibrational and translational temperature contours around the ACM are given in Figure 4.35 and Figure 4.36. Also, the following figures are obtained by using Park's average temperature assumption where p is 0.5, and q is 0.5.

CHAPTER 5

CONCLUSION AND RECOMMENDATIONS

The purpose of this study is to model hypersonic flow field around the Apollo Command Module during re-entry to the Earth's atmosphere by considering chemical and vibrational nonequilibrium. The real and ideal gas assumptions are compared, and it can be seen that real gas assumption is essential to simulate hypersonic re-entry flow. The ideal gas assumptions lose their accuracy at high temperature; thus, they affect flow characteristics especially shock standoff distance and peak temperature values. At the modelling of chemical nonequilibrium part, different methods and coefficients are studied. Seven different forward reaction rate constants are compared, and two different backward reaction rate calculation methods are also examined. There are not any certain way to prove accuracy of these methods. Therefore, stability and coherence of methods are considered to choose the most efficient models. Also, different species numbers and reaction numbers are investigated. For the vibrational nonequilibrium part, two temperature models are used to obtain vibrational and translational temperature contours. Moreover, coupling between vibrational temperature and dissociation reactions are examined by considering harmonic oscillator assumption. At these parts, it can be seen that the chosen physical models affects flow regime properties. Also, stiffness of real gas and nonequilibrium flow are high, convergence could not obtained for each combinations of models. Lastly, mesh refinement, higher order discretization and different flux splitting methods are studied. Higher order spatial discretization is not applicable for hypersonic flow field simulation with real gas assumptions. Also, Steger- Warming and Van-Leer flux splitting are investigated.

For the future studies, vibrational nonequilibrium modelling can be investigated. Currently, harmonic oscillator assumption is used; however, inharmonic oscillator models should be used to have more accurate modelling. Also, vibrational energy exchange between molecules can also be considered. The electronic energy and rotational energy modes can be solved in addition to translational and vibrational energy modes. Moreover, flow field is assumed as weakly ionized; however, for the most of the re-entries to Earth's atmosphere plasma field around the geometry occurs. Therefore, simulation of flow field can be done by considering plasma dynamics effects. Lastly, solver applicability range can be increased from continuum regime to translational regime by using statistical methods.

REFERENCES

[1] Bertin, J.J., & Cummings, R. M. (2006). Critical Hypersonic Aerothermodynamic Phenomena. *The Annual Review of Fluid Mechanics*, 38: 129-57

[2] USA. Columbia Accident Investigation Board, Printing Office. (2003). *Columbia Accident Investigation Board Report*. Washington, DC.

[3] NASA Engineering and Safety Center Report. (2006). *Stardust Hypervelocity Entry Observing Campaign Support*, RP-06-80.

[4] Vincenti, W. G., & Kruger, C. H. (1967). *Introduction to Physical Gas Dynamics.* New York: Wiley.

[5] Scalabrin, L.C. (2007). *Numerical Simulation of Weakly Ionized Hypersonic Flow over Reentry Capsules*. PhD Thesis. University of Michigan.

[6] Lofthouse, A. J. (2008). *Nonequilibrium Hypersonic Aerothermodynamics using the Direct Simulation Monte Carlo and Navier-Stokes Models*. PhD dissertation. The University of Michigan,

[7] Tirsky, G. A. (1993). Up-to-date Gas Dynamic Models of Hypersonic Aerodynamics and Heat Transfer with Real Gas Properties. *Annual Review of Fluid Mechanics*. 25: 151–181

[8] Park, C. (1993). Review of Chemical-Kinetic Problems of Future NASA Missions, II: Earth Entries. *Journal of Thermophysics and Heat Transfer*. 7(3): 385-398

[9] Bird, G. A. (1994). *Molecular Gas Dynamics and Direct Simulation of Gas Flow*. New York. Oxford. Clarendon Press.

[10] Dietrich, S., &Boyd, I. D. (1996). Scalar and Parallel Optimized Implementation of the Direct Simulation Monte Carlo Method. *Journal of Computational Physics*. 126: 328–342.

[11] Macrossan, M. N. (2001). A Particle-Only Hybrid Method for Near-Continuum Flows. *22nd International Symposium on Rarefied Gas Dynamics*, Vol. 585. (pp. 388-395)

[12 Burt, J. M., & Boyd, I. D. (2008). Extension of a Multiscale Particle Scheme to Near-Equilibrium Viscous Flows. *40th Thermophysics Conference*, AIAA Paper 2008-3914. DOI: 10.2514/1.40262

[13] Park, C. (1989). Assessment of Two Temperature Kinetics Model for Ionizing for Dissociating and Weakly Ionizing Nitrogen. *Journal of Thermophysics Heat Transfer*. Vol. 2, No. 1.

[14] Kim, M., Gülhan, A., & Boyd, I.D. (2011). Modelling of Electron Temperature in Hypersonic Flows. *49th Aerospace Sciences Meeting Including the New Horizons Forum and Aerospace Exposition, Orlando, FL*. AIAA Paper 2011-1028.

[15] Bourdon, A., &Vervisch, P. (1997). Electron-vibration Energy Exchange Models in Nitrogen Plasma Flows. *Phys. Rev. E*, Vol. 55, No. 4, April. (pp. 4634–4641).

[16] Boyd, I.D. (1993). Temperature Dependence of Rotational Relaxation in Shock Waves of Nitrogen. *Journal of Fluid Mechanics*. Vol. 246. (pp. 343-360).

[17] Wang, W., & Shu, C. (2008). On Well-Balanced Schemes for Non-Equilibrium Flow with Stiff Source Terms. *Center for Turbulence Research Annual Research Briefs*. (pp. 391-402)

[18] Gupta, R.N., Yos, J.M., Thompson, R.A. & Lee, K. (1990). A Review of Reaction Rates and Thermodynamic and Transport Properties for an 11-Species Air Model for Chemical and Thermal Nonequilibrium Calculations to 30000 K. *NASA Technical Report No. RP 1232*.

[19] Dunn, M.G., & Kang, S.W. (1973).Theoretical and Experimental Studies of Reentry Plasma". *Technical Report of NASA: CR2232*.

[20] Park, C. (1990). *Nonequilibrium Hypersonic Aerothermodynamics*. John Wiley & Sons.

[21] Gardiner, W.C. (1984). *Combustion Chemistry*. Springer- Verlag, New York.

[22] Sharma, S. P., Huo, W. M., & Park, C. (1988). The Rate Parameters for Coupled Vibration- Dissociation in a Generalized SSH Approximation - Schwartz, Slawsky, and Herzfeld. *Journal of Thermophysics*.Vol.6 No.1 (pp.9-20). DOI: 10.2514/3.312

[23] Marrone, P. V., & Treanor, C. E., (1963). Chemical Relaxation with Preferential Dissociation from Excited Vibrational Levels. *Physics of Fluids*. 6:1215-1221.

[24] Knab, O., Freuhauf, H., &Messerschmid, E., (1995). Theory and validation of the physically consistent coupled vibration-chemistry-vibration model. *Journal of Thermophysics and Heat Transfer*. 9(2):219-226.

[25] Macheret, S. O., Fridman, A.A., Adamovich, I.W., Rich, J.W., &Treanor, C.E. (1994). Mechanisms of nonequilibrium dissociation of diatomic molecules. *6th AIAA/ ASME Joint Thermophysics and Heat Transfer Conference,Colorado Springs, CO*. DOI: 10.2514/6.1994-1984

[26] Maus, J., Griffith, B., Szema, K., & Best, J. (1984). Hypersonic Mach number and Real Gas Effects on Space Shuttle Orbiter Aerodynamics. *Journal of Spacecraft,* 21:136-141.

[27] Woods, W.C., Arrington, J.P., & Hamilton, H. H. (1983). A Review of Preflight Estimates of Real Gas Effects on Space Shuttle Aerodynamic Characteristics. Arrington, J.P., and Jones, J.J. (eds.), *Shuttle Performance: Lessons Learned. NASA CP-2283*. Part 1, pp.309-346.

[28] Tchuen, G., & Burtschell, Y. (1991). *Physico-Chemical Modelling in Nonequilibrium Hypersonic Flow around Blunt Bodies*. Retrieved from http://cdn.intechopen.com/pdfs-wm/19528.pdf last accessed on 07/06/2015

[29] McBride, B.J., Zehe, M.J., Gordon, S. (200). NASA Glenn Coefficients for Calculating Thermodynamic Properties of Individual Species. *NASA Technical Proceedings /TP-2002-211556*

[30] Candler, G.V., & MacCormack, J. (1991). Computation of Weakly Ionized Hypersonic Flows in Thermochemical Nonequilibrium. *Journal of Thermophysics and Heat Transfer*. 5(11):266.

[31] Kumar, S. (2005). *Numerical Simulation of Chemically Reactive Hypersonic Flows*. PhD Dissertation. Berichte aus der Luft- und Raumfahrttechnik.

[32] Panesi, M. (2009). *Physical Models for Nonequilibrium Plasma Flow Simulations at High Speed Re-entry Conditions*. Ph.D. thesis, von Karman Institute for Fluid Dynamics, Rhode-St-Genése, Belgium.

[33] Lee, J. H. (1984). Basic Governing Equations for the Flight Regimes of Aeroassisted Orbital Transfer Vehicles. *Technical Paper 84-1729, AIAA, Snowmass, Colorado*, (pp.17, 68)

[34] Millikan, R. C., & White, D. R. (1963). Systematics of Vibrational Relaxation. *J. of Chem. Phys*. 39, 3209–3213.

[35] Tchuen, G., Burtschell, Y., & Zeitoun, E. D. (2008). Computation of Nonequilibrium Hypersonic Flow with Artificially Upstream Flux Vector Splitting (AUFS) Schemes. *International Journal of Computational Fluid Dynamics*, Vol. 22, No. 4, (pp. 209–220).

[36] Fletcher, A.A.J. (1991). Specific Techniques for Different Flow Categories *Computational Techniques for Fluid Dynamics*. Vol.2, Berlin: Springer –Verlag.

[37] van Leer, B. (1979). Towards the Ultimate Conservative Difference Scheme. V: A second Order Sequel to Godunov's Method. *Journal of Computational Physics*. Vol. 32, No. 1 (pp. 101–136).

[38] Van Albada, G.D., Van Leer, B., & Roberts, W.W. (1982).A Comparative Study of Computational Methods in Cosmic Gas Dynamics. *Astronomy and Astrophysics*. Vol. 108. (pp. 76–84).

[39] Venkatakrishnan, V. (1995). Convergence to Steady State Solutions of the Euler Equations on Unstructured Grids with Limiters. *J. Computational Phys.,* Vol. 118 (pp.120-130).

[40] Liou, M.S., Van Leer, B., & Shuen, J.S. (1990). Splitting of Inviscid Fluxes for Real Gases. *Journal of Computational Physics*. Vol.87. (pp.1-24).

[41] Grossman, B., & Cinnella, P. (1990). Flux Split Algorithm for Flows with Non-Equilibrium Chemistry and Vibrational Relaxation. *Journal of Computational Physics.* Vol.88 (pp.131-168).

[42] Steger, J. L., & Warming, R. R. (1981). Flux Vector Splitting of Inviscid Gas Dynamics with Application to Finite Difference Methods. *Journal of Computational Physics.* Vol. 40, No. 2 (pp. 263-293).

[43]Grossman, B., & Cinnella, P. (1988). The Computation of Non-Equilibrium, Chemically Reacting Flow. *Computers & Structures*., Vol.30, No. ½ (pp. 79-93).

[44] Brown P.N., & Hindmarsh A.C. (1986). Matrix-free methods for stiff systems of ODEs. *SIAM Journal on Numerical Analysis.* Vol. 23 (pp. 610–638).

[45] Dembo, R.S., Eisenstat, C., & Steihaug, T. (1982). Inexact Newton methods. *SIAM Journal of Numerical Analysis*, Vol.19 (pp.400-408).

[46] Simonis, J.P. (2003). *A Numerical Study of Globalizations of Newton –GMRES Methods*. Master Thesis, Worcester Polytechnic Institute.

[47] Bai, Z., Hu, D., & Reichel, L. (1994). A Newton Basis GMRES Implementation. *IMA Journal of Numerical Analysis*, Vol. 14 (pp.563-581).

[48] Park, C. (1985). On convergence of computation of chemically reacting flows. *23rd AIAA Aerospace Sciences Meeting and Exhibit*. Vol. 85-0247.

[49] Murray, A. (1999). Aeroheating Analysis for Planetary Re-Entry Vehicles. *ITT Industries Report*. Retrieved from https://tfaws.nasa.gov/TFAWS04/Website/ program/ paper/TFAWS04_AMurray_Aero_CFD.pdf

[50] Bertin, J.J. (1966). *The Effect of Protuberances, Cavities, and Angle of Attack on the Wind Tunnel Pressure and Heat Transfer Distribution for the Apollo Command Module*. NASA Technical Report.

[51] Marvin, J., Tendeland, T., &Kussoy, M. (1963). *Apollo Forebody Pressure and Heat-Transfer Distributions in Helium at M=20*. NASA Ames Research Center, NASA TM X-854, Moffett Field, CA.

[52] Papadopoulou, E. (2013). *Numerical Simulation of the Apollo 4 Reentry Trajectory*. Master Thesis. Aristotle University of Thessaloniki and Ecole Polytechnique Federale de Lausanne.

APPENDIX A

DATA FOR CHEMICAL NONEQUILIBRIUM

Table A.1 Molecular weight of the species

Species	Molecular weight (kg/mol)	Characteristic Temperature (K)
O_2	0.032	2239.
N_2	0.028	3395.
NO	0.030	2817.
N	0.014	0.
O	0.016	0.
O_2^+	0. 0319994514	2239.
N_2^+	0. 0279994514	3395.
NO^+	0. 0299994514	2817.
N^+	0. 0139994514	0.
O^+	0. 0159994514	0.
e	5.486×10^{-7}	0.

Table A2 Thermochemical coefficient of species taken by NASA Glenn research center [44]

	coef1	coef2	coeff3	coef4	coef5	coef6	coef7	coef8	coeff9
O									
	-7,953611300E+03	1,607177787E+02	1,966226438E+00	1,013670310E-03	-1,110415423E-06	6,517507500E-10	-1,584779251E-13	2,840362437E+04	8,404241820E+00
	2,619020262E+05	-7,298722030E+02	3,317177270E+00	-4,281334360E-04	1,036104594E-07	-9,438304330E-12	2,725038297E-16	3,392428060E+04	-6,679585350E-01
	1,779004264E+08	-1,082328257E+05	2,810778365E+01	-2,975232262E-03	1,854997534E-07	-5,796231540E-12	7,191720164E-17	8,890942630E+05	-2,181728151E+02
O2									
	-3,425563420E+04	4,847000970E+02	1,119010961E+00	4,293889240E-03	-6,836300520E-07	-2,023372700E-09	1,039040018E-12	-3,391454870E+03	1,849699470E+01
	-1,037939033E+06	2,344830282E+03	1,819732036E+00	1,267847582E-03	-2,188067988E-07	2,053719572E-11	-8,193467050E-16	-1,689010929E+04	1,738716506E+01
	4,975294300E+08	-2,866106875E+05	6,690352250E+01	-6,169959020E-03	3,016396027E-07	-7,421416600E-12	7,278175770E-17	2,293554027E+06	-5,530621610E+02
N									
	0,000000000E+00	0,000000000E+00	2,500000000E+00	0,000000000E+00	0,000000000E+00	0,000000000E+00	0,000000000E+00	5,610463780E+04	4,193905036E+00
	8,876501380E+04	-1,071231500E+02	2,362188287E+00	2,916720081E-04	-1,729515100E-07	4,012657880E-11	-2,677227571E-15	5,697351330E+04	4,865231506E+00
	5,475181050E+08	-3,107574980E+05	6,916782740E+01	-6,847988130E-03	3,827572400E-07	-1,098367709E-11	1,277986024E-16	2,550585618E+06	-5,848769753E+02
N2									
	2,210371497E+04	-3,818461820E+02	6,082738360E+00	-8,530914410E-03	1,384646189E-05	-9,625793620E-09	2,519705809E-12	7,108460860E+02	-1,076003744E+01
	5,877124060E+05	-2,239249073E+03	6,066949220E+00	-6,139685500E-04	1,491806679E-07	-1,923105485E-11	1,061954386E-15	1,283210415E+04	-1,586640027E+01
	8,310139160E+08	-6,420733540E+05	2,020264635E+02	-3,065092046E-02	2,486903333E-06	-9,705954110E-11	1,437538881E-15	4,938707040E+06	-1,672099740E+03
NO									
	-1,143916503E+04	1,536467592E+02	3,431468730E+00	-2,668592368E-03	8,481399120E-06	-7,685111050E-09	2,386797655E-12	9,098214410E+03	6,728725490E+00
	2,239018716E+05	-1,289651623E+03	5,433936030E+00	-3,656034900E-04	9,880966450E-08	-1,416076856E-11	9,380184620E-16	1,750317656E+04	-8,501669090E+00
	-9,575303540E+08	5,912434480E+05	-1,384566826E+02	1,694339403E-02	-1,007351096E-06	2,912584076E-11	-3,295109350E-16	-4,677501240E+06	1,242081216E+03
N2+	-3,474047470E+04	2,696222703E+02	3,164916370E+00	-2,132239781E-03	6,730476400E-06	-5,637304970E-09	1,621756000E-12	1,790004424E+05	6,832974166E+00
	-2,845599002E+06	7,058893030E+03	-2,884886385E+00	3,068677059E-03	-4,361652310E-07	2,102514545E-11	5,411996470E-16	1,340388483E+05	5,090897022E+01
	-3,712829770E+08	3,139287234E+05	-9,603518050E+01	1,571193286E-02	-1,175065525E-06	4,144441230E-11	-5,621893090E-16	-2,217361867E+06	8,436270947E+02

Table A.2 continued.

	coef1	coef2	coeff3	coef4	coef5	coef6	coef7	coef8	coeff9
NO+	1,398106635E+03	-1,590446941E+02	5,122895400E+00	-6,394388620E-03	1,123918342E-05	-7,988581260E-09	2,107383677E-12	1,187495132E+05	-4,398433810E+00
	6,069876900E+05	-2,278395427E+03	6,080324670E+00	-6,066847580E-04	1,432002611E-07	-1,747990522E-11	8,935014060E-16	1,322709615E+05	-1,519880037E+01
	2,676400347E+09	-1,832948690E+06	5,099249390E+02	-7,113819280E-02	5,317659880E-06	-1,963208212E-10	2,805268230E-15	1,443308939E+07	-4,324044462E+03
N+	5,237079210E+03	2,299958315E+00	2,487488821E+00	2,737490756E-05	-3,134447576E-08	1,850111332E-11	-4,447350984E-15	2,256284738E+05	5,076830786E+00
	2,904970374E+05	-8,557908610E+02	3,477389290E+00	-5,288267190E-04	1,352350307E-07	-1,389834122E-11	5,046166279E-16	2,310809984E+05	-1,994146545E+00
	1,646092148E+07	-1,113165218E+04	4,976986640E+00	-2,005393583E-04	1,022481356E-08	-2,691430863E-13	3,539931593E-18	3,136284696E+05	-1,706646380E+01
O2+	-8,607205450E+04	1,051875934E+03	-5,432380470E-01	6,571166540E-03	-3,274263750E-06	5,940645340E-11	3,238784790E-13	1,345544668E+05	2,902709750E+01
	7,384654880E+04	-8,459559540E+02	4,985164160E+00	-1,611010890E-04	6,427083990E-08	-1,504939874E-11	1,578465409E-15	1,446321044E+05	-5,811230650E+00
	-1,562125524E+09	1,161406778E+06	-3,302504720E+02	4,710937520E-02	-3,354461380E-06	1,167968599E-10	-1,589754791E-15	-8,857866270E+06	2,852035602E+03
O+	0,000000000E+00	0,000000000E+00	2,500000000E+00	0,000000000E+00	0,000000000E+00	0,000000000E+00	0,000000000E+00	1,879352842E+05	4,393376760E+00
	-2,166513208E+05	6,665456150E+02	1,702064364E+00	4,714992810E-04	-1,427131823E-07	2,016595903E-11	-9,107157762E-16	1,837191966E+05	1,005690382E+01
	-2,143835383E+08	1,469518523E+05	-3,680864540E+01	5,036164540E-03	-3,087873854E-07	9,186834870E-12	-1,074163268E-16	-9,614208960E+05	3,426193080E+02
e	0,000000000E+00	0,000000000E+00	2,500000000E+00	0,000000000E+00	0,000000000E+00	0,000000000E+00	0,000000000E+00	-7,453750000E+02	-1,172081224E+01
	0,000000000E+00	0,000000000E+00	2,500000000E+00	0,000000000E+00	0,000000000E+00	0,000000000E+00	0,000000000E+00	-7,453750000E+02	-1,172081224E+01
	0,000000000E+00	0,000000000E+00	2,500000000E+00	0,000000000E+00	0,000000000E+00	0,000000000E+00	0,000000000E+00	-7,453750000E+02	-1,172081224E+01

The forward reaction rate constants for 5 species and 17 reactions,

Table A.3 Gardiner Model [17]

Reactions number	Reactions	A_i $[^{m^3}/_{mols}$	β_i $[-]$	$^{E_i}/_{R_u}$ $[K]$
1	$O_2 + N \rightleftarrows 2O + N$	1.82E+12	-1.	59380.
2	$O_2 + NO \rightleftarrows 2O + NO$	1.82E+12	-1.	59380.
3	$O_2 + N_2 \rightleftarrows 2O + N_2$	3.64E+12	-1.	59380.
4	$2O_2 \rightleftarrows 2O + O_2$	1.64E+13	-1.	59380.
5	$O_2 + O \rightleftarrows 3O$	4.56E+13	-1.	59380.
6	$N_2 + N \rightleftarrows 3N$	1.60E+16	-1.6	113200.
7	$N_2 + NO \rightleftarrows 2N + NO$	1.40E+15	-1.6	113200.
8	$2N_2 \rightleftarrows 2N + N_2$	3.70E+15	-1.6	113200.
9	$N_2 + O_2 \rightleftarrows 2N + O_2$	1.40E+15	-1.6	113200.
10	$N_2 + O \rightleftarrows 2N + O$	1.40E+15	-1.6	113200.
11	$NO + N \rightleftarrows 2N + O$	4.00E+14	-1.5	75510.
12	$NO + NO \rightleftarrows N + O + NO$	4.00E+14	-1.5	75510.
13	$NO + N_2 \rightleftarrows N + O + N_2$	8.00E+14	-1.5	75510.
14	$NO + O_2 \rightleftarrows N + O + O_2$	8.00E+14	-1.5	75510.
15	$NO + O \rightleftarrows N + 2O$	8.00E+14	-1.5	75510.
16	$N_2 + O \rightleftarrows NO + N$	3.80E+03	1.0	20820.
17	$NO + O \rightleftarrows O_2 + N$	1.82E+8	0.	38370.

Table A.4 Dunn & Kang [15] and Gupta [14] models

RN	Dunn & Kang model			Gupta model		
	A_i $[m^3/mols]$	β_i $[-]$	E_i/R_u [K]	A_i $[m^3/mols]$	β_i $[-]$	E_i/R_u [K]
1	3.60E+12	-1.	59500.	3.61E+12	-1.	59400.
2	3.60E+12	-1.	59500.	3.61E+12	-1.	59400.
3	7.20E+12	-1.	59500.	3.61E+12	-1.	59400.
4	3.24E+13	-1.	59500.	3.61E+12	-1.	59400.
5	9.00E+13	-1.	59500.	3.61E+12	-1.	59400.
6	4.08E+16	-1.5	113000.	4.15E+16	-1.5	113100.
7	1.90E+11	-0.5	113000.	1.92E+11	-0.5	113100.
8	4.70E+11	-0.5	113000.	1.92E+11	-0.5	113100.
9	1.90E+11	-0.5	113000.	1.92E+11	-0.5	113100.
10	1.90E+11	-0.5	113000.	1.92E+11	-0.5	113100.
11	3.90E+14	-1.5	75500.	3.97E+14	-1.5	75600.
12	3.90E+14	-1.5	75500.	3.97E+14	-1.5	75600.
13	7.80E+14	-1.5	75500.	3.97E+14	-1.5	75600.
14	7.80E+14	-1.5	75500.	3.97E+14	-1.5	75600.
15	7.80E+14	-1.5	75500.	3.97E+14	-1.5	75600.
16	7.00E+07	0.	38000.	6.75E+07	0.	37500.
17	3.20E+03	1.	19700.	3.18E+03	1.	19700.

Table A.5 Curve fit [45] and Park 85 [46] models

RN	Curve fit model			Park 85 model		
	A_i $[^{m^3}/_{mols}]$	β_i $[-]$	$^{E_i}/_{R_u}$ [K]	A_i $[^{m^3}/_{mols}]$	β_i $[-]$	$^{E_i}/_{R_u}$ [K]
1	2.00E+14	-1.18	59500.	8.25E+12	-1.	59500.
2	1.072E+14	-1.23	59500.	2.75E+13	-1.	59500.
3	1.072E+14	-1.23	59500.	2.75E+13	-1.	59500.
4	1.072E+14	-1.23	59500.	2.75E+13	-1.	59500.
5	2.00E+14	-1.18	59500.	8.25E+13	-1.	59500.
6	2.95E+16	-1.54	113200.	1.11E+16	-1.6	113200.
7	2.74E+13	-0.99	113200.	3.70E+15	-1.6	113200.
8	2.74E+13	-0.99	113200.	3.70E+15	-1.6	113200.
9	2.74E+13	-0.99	113200.	3.70E+15	-1.6	113200.
10	2.95E+16	-1.54	113200.	1.11E+16	-1.6	113200.
11	5.14E+13	-1.02	75600.	2.30E+11	-0.5	75500.
12	5.14E+13	-1.02	75600.	2.30E+11	-0.5	75500.
13	5.14E+13	-1.02	75600.	4.60E+11	-0.5	75500.
14	5.00E+14	-0.984	75600.	4.60E+11	-0.5	75500.
15	5.00E+14	-0.984	75600.	8.00E+11	-0.5	75500.
16	1.70E+08	-0.0975	38000.	3.18E+07	0.1	37700.
17	5.00E+04	0.69	19400.	2.16E+02	1.29	19220.

Table A.6 Park 87 [9] and Park 90 [16] models

RN	Park 87 model			Park 90 model		
	A_i $[^{m^3}/_{mols}]$	β_i $[-]$	$^{E_i}/_{R_u}$ [K]	A_i $[^{m^3}/_{mols}]$	β_i $[-]$	$^{E_i}/_{R_u}$ [K]
1	2.90E+17	-2.00	59750.	1.00E+16	-1.50	59500.
2	9.68E+16	-2.00	59750.	2.00E+15	-1.50	59500.
3	9.68E+16	-2.00	59750.	2.00E+15	-1.50	59500.
4	9.68E+16	-2.00	59750.	2.00E+15	-1.50	59500.
5	2.90E+17	-2.00	59750.	1.00E+16	-1.50	59500.
6	1.60E+16	-1.60	113200.	3.00E+16	-1.6	113200.
7	4.98E+15	-1.60	113200.	7.00E+15	-1.6	113200.
8	3.70E+15	-1.60	113200.	7.00E+15	-1.6	113200.
9	3.70E+15	-1.60	113200.	7.00E+15	-1.6	113200.
10	4.98E+16	-1.60	113200.	3.00E+16	-1.6	113200.
11	7.95E+17	-2.00	75500.	5.00E+11	0.0	75500.
12	7.95E+17	-2.00	75500.	5.00E+11	0.0	75500.
13	7.95E+17	-2.00	75500.	5.00E+11	0.0	75500.
14	7.95E+17	-2.00	75500.	1.10E+11	0.0	75500.
15	7.95E+17	-2.00	75500.	1.10E+11	0.0	75500.
16	6.44E+11	-1.00	38370.	6.40E+07	-1.0	38400.
17	8.37E+06	0.00	19450.	8.40E+02	0.0	19400.

The forward reaction rate constants for 11 species and 49 reactions,

Table A.7 Forward reaction rates are obtained from Park study [8].

Reactions number	Reactions	$A_i\ [^{m^3}/_{mols}]$	$\beta_i\ [-]$	$^{E_i}/_{R_u}\ [K]$
1,2,3	$O_2 + M \rightleftarrows 2O + M$ $M=N_2, O_2, NO$	2.00E+15	-1.50	59500.
4,5	$O_2 + M \rightleftarrows 2O + M$ M= N, O	1.00E+16	-1.50	59500.
6,7,8	$O_2 + M \rightleftarrows 2O + M$ $M= N_2^+, {O_2}^+, NO^+$	2.00E+15	-1.50	59500.
9,10	$O_2 + M \rightleftarrows 2O + M$ $M= N^+, O^+$	1.00E+16	-1.50	59500.
11,12,13	$N_2 + M \rightleftarrows 2N + M$ $M=N_2, O_2, NO$	7.00E+15	-1.60	113200.
14,15	$N_2 + M \rightleftarrows 2N + M$ M= N, O	3.00E+16	-1.60	113200.
16,17,18	$N_2 + M \rightleftarrows 2N + M$ $M= N_2^+, {O_2}^+, NO^+$	7.00E+15	-1.60	113200.
19,20	$N_2 + M \rightleftarrows 2N + M$ $M= N^+, O^+$	3.00E+16	-1.60	113200.
21,22,23	$NO + M \rightleftarrows N + O + M$ $M=N_2, O_2, NO$	5.00E+09	0.0	75500.
24,25	$NO + M \rightleftarrows N + O + M$ M= N, O	1.11E+11	0.0	75500.
26,27,28	$NO + M \rightleftarrows N + O + M$ $M= N_2^+, {O_2}^+, NO^+$	5.00E+09	0.0	75500.
29,30	$NO + M \rightleftarrows N + O + M$ $M= N^+, O^+$	1.11E+11	0.0	75500.
31	$N_2 + e \rightleftarrows 2N + e$	1.20E+19	-1.6	113200.
32	$N + e \rightleftarrows N^+ + 2e$	2.50E+28	-3.82	168600.
33	$O + e \rightleftarrows O^+ + 2e$	3.90E+27	-3.78	158500.
34	$N_2 + O \rightleftarrows NO + N$	6.40E+11	-1.0	38400.
35	$NO + O \rightleftarrows O_2 + N$	8.40E+06	-0.0	19450.
36	$N + O \rightleftarrows NO^+ + e$	8.80E+02	1.0	31900.
37	$N + N \rightleftarrows N_2^+ + e$	4.40E+01	1.5	67500.
38	$O + O \rightleftarrows O_2^+ + e$	7.10E-04	2.70	80600.

39	$O^+ + N_2 \rightleftarrows N_2^+ + O$	9.10E+05	0.36	22800.
40	$O^+ + NO \rightleftarrows N^+ + O_2$	1.40E-01	1.90	26600.
41	$NO^+ + O_2 \rightleftarrows O_2^+ + NO$	2.40E+07	0.41	32600.
42	$NO^+ + N \rightleftarrows N_2^+ + O$	7.20E+07	0.0	35500.
43	$NO^+ + O \rightleftarrows N^+ + O_2$	1.00E+06	0.5	77200.
44	$O_2^+ + N \rightleftarrows N^+ + O_2$	8.70E+07	0.14	28600.
45	$O_2^+ + N_2 \rightleftarrows N_2^+ + O_2$	9.90E+06	0.0	40700.
46	$NO^+ + N \rightleftarrows O^+ + N_2$	3.40E+07	-1.08	12800.
47	$NO^+ + O \rightleftarrows O_2^+ + N$	7.20E+06	0.29	48600.
48	$O_2^+ + O \rightleftarrows O^+ + O_2$	4.00E+06	-0.09	18000.
49	$N^+ + N_2 \rightleftarrows N_2^+ + N$	1.00E+06	0.5	11200.

Table A.8 Equilibrium coefficients for 5 species and 17 reactions [14]

Reactions	Coefficients					
	c_1	c_2	c_3	c_4	c_5	c_6
1 to 5	0.00000E+00	-0.48129E+00	-0.18309E+01	-0.82835E+00	-0.56203E+01	-0.39664E+01
6 to 10	0.00000E+00	-0.10406E+01	-0.27317E+01	-0.24633E+01	-0.11689E+02	-0.89886E+01
11 to 15	0.00000E+00	-0.66282E+00	-0.20677E+01	-0.12125E+01	-0.78281E+01	-0.67849E+01
16	0.00000E+00	-0.37785E+00	-0.66398E+00	-0.12508E+01	-0.38613E+01	-0.22037E+01
17	0.00000E+00	-0.21458E+00	-0.30792E+00	-0.50191E+00	-0.25374E+01	-0.31838E+01